Multidimensional Signal Processing Techniques for Disturbance Mitigation in Synthetic Aperture Systems

by

Chamira Udaya Shantha Edussooriya
B.Sc.Eng., University of Moratuwa, Sri Lanka, 2008

A Thesis Submitted in Partial Fulfillment of the
Requirements for the Degree of

MASTER OF APPLIED SCIENCE

in the Department of Electrical and Computer Engineering

University of Victoria

Multidimensional Signal Processing Techniques for Disturbance Mitigation in Synthetic Aperture Systems

by

Chamira Udaya Shantha Edussooriya
B.Sc.Eng., University of Moratuwa, Sri Lanka, 2008

Supervisory Committee

Dr. Leonard T. Bruton, Co-Supervisor
(Department of Electrical and Computer Engineering)

Dr. Panajotis Agathoklis, Co-Supervisor
(Department of Electrical and Computer Engineering)

Supervisory Committee

Dr. Leonard T. Bruton, Co-Supervisor
(Department of Electrical and Computer Engineering)

Dr. Panajotis Agathoklis, Co-Supervisor
(Department of Electrical and Computer Engineering)

ABSTRACT

In this thesis, multidimensional signal processing techniques to mitigate disturbances in synthetic aperture systems such as radio telescopes are investigated. Here, two computationally efficient three-dimensional (3D) spatio-temporal (ST) finite impulse response (FIR) cone filter bank structures are proposed. Furthermore, a strategy is proposed to design 3D ST FIR frustum filter banks, having double-frustum-shaped passbands oriented along the temporal axis, derived from appropriate 3D ST FIR cone filter banks. Both types of cone and frustum filter banks are almost alias free and provide near-perfect reconstruction. In the proposed cone and frustum filter banks, both temporal and spatial filtering operations can be carried out at a significantly lower rate compared to previously reported 3D ST FIR cone filter banks implying lower power consumption. Furthermore, the proposed cone and frustum filter banks require a significantly lower computational complexity than previously reported 3D ST FIR cone and frustum filter banks. Importantly, this is achieved without deteriorating the improvement in signal-to-interference-plus-noise ratio.

A theoretical analysis of brightness distribution (BD) errors caused by parameter perturbations and mismatches among the transfer functions of receivers employed in synthetic aperture systems is presented. First, the BD errors caused by perturbations in the transfer functions of low noise amplifiers (LNAs) and anti-aliasing filters (AAFs) are considered, and the characteristics of the additive BD error and its effects on synthesized BDs are thoroughly analyzed. Second, the conditions that should be satisfied by the transfer functions of digital beamformers to eliminate the BD errors caused by their phase responses are examined. The sufficient condition to eliminate the BD errors is that the transfer functions are matched, and, interestingly, the phase responses are not necessary to be linear. Furthermore, the BD errors caused by typical tolerances of passive L and C elements used to implement the AAFs and those caused by the random variations of gain from LNA to LNA are quantified through numerical simulations. The simulations indicate that substantial BD errors are observed at frequencies that are close to the passband edge of the AAFs.

Contents

List of Tables

List of Figures

List of Abbreviations

1D	One-Dimensional
2D	Two-Dimensional
3D	Three-Dimensional
4D	Four-Dimensional
AAF	Anti-Aliasing Filter
ADC	Analog-to-Digital Converter
AFAD	Advanced Focal Array Demonstrator
APERTIF	APERture Tile In Focus
ASKAP	Australian Square Kilometre Array Pathfinder
BB	BroadBand
BD	Brightness Distribution
CD	Continuous-Domain
CDFT	Continuous-Domain Fourier Transform
DAA	Dense Aperture Array
DD	Discrete-Domain
DDFT	Discrete-Domain Fourier Transform
DFT	Discrete Fourier Transform
DLA	Dense Linear Array
DOA	Direction Of Arrival
EM	ElectroMagnetic
EMBRACE	Electronic Multi-Beam Radio Astronomy ConcEpt

FFT	Fast Fourier Transform
FIR	Finite Impulse Response
FoV	Field of View
FPA	Focal Plane Array
IDFT	Inverse Discrete Fourier Transform
IF	Intermediate Frequency
IIR	Infinite Impulse Response
LNA	Low Noise Amplifier
MD	Mixed-Domain
MDFT	Mixed-Domain Fourier Transform
PHAD	PHased-Array feed Demonstrator
PW	Plane Wave
RF	Radio Frequency
RFI	Radio Frequency Interfering
ROS	Region Of Support
SINR	Signal-to-Interference-plus-Noise Ratio
SKA	Square Kilometre Array
SOI	Signal Of Interest
ST	Spatio-Temporal
THEA	THousand Element Array
VLA	Very Large Array
VLSI	Very Large Scale Integrated
WSRT	Westerbork Synthesis Radio Telescope

ACKNOWLEDGEMENTS

First, I would like to express heartfelt gratitude to my co-supervisors Dr. Leonard T. Bruton and Dr. Panajotis Agathoklis for their mentorship, advice, inspiring discussions and patience. Furthermore, I really appreciate their kind support and encouragement provided me during hard times. Besides those, I admire their dedication to the advancement of the multidimensional signal processing field.

I am very grateful to Dr. Chulantha Kulasekere and Dr. Rohan Munasinghe at the University of Moratuwa, Sri Lanka and Dr. Arjuna Madanayake at the University of Calgary (currently at the University of Akron) for all the assistance provided me to open the doors of graduate studies.

Next, I wish to thank course instructors: Dr. Andreas Antoniou, Dr. Wu-Sheng Lu, Dr. Jens Bornemann and Dr. Michael Adams for their outstanding teaching and inspiration. I also acknowledge the assistance received from the staff of the Department of Electrical and Computer Engineering including Ms. Moneca Bracken, Ms. Vicky Smith, Ms. Lynne Barrett, Ms. Janice Closson and Mr. Dan Mai. My special thank goes to Mr. Kevin Jones for his kind assistance provided to me whenever I had technical issues. Furthermore, a special thank goes to my senior colleague Dr. Thushara Gunaratne at the University of Calgary for providing me the Focal Field Synthesizer program.

Victoria and UVic itself are gorgeous places. However, life would have been dull and boring if I had not had companionship with a nice group of humans: my colleagues and friends. I take this opportunity to express sincere gratitude to my colleague Ioana Sevcenco for her support, encouragement and wonderful friendship. Also, I am grateful to my colleagues and friends Soltan Alharbi, Dr. Ana-Maria Sevcenco, Iman Moazzen, Ping Li, Xi Tu, Dan Li, Ahmad Abdullah and Xinyu Fang.

My strength is my family: father, mother and sister. I would not have been able to reach to the destination without their unconditional love, constant support and encouragement. Also, I wish to thank families of Dr. Deepal Samarajeewa, Mr. Gamini Fonseka and Mr. Sisira Kosgoda for all the support given to me during my stay in Victoria.

Last but not least, I greatly acknowledge the financial support received from the Natural Sciences and Engineering Research Council of Canada and the University of Victoria to pursue this endeavour.

DEDICATION

To my parents *P. Seelawathie* and *Sarath N. Edussooriya*

and

to the teacher *Mr. Sisila R. Perera*,
who taught me ABCs of Electrical and Electronic Science
when I was a Grade 8 student.

Chapter 1

Introduction

Multidimensional signal processing techniques are employed in such fields as wireless communications, image processing, video processing and directional audio systems [1][2][3][4][5]. Recently, these techniques are considered to be employed in the development of the next generation radio telescopes such as the Square Kilometre Array (SKA) [6][7][8][9] to meet the unprecedented technical challenges. The SKA will be an ultrasensitive aperture synthesis radio telescope that is to be built to expose the most important phenomena in the Universe that cannot be successfully investigated with the current generation radio telescopes. As the name itself implies, the SKA will have an aggregate collecting area of up to 10^6 m^2 or 1 km^2 spread over an area about 3000 km in extent, and will facilitate for observations over the radio frequency band from 70 MHz to 30 GHz [6]. Figure 1.1 illustrates an artist's impression of the core of a provisional array configuration (in the form of a log-spiral with a dense core) of the SKA.

The five SKA Key Science Programs, goals of which are: probing the dark ages; studies of galaxy evolution, cosmology and dark energy; studies of the origin and evolution of cosmic magnetism; strong field tests of gravity using pulsars and black holes to verify the general theory of relativity; and search for the cradle of life, have been recognized as observations that are necessary to make fundamental progress in currently unanswered questions in fundamental physics or astrophysics [10]. To facilitate these programs, the SKA will need to provide unprecedented sensitivities, survey speeds and angular resolutions [11](pp. 20). In addition to the five SKA Key Science Programs, the design and development of the SKA have *Exploration of the Unknown* as a philosophy, and it has been included as the sixth SKA Key Science Program to address outstanding questions in the period 2020–2050 and beyond, many

Figure 1.1: An artist's impression of the core of the SKA (Created by - Xilostudios, Source - http://www.jb.man.ac.uk/~pulsar/)

of which are probably not even known today [7][11](pp. 16).

For the SKA Key Science Programs that require observations at frequencies below $\sim$1.5 GHz, *survey speed* is a key specification and prefers antenna designs with large instantaneous fields of view (FoVs) [6]. For the so-called *lower mid-band* of the SKA (0.5–1.5 GHz), dense aperture arrays (DAAs) and focal plane arrays (FPAs) mounted on the focal planes of paraboloidal reflectors are considered as a means of expanding the instantaneous FoV [6][7][8][11](pp. 31–35). In general, DAAs and FPAs are comprised of closely packed wavelength-scale broadband (BB) elemental antennas such as Vivaldi antennas [12]. Research and development of DAAs and FPAs have been carried out in a number of pathfinder projects of the SKA. For example, DAAs are employed in the Thousand Element Array (THEA) [13][14] and Electronic Multi-Beam Radio Astronomy Concept (EMBRACE) [15][16] demonstrators being carried out in Europe. Counterpart demonstrators that employ FPAs are: the Phased-Array Feed Demonstrator (PHAD) [17][18][19] and the Advanced Focal Array Demonstrator (AFAD) [20] in Canada, the Aperture Tile In Focus (APERTIF) [21][22] in the Netherlands and the Australian Square Kilometre Array Pathfinder (ASKAP) [23][24] in Australia. Figures 1.2(a) and 1.2(b) show four THEA tiles and PHAD, respectively. In addition to contribution for the SKA, FPAs are being considered to retrofit exist-

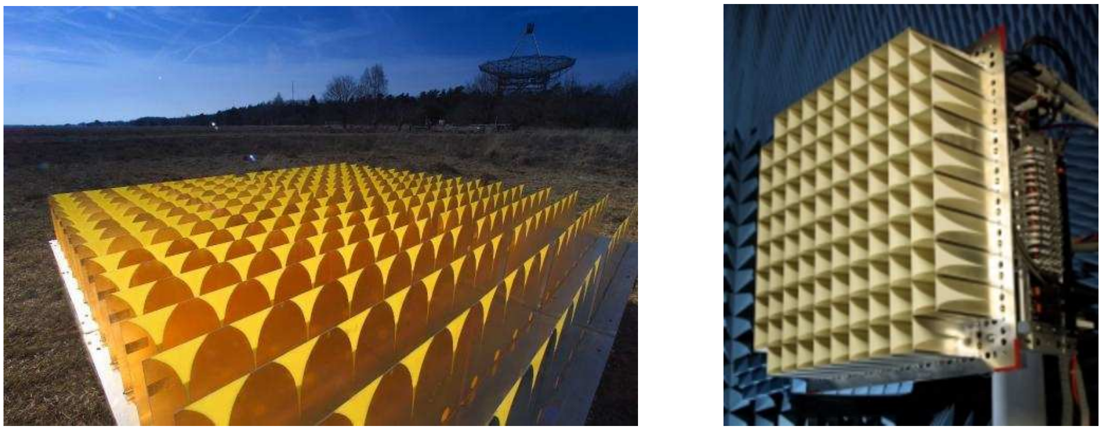

(a) (b)

Figure 1.2: (a) Four THEA tiles each of which consists of 64 Vivaldi antennas (Source - http://www.astron.nl/r-d-laboratory/ska/thea/thea) (b) PHAD, which consists of 180 Vivaldi antennas, undergoing tests in an indoor antenna test facility (Source - http://www.nrc-cnrc.gc.ca/eng/projects/hia/phased-array.html).

ing large radio telescopes to increase survey speeds, e.g., the APERTIF demonstrator for the Westerbork Synthesis Radio Telescope (WSRT) [22][25].

Each elemental antenna in a DAA or an FPA is connected to an LNA and the output of each LNA is subjected to analog preprocessing prior to analog-to-digital conversion and subsequent digital signal processing. *Because of small random perturbations and tolerances in elemental-antenna and circuit parameters, the transfer functions of elemental antennas in DAAs and FPAs and the transfer functions of receivers connected to them are slightly mismatched.* In [26][27][28][29][30][31], the impact of non-idealities in the receiver subsystem and that of mismatches and mutual coupling in the antenna subsystem on the performance are thoroughly analyzed for aperture synthesis interferometric radiometers used in remote sensing [32]. In the context of aperture synthesis radio telescopes, Thompson and D'Addario [33] have analyzed and estimated loss in sensitivity and the introduction of errors in the calibration procedure due to various non-idealities and mismatches in radio frequency (RF) and intermediate frequency (IF) amplifiers and transmission lines and due to delay errors for the Very Large Array (VLA) radio telescope [34]. *Nonetheless, there appears to be little analytical information in the literature about how parameter perturbations and mismatches among the LNAs and anti-aliasing filters (AAFs) employed in analog receiver channels impact upon the brightness distribution (BD) of a synthesized image. Although BD errors due to those non-idealities and mismatches may be* *mostly eliminated through calibration techniques [35](chs. 10 and 11)[36](ch. 9), it is important to understand their characteristics for proper and efficient usage of these techniques.*

The main figure of merit that indicates the performance of a radio telescope is the *system sensitivity*, which is defined as [9]

$$S_{sys} \triangleq \frac{A_e}{T_{sys}}, \tag{1.1}$$

where A_e is the effective collecting area (m^2) and T_{sys} is the system-equivalent noise temperature (K), which is given by the sum of the equivalent temperatures of thermal noise of the antennas, LNAs and the rest of the receiver, radio frequency interfering (RFI) signals, atmosphere noise, and cosmic background noise [37](ch. 2). In fact, the system sensitivity is an indicator of the strength of the weakest, unresolved (point-like) source that can be detected in a given observing time [6]. Furthermore, the survey speed figure of merit of a radio telescope is proportional to $(A_e/T_{sys})^2$ [6]. *Obviously, if T_{sys} can be reduced, A_e can be reduced without degrading the system sensitivity and the survey speed. Therefore, the number of antennas necessary to achieve a given system sensitivity and a given survey speed is reduced. Alternatively, for a given A_e, the system sensitivity and the survey speed can be increased by reducing T_{sys}.*

The design and construction of the SKA involve technical as well as economical challenges. A number of research and development teams around the world have been working on several areas to develop new algorithms and techniques in number of areas [7][9][11]. In the context of signal processing, with the emergence of DAAs and FPAs, three-dimensional (3D) spatio-temporal (ST) cone and frustum filters have been proposed to employ in radio astronomy applications as a means to improve the system sensitivity and survey speed of radio telescopes by attenuating terrestrial RFI signals and various types of noise signals [38][39][40][41][42][43][44](ch. 5). In contrast to previously reported techniques [45][46][47][48][49][50][51][52], which are mostly suitable for processing of temporally narrowband signals, the ST filtering approach with cone and frustum filters is inherently capable of processing temporally BB signals, which is often the case of signals of interest (SOIs) for the SKA. Furthermore, this led to satisfactory results with respect to the improvement in signal-to-interference-plus-noise ratio (SINR), but tends to be computationally intensive. Consequently, much research and development effort is necessary to reduce the computational complexity of cone and frustum filters to a satisfactory level to make them feasible to be employed in the SKA as well as other applications such as wireless communications.

1.1 Contributions of the Thesis

In this thesis, two computationally efficient 3D ST FIR cone filter bank structures are proposed following [3][53] to improve the computational efficiency of the 3D ST FIR cone filter bank structure proposed in [38](ch. 5.5)[39]. Furthermore, we extend this approach to design 3D ST FIR frustum filter banks, having double-frustum-shaped passbands oriented along the temporal axis, from the proposed 3D ST FIR cone filter banks without compromising the computational efficiency. Both types of cone and frustum filter banks are almost alias free and provide near-perfect reconstruction. In the proposed cone and frustum filter banks, both temporal and spatial filtering operations can be carried out at a significantly lower rate compared to the original cone filter bank implying lower power consumption. Furthermore, it is numerically confirmed that the proposed cone and frustum filter banks provide a significant reduction of the computational complexity without deteriorating the improvement in SINR by means of illustrative examples involving the attenuation of strong BB terrestrial RFI signals received by DAAs and FPAs.

The other contribution of the thesis is a theoretical analysis of BD errors caused by parameter perturbations and mismatches among the ideally-matched transfer functions of receivers employed in synthetic aperture systems. For simplicity, we consider one-dimensional (1D) aperture synthesis with a synthetic aperture system consisting of 1D dense linear arrays (DLAs), which mimic the 1D version of more general two-dimensional (2D) DAAs. However, the extension of the analysis from 1D to 2D aperture synthesis is straightforward. The analysis is mainly divided into two parts. First, we consider the BD errors caused by perturbations in the transfer functions of LNAs and AAFs. For LNAs and AAFs, those perturbations are primarily caused by process variations in manufacturing [54][55] and typical element tolerances [56](ch. 7), respectively. Here, we present a detailed analysis of characteristics of the *additive BD error* and its effects on the *synthesized BD* under three cases: completely matched, partially matched and unmatched transfer functions of the LNAs and AAFs. Second, we examine the conditions under which the BD errors caused by the phase responses of 2D beamformers vanish. Here, we show that the sufficient condition to vanish the BD errors due to the phase responses is that the transfer functions of the 2D beamformers are matched and the phase responses are not necessary to be linear.

This important result suggests an interesting potential application for infinite impulse response (IIR) beamformers because they are arithmetically- and hardware-wise less complex than finite impulse response (FIR) counterparts. Furthermore, a numerical study of the BD errors due to the typical tolerances of the passive L and C elements used to implement the AAFs and due to the variation of gain from LNA to LNA is presented. The percentage error of the synthesized BDs for the partially matched and unmatched cases is substantial at frequencies near the passband edge of the AAFs. The variation of the percentage error due to the random variations of the gains of the LNAs is random and entirely depends on the additive perturbations for both partially matched and unmatched cases. Furthermore, the maximum percentage error due to the typical tolerances of passive L and C elements of AAFs is greater than that due to the random variations of the gains of the LNAs.

1.2 Outline of the Thesis

The rest of the thesis is organized as follows. In Chapter 2, ST modeling and analog preprocessing of the signals on DAAs and FPAs are reviewed. In Section 2.2, ST modeling and the spectra of SOIs and RFI signals received by DAAs and FPAs are discussed. In Section 2.3, spatial sampling of SOIs and RFI signals and the finite aperture effect are reviewed. Analog preprocessing and temporal sampling of DAA and FPA signals are discussed in Section 2.4.

In Chapter 3, two computationally efficient 3D ST FIR cone filter bank structures are presented. In Section 3.2, a review of the 3D cone filter bank structure proposed in [38](ch. 5.5)[39] is presented. Next, the proposed computationally efficient cone filter bank structures are described in Sections 3.3 and 3.4. Then, the strategy that can be used to design the 3D ST FIR frustum filter banks from the respective 3D ST FIR cone filter banks without compromising the computational efficiency is described in Section 3.5. In Section 3.6, performance of the proposed filter bank structures, in terms of the achievable improvement in SINR and computational complexity, is compared with the performance of the original filter bank structure.

In Chapter 4, BD errors caused by parameter perturbations and mismatches among the transfer functions of receivers employed in synthetic aperture systems are examined. In Section 4.2, an idealized model of a 2D synthetic aperture system is reviewed. The theoretical analysis of BD errors caused by perturbations in the receiver transfer functions is presented in Section 4.3. In Section 4.4, the BD errors caused by the typical tolerances of passive L and C elements used to implement LC AAFs and the random variations of gain from LNA to LNA are numerically studied.

Finally, in Chapter 5, concluding remarks and future work are presented.

Chapter 2

Spatio-Temporal Modeling and Analog Preprocessing of Signals on Dense Aperture Arrays and Focal Plane Arrays

2.1 Introduction

In this chapter, ST modeling and analog preprocessing of signals on DAAs and FPAs are reviewed. We mainly consider SOIs emanating from cosmic sources and natural or artificial terrestrial RFI signals. Cosmic SOIs are generated by natural processes such as the synchrotron mechanism, in which high-energy electrons in magnetic fields radiate as a result of their orbital motion [35](ch. 1.2). Terrestrial RFI signals mainly consist of electromagnetic (EM) radiation from the electronic systems within the sites of radio telescopes themselves and from commercial broadcasting and wireless communication transmissions [38](ch. 3.2)[40].

The organization of the chapter is as follows. In Section 2.2, ST modeling and the spectra of SOIs and RFI signals received by DAAs and FPAs are discussed. In Section 2.3, spatial sampling of SOIs and RFI signals and the finite aperture effect are reviewed. Analog preprocessing and temporal sampling of DAA and FPA signals are discussed in Section 2.4. Finally, summary of the chapter is presented in Section 2.5.

2.2 Spatio-Temporal Modeling and the Spectra of Signals of Interest and Terrestrial Radio Frequency Interfering Signals Received by DAAs and FPAs

The wavefronts of a propagating EM wave emanating from a *point* source in the far field effectively lie in planes as shown in Figure 2.1. Therefore, over a finite area, the EM wave can be very closely approximated as a four-dimensional (4D) continuous-domain (CD) spatio-temporal[1] (ST) plane wave (PW) [57]. This ST PW approximation can be used to model the signals of interest (SOIs) coming from cosmic sources of very small angular diameter on the surface of the Earth [58](pp. 296)[35](pp. 16) and natural or artificial terrestrial RFI signals received by DAAs and FPAs [38](ch. 3.2)[40].

An *ideal* 4D CD ST PW can be expressed in the form

$$pw_{4\mathrm{C}}(x, y, z, \mathrm{c}t) = w_{\mathrm{C}}(d_x x + d_y y + d_z z + \mathrm{c}t), \tag{2.1}$$

where $\hat{\mathbf{d}} = [d_x\ d_y\ d_z]^{\mathrm{T}}$ is the unit vector that specifies the direction of arrival (DOA) in the 3D space $(x, y, z) \in \mathbb{R}^3$, $t \in \mathbb{R}$ is the time, c is the constant speed of propagation and $w_{\mathrm{C}}(s)|\ \forall\, s = d_x x + d_y y + d_z z + \mathrm{c}t \in \mathbb{R}$ is the 1D temporal function that describes the amplitude of the wavefronts in the DOA [4]. Note that $pw_{4\mathrm{C}}(x, y, z, \mathrm{c}t)$ is assumed to be a mono polarized wave, hence, it is treated as a scalar quantity. As shown in Figure 2.1, the DOA can also be specified in terms of the inclination angle θ and azimuth angle ϕ, such that

$$[d_x\ d_y\ d_z]^{\mathrm{T}} \equiv [\sin(\theta)\cos(\phi) \quad \sin(\theta)\sin(\phi) \quad \cos(\theta)]^{\mathrm{T}}, \tag{2.2}$$

where $\theta \in [0^\circ, 180^\circ]$ and $\phi \in [0^\circ, 360^\circ)$.

---

[1] A spatio-temporal signal is a multidimensional signal that is a function of at least one spatial dimension in the 3D space and one temporal dimension. The term “temporal” indicates time or a dimension proportional to time.

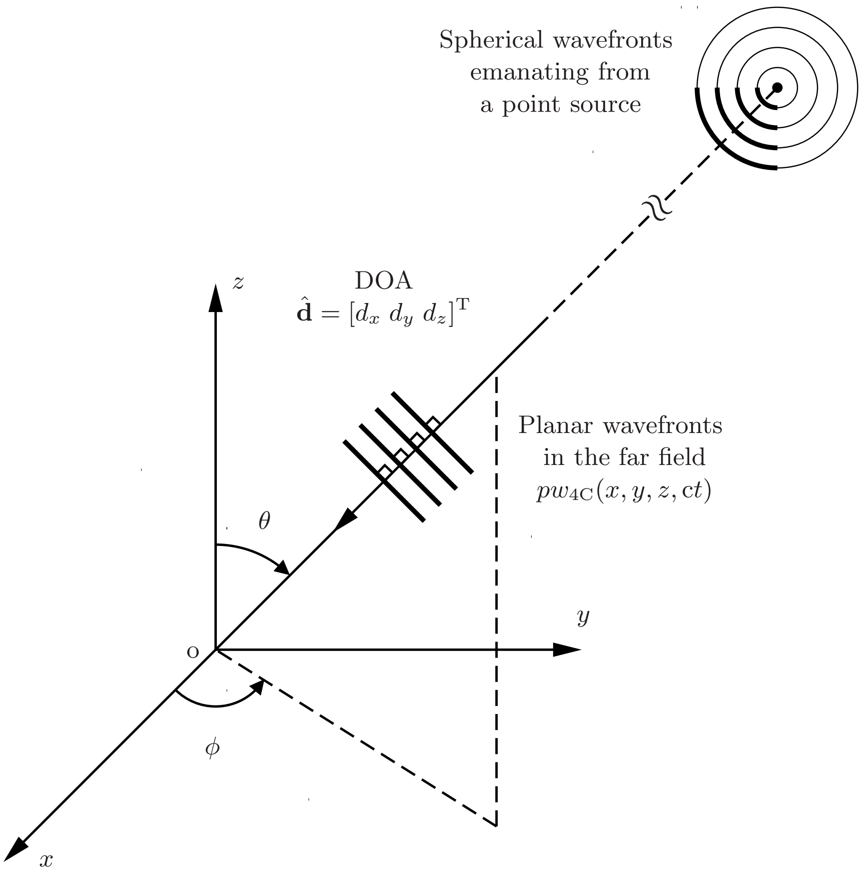

Figure 2.1: A propagating EM wave emanating from a point source in the far field, where the unit vector $\hat{\mathbf{d}} = [d_x\ d_y\ d_z]^{\mathrm{T}}$ specifies the DOA. Note that the direction of $\hat{\mathbf{d}}$ is opposite to the direction of propagation.

2.2.1 Spatio-Temporal Plane Waves Observed on the $z = 0$ Plane and Their CD Spectra

Let us consider the case illustrated in Figure 2.2 (a), where a 4D CD ST PW propagating in the 3D space is observed on the $z = 0$ plane. Then, the resulting 3D CD ST PW $pw_{3\mathrm{C}}(x, y, \mathrm{c}t)$ can be expressed in the form

$$\begin{aligned} pw_{3\mathrm{C}}(x, y, \mathrm{c}t) &= pw_{4\mathrm{C}}(x, y, 0, \mathrm{c}t) \\ &= w_{\mathrm{C}}(d_x x + d_y y + \mathrm{c}t). \end{aligned} \tag{2.3}$$

The 3D continuous-domain Fourier transform (CDFT) of $pw_{3\mathrm{C}}(x, y, ct)$ is given by [38] (ch. 3.4)[40][44](ch. 2.3.2)

$$PW_{3\mathrm{C}}(\Omega_x, \Omega_y, \Omega_{ct}) = W_{\mathrm{C}}(\Omega_{ct})\delta(\Omega_x - \sin(\theta)\cos(\phi)\Omega_{ct})\delta(\Omega_y - \sin(\theta)\sin(\phi)\Omega_{ct}), \tag{2.4}$$

where $(\Omega_x, \Omega_y, \Omega_{ct}) \in \mathbb{R}^3$, $W_{\mathrm{C}}(\Omega_{ct})$ is the 1D CDFT of $w_{\mathrm{C}}(ct)$ and $\delta(\cdot)$ is the 1D CD impulse function. Note that $\Omega_{ct} = \Omega_t/\mathrm{c}$, and the units of Ω_{ct} and Ω_t are rad/m and rad/s, respectively. The region of support[2] (ROS) of $PW_{3\mathrm{C}}(\Omega_x, \Omega_y, \Omega_{ct})$ lies on a *straight line* [4] going through the origin of the 3D frequency space [60]. This straight line corresponds to the line of intersection of the two 3D planes $\Omega_x - \sin(\theta)\cos(\phi)\Omega_{ct} = 0$ and $\Omega_y - \sin(\theta)\sin(\phi)\Omega_{ct} = 0$. The angle α between the straight line and the Ω_{ct} axis and the angle β between the projection of the straight line onto the plane $\Omega_{ct} = 0$ and the Ω_x axis, shown in Figure 2.2 (b), are given by [38](ch. 3.4)[40][44](ch. 2.3.2)

$$\alpha = \tan^{-1}(\sin(\theta)) \tag{2.5a}$$

$$\beta = \phi. \tag{2.5b}$$

The ROS of $PW_{3\mathrm{C}}(\Omega_x, \Omega_y, \Omega_{ct})$ depends on the frequency content of $w_{\mathrm{C}}(ct)$ and occupies a segment(s) on the straight line. For example, the ROS is comprised of two distinct straight line segments for a 3D ST *bandpass* PW as shown in Figure 2.2 (b). In the case of a *purely monochromatic* signal, the ROS becomes two points in the 3D frequency space.

In the case of a radio telescope located on the Earth, the observable space is the upper hemisphere; Therefore, the range of θ is effectively limited to $[0°, 90°]$. According to Equations (2.5a) and (2.5b), the ROSs of all possible 3D ST PWs for $\theta \in [0°, 90°]$ and $\phi \in [0°, 360°)$ lie on or inside the surface of a double-cone section having a half-cone angle $\alpha_{max} = 45°$ [38](ch. 3.4)[40][44](ch. 2.3.2).

2.2.2 The Effect of Effective Fields of View of DAAs on the ROSs of the Spectra of SOIs and RFI Signals

Ideally, the SOIs emanating from the cosmic sources in the entire upper hemisphere of the visible sky can be observed by means of DAAs with the largest possible FoV with

---

[2] By definition, the region of support of a function is the region of its domain where the function is defined to be *nonzero* [59](ch. 1).

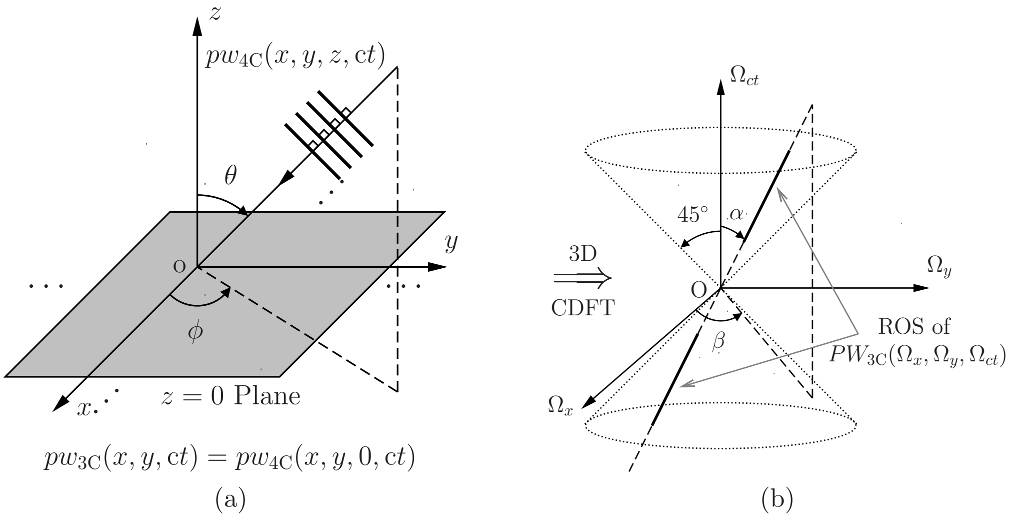

Figure 2.2: (a) A 4D CD ST PW $pw_{4C}(x,y,z,ct)$ observed on the $z=0$ plane (b) the ROS of $PW_{3C}(\Omega_x,\Omega_y,\Omega_{ct})$, the spectrum of the corresponding 3D CD ST PW $pw_{3C}(x,y,ct)$. For a 3D ST bandpass PW, the ROS is comprised of two distinct straight line segments.

$\theta \in [0°,90°]$ and $\phi \in [0°,360°)$ [40]. However, in practice, the effective FoV is limited to the angular range $\theta \in [0°,\theta_{Dmax}]$, where θ_{Dmax} is the maximum inclination scan angle of the DAA sky beam. This is due to the reduction of the effective aperture with increased θ, ground clutter and terrestrial RFI signals arriving with inclination angles $\theta > 80°$ [38](ch. 3)[40]. For example, θ_{Dmax} corresponding to the FoVs to be achieved with DAAs in the SKA phase 1 and phase 2 are 45° and 60°, respectively [11](pp. 28). The corresponding α_{Dmax} are 35.3° and 40.9°, respectively. *For such FoVs, ideally, the ROSs corresponding to the spectra of the SOIs and those corresponding to the terrestrial RFI signals do not overlap as illustrated in Figure 2.3.* This property will be used to significantly attenuate the terrestrial RFI signals with low distortion on the SOIs using 3D ST cone and frustum filters having double-cone-shaped and double-frustum-shaped passbands, respectively, as will be shown in Chapter 3.

2.2.3 Dish-Reflected Broadband SOIs on the Focal Plane of a Paraboloidal Reflector and Their CD Spectra

Here, the EM field on the focal plane of a paraboloidal reflector due to dish-reflected BB ST PWs and its CD spectrum [40][44](ch. 3.2) is reviewed. For simplicity, a circular-aperture prime-focus paraboloidal reflector [61](ch. 2) of focal length F and

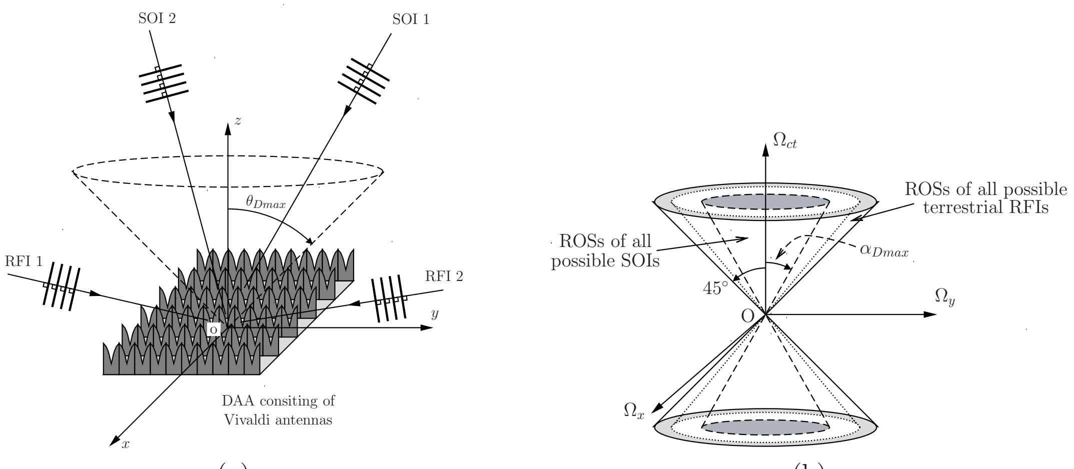

(a) (b)

Figure 2.3: (a) Cosmic SOIs and RFI signals on a DAA. The terrestrial RFI signals arrive the DAA with inclination angles $\theta > 80°$, and the effective FoV is given by $\theta \in [0°, \theta_{Dmax}]$ and $\phi \in [0°, 360°)$ [38](ch. 3)[40]. (b) The ROSs of the spectra of the SOIs and terrestrial RFI signals in the 3D frequency space.

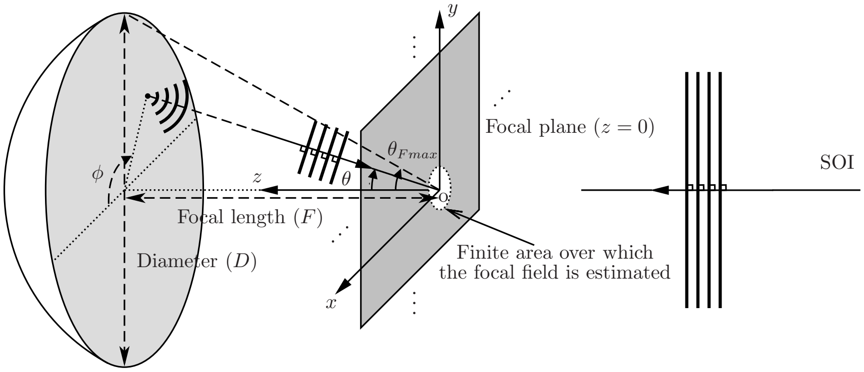

Figure 2.4: The SOI induces surface currents on the inner-surface of the paraboloid reflector, which in turn behave as point sources that radiate spherical wavefronts towards the focal region.

diameter D is assumed. Let us consider the case where a BB ST PW SOI emanating from a cosmic source in the *broadside direction* is received by a paraboloidal reflector as shown in Figure 2.4. The SOI induces surface currents on the ideally conducting inner-surface of the paraboloid reflector, which in turn behave as *point sources* that radiate spherical wavefronts towards the focal region according to the "Huygens' Principle" [61](ch. 3)[62](ch. 5). These spherical wave fronts can be approximated as *infinitesimal* 3D ST PWs over a finite area around the focal point on the focal plane [44](ch. 3.2). Consequently, the EM field $fp_{3C}(x, y, ct)$ over this area is formed by the superposition (i.e., diffraction interference) of such infinitesimal 3D ST PWs which radiate from all points on the paraboloidal reflector; that is,

$$fp_{3\mathrm{C}}(x, y, \mathrm{c}t) = \sum_{\theta} \sum_{\phi} pw_{3\mathrm{C}}^{\theta,\phi}(x, y, \mathrm{c}t), \tag{2.6}$$

where $pw_{3\mathrm{C}}^{\theta,\phi}(x, y, ct)$ is given by Equation (2.3), and θ and ϕ are, respectively, the inclination and azimuth angles of the point source with respect to the focal point [40][44](ch. 3.2). Furthermore, for all the point sources on the surface of the paraboloidal reflector, the inclination angle varies over the range $\theta \in [0°, \theta_{Fmax}]$, where θ_{Fmax} is the *subtended angle*[3] of the paraboloidal reflector that is given by [63](ch. 15.4)

$$\theta_{Fmax} = \tan^{-1} \left| \frac{\frac{1}{2}\left(\frac{F}{D}\right)}{\left(\frac{F}{D}\right)^2 - \frac{1}{16}} \right|, \tag{2.7}$$

and the azimuth angle varies over the range $\phi \in [0°, 360°)$ [40][44](ch. 3.2). For all combinations of θ and ϕ, the 1D wave-front signals $w_{\mathrm{C}}^{\theta,\phi}(\cdot)$ corresponding to $pw_{3\mathrm{C}}^{\theta,\phi}(x, y, \mathrm{c}t)$ have almost identical magnitudes but different delays relative to the impinging SOI [40]. Consequently, the radiated signal power is concentrated onto regions of the focal plane [40] that are called *focal spots* [61](ch. 3.8)[63](ch. 15.4). The focal spot corresponding to an SOI emanating from the broadside direction is located at the focal point of the paraboloidal reflector [44](ch. 5.4).

To determine the ROS of the CD spectrum of $fp_{3\mathrm{C}}(x, y, \mathrm{c}t)$, we first write its 3D CDFT as

$$FP_{3\mathrm{C}}(\Omega_x, \Omega_y, \Omega_{ct}) = \sum_{\theta} \sum_{\phi} PW_{3\mathrm{C}}^{\theta,\phi}(\Omega_x, \Omega_y, \Omega_{ct}), \tag{2.8}$$

where $PW_{3\mathrm{C}}^{\theta,\phi}(\Omega_x, \Omega_y, \Omega_{ct})$ is the 3D CDFT of $pw_{3\mathrm{C}}^{\theta,\phi}(x, y, \mathrm{c}t)$. As discussed in Section 2.2.1, the ROS of $PW_{3\mathrm{C}}^{\theta,\phi}(\Omega_x, \Omega_y, \Omega_{ct})$ lies on a straight line going through the origin of the 3D frequency space, and the orientation of the straight line is specified by the angles α and β that depend on θ and ϕ, respectively, as given by Equations (2.5a) and (2.5b), respectively. According to Equation (2.8), the ROS of $FP_{3\mathrm{C}}(\Omega_x, \Omega_y, \Omega_{ct})$ is given by the superposition of the ROSs of $PW_{3\mathrm{C}}^{\theta,\phi}(\Omega_x, \Omega_y, \Omega_{ct})$ implying a solid

---

[3] Note that, θ_{Fmax} is also referred to as the spill over angle [38] and the aperture half-angle [61](ch. 2).

double-conic section having a half-cone angle [40][44](ch. 3.2)

$$\alpha_{Fmax} = \tan^{-1}(\sin(\theta_{Fmax})). \tag{2.9}$$

Note that, the paraboloidal reflectors proposed for the SKA have F/D ratio in the range 0.4 to 0.6 [9] implying $\alpha_{Fmax} \in (35^\circ, 42^\circ)$.

2.2.4 The Effect of Effective Fields of View of FPAs on the ROSs of the Spectra of SOIs and RFI Signals

As mentioned in the previous subsection, the focal spot corresponding to an SOI emanating from the broadside direction is located at the focal point of the paraboloidal reflector. However, in the case of an SOI emanating from a direction other than the broadside direction, the position of the corresponding focal spot moves away from the focal point, in the opposite direction to the direction of the SOI as it moves away from the broadside direction [64], as illustrated in Figure 2.5 (a). The effective FoV of an FPA mounted on a paraboloidal reflector is determined by the dimensions of the paraboloidal reflector and the size of the FPA [64]. For example, the effective FoV of an FPA of size 1.8×1.8 m^2 mounted on a paraboloidal reflector of focal length 6.75 m and diameter 15 m is a $5^\circ \times 5^\circ$ square in the sky at 500 MHz [44](ch. 5.3). Note that, in the case of FPAs, the effective FoVs are considerably lower compared to those of DAAs. If the deviation of the DOA of an SOI from the broadside direction is less than 3.5°, the ROS of the spectrum of the corresponding EM field on the focal plane is almost the same as the ROS of the spectrum of the EM field corresponding to an SOI emanating from the broadside direction [44](ch. 3.2), i.e., a solid double-conic section having a half-cone angle $\alpha_{Fmax} = \tan^{-1}(\sin(\theta_{Fmax})$. Similar to DAAs, the terrestrial RFI signals are, in most cases, received by FPAs directly, i.e., without being reflected from the paraboloidal reflector, with inclination angles $\theta > 75^\circ$ [38](ch. 3)[40]. *Consequently, the ROSs corresponding to the spectra of the SOIs and those corresponding to the terrestrial RFI signals do not overlap under ideal conditions* as illustrated in Figure 2.5 (b). As in the case of DAAs, this property will be used to significantly attenuate the terrestrial RFI signals with low distortion on the SOIs using 3D ST cone and frustum filters having double-cone-shaped and double-frustum-shaped passbands, respectively, as will be shown in Chapter 3.

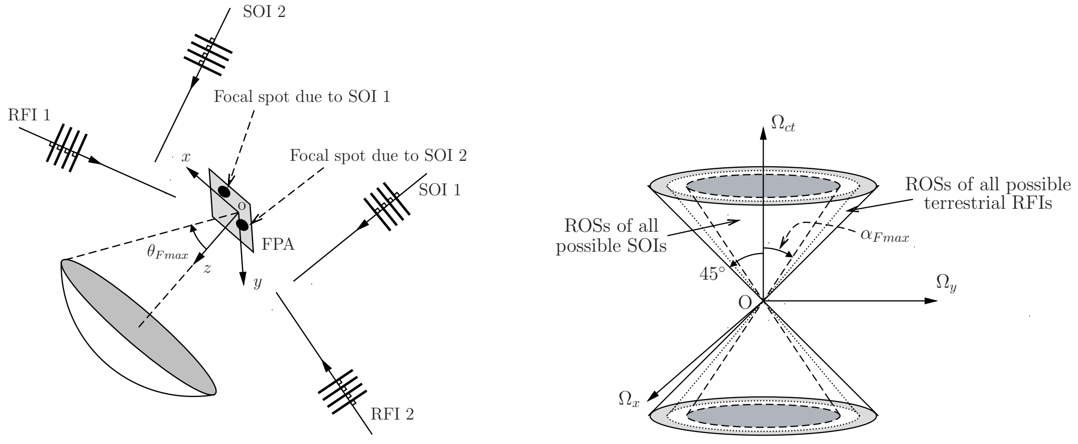

(a) (b)

Figure 2.5: (a) Cosmic SOIs and RFI signals on an FPA. The terrestrial RFI signals arrives the FPA with inclination angles $\theta > 75°$ [38](ch. 3)[40]. (b) The ROSs of the spectra of the SOIs and terrestrial RFI signals in the 3D frequency space.

2.3 Spatial Sampling of SOIs and RFI Signals Received by DAAs and FPAs

The elemental antennas of DAAs and FPAs are mostly arranged rectangularly [13][15] [17][21] although other geometric arrangements such as hexagonal can also be employed [65]. In the following discussion, only the rectangular arrangement of the elemental antennas is considered. According to the 2D sampling theorem [1](ch. 1.4)[2](ch. 2.1), the sampling distances along the x and y dimensions T_x and T_y, respectively, should be chosen such that

$$T_x \leq \frac{\mathrm{c}}{2\max[f_{\mathrm{soi}}]} \tag{2.10a}$$

$$T_y \leq \frac{\mathrm{c}}{2\max[f_{\mathrm{soi}}]} \tag{2.10b}$$

to avoid spatial aliasing in the interested temporal frequency range of the SOIs, where $\max[f_{\mathrm{soi}}]$ is the maximum temporal frequency, measured in Hz, in the *interested temporal bandwidth*. Note that $\max[f_{\mathrm{soi}}]$ *is not* the maximum temporal frequency of the SOIs but the maximum temporal frequency in the interested temporal bandwidth. For example, if the bandwidth of the SOIs is 0.3–10 GHz and the interested temporal bandwidth is 0.5–1.5 GHz, $\max[f_{\mathrm{soi}}] = 1.5$ GHz. In addition to the SOIs, the RFI signals may contain temporal frequencies higher than $\max[f_{\mathrm{soi}}]$. The sections of spectra corresponding to the temporal frequencies higher than $\max[f_{\mathrm{soi}}]$ are vulnerable to spatial aliasing [44](ch. 2.6)[66](ch. 2.3.2). This is further discussed in the next paragraph with the aid of the 3D mixed domain Fourier transform (MDFT).

The 3D ST signals at the outputs of the elemental antennas in the DAAs and FPAs are 3D mixed domain (MD)(i.e., continuous in the temporal dimension and discrete in the spatial dimension(s)) signals. The *spatially sampled (by a DAA)* 3D MD ST PW corresponding to a 3D CD ST PW is defined by

$$\begin{aligned} pw_{3\mathrm{M}}(n_x, n_y, \mathrm{c}t) &= pw_{3\mathrm{C}}(n_x T_x, n_y T_y, \mathrm{c}t) \\ &= w_{\mathrm{C}}(d_x n_x T_x + d_y n_y T_y + \mathrm{c}t), \end{aligned} \tag{2.11}$$

where $(n_x, n_y, \mathrm{c}t) \in \mathbb{Z}^2 \times \mathbb{R}$. (At the moment, let us assume that the DAA has an infinite number of elemental antennas that are arranged rectangularly, i.e., an infinite-extent aperture.) The 3D MDFT of $pw_{3\mathrm{M}}(n_x, n_y, ct)$ is defined by

$$PW_{3\mathrm{M}}(\omega_x, \omega_y, \Omega_{ct}) \triangleq \sum_{n_x=-\infty}^{\infty} \sum_{n_x=-\infty}^{\infty} \int_{\mathrm{c}t=-\infty}^{\infty} pw_{3\mathrm{M}}(n_x, n_y, \mathrm{c}t)\, \mathrm{e}^{-j(\omega_x n_x + \omega_y n_y + \Omega_{ct}\mathrm{c}t)}\, \mathrm{d}(\mathrm{c}t), \tag{2.12}$$

where $(\omega_x, \omega_y, \Omega_{ct}) \in \mathbb{R}^3$ [59](ch. 6). Note that, although the typical elemental antennas employed in the DAAs and FPAs (such as Vivaldi antennas) are directional, for simplicity of the analysis, we assume that the elemental antennas have *isotropic* radiation patterns [63](ch. 2.2). Further, we ignore mutual coupling among the elemental antennas. According to [1](ch. 1.4)[2](ch. 2.1), $PW_{3\mathrm{M}}(\omega_x, \omega_y, \Omega_{ct})$ may be expressed in the form

$$PW_{3\mathrm{M}}(\omega_x, \omega_y, \Omega_{ct}) = \frac{1}{T_x T_y} \sum_{k_x=-\infty}^{\infty} \sum_{k_y=-\infty}^{\infty} PW_{3\mathrm{C}}\left(\frac{\omega_x - 2\pi k_x}{T_x}, \frac{\omega_y - 2\pi k_y}{T_y}, \Omega_{ct}\right), \tag{2.13}$$

where $\omega_i = \Omega_i T_i$, $i = x, y$. Consequently, $PW_{3\mathrm{M}}(\omega_x, \omega_y, \Omega_{ct})$ may be considered as a periodic extension of $PW_{3\mathrm{C}}\left(\frac{\omega_x}{T_x}, \frac{\omega_y}{T_y}, \Omega_{ct}\right)$ on the $\Omega_{ct} = 0$ plane with the periodicity $2\pi \times 2\pi$ in the $(\omega_x, \omega_y, \Omega_{ct}) \in \mathbb{R}^3$ space. Furthermore, the ROS of $PW_{3\mathrm{M}}(\omega_x, \omega_y, \Omega_{ct})$ is the periodic extension of that of $PW_{3\mathrm{C}}\left(\frac{\omega_x}{T_x}, \frac{\omega_y}{T_y}, \Omega_{ct}\right)$ with the same periodicity. Therefore, the ROSs of the MD spectra of two 3D ST PWs having frequencies higher than $\max[f_{\mathrm{soi}}]$ may overlap in the regions marked by hatching in Figure 2.6. Similar

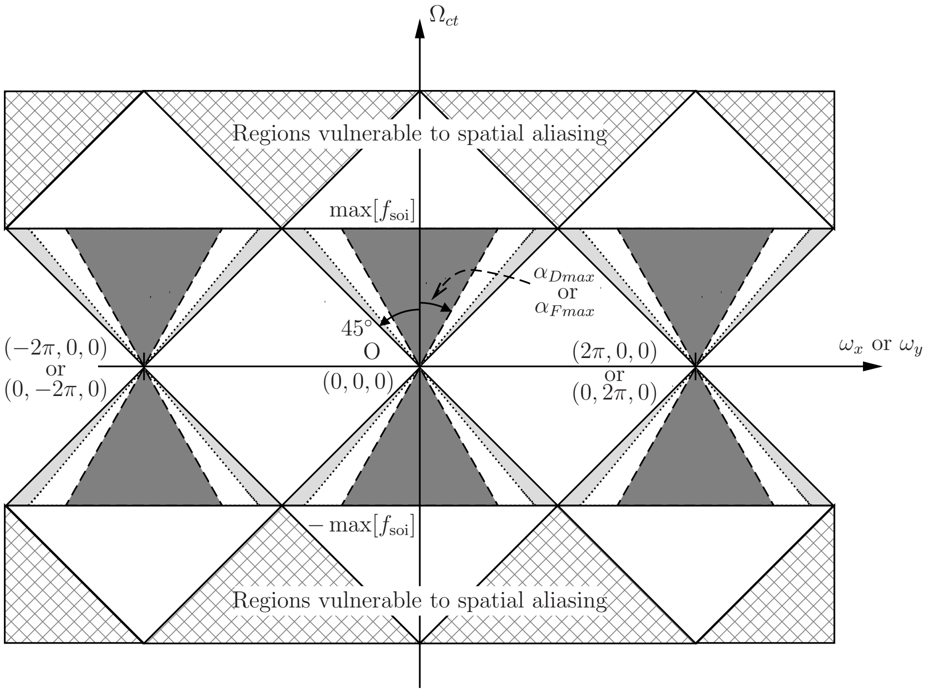

Figure 2.6: Cross sections, on the $\omega_x = 0$ or $\omega_y = 0$ planes, of the ROSs of the 3D MDFTs of the SOIs and RFI signals received by a DAA or an FPA. The part, corresponding to the interested temporal bandwidth, of the ROS of the 3D MDFT of an SOI is within the two fan-shaped areas having half-width angles of α_{Dmax} and α_{Fmax} for the DAA and FPA, respectively. The regions vulnerable to spatial aliasing are marked by hatching [44](ch. 2.6)[66](ch. 2.3.2).

analysis can be applied to the SOIs and RFI signals received by an FPA although, in this case, the SOIs are not 3D ST PWs. Nevertheless, this does not introduce any distortion to the sections of the spectra of the SOIs corresponding to the interested temporal bandwidth. Furthermore, almost all of spectra in the regions vulnerable to spatial aliasing can be attenuated (to the level of the stopband gain) by employing appropriate AAFs as shown in Section 2.4.

In the above discussion, we did not take the *finite-extent aperture* of the DAAs and FPAs into account. Therefore, the ROSs of the 3D MDFTs of spatially sampled signals have been considered as the periodic extensions of the ROSs of their 3D CDFT counterparts on the $\Omega_{ct} = 0$ plane without any distortion. However, with a finite-extent aperture, as is always the case in real DAAs and FPAs, the ROSs of the 3D MDFTs of spatially sampled signals are *spread* around the ideal ROSs along planes parallel to the $\Omega_{ct} = 0$ plane [38](ch. 3.4.2)[44](ch. 2.7). This is known as the *finite aperture effect* and is briefly reviewed in the next subsection.

2.3.1 The Finite Aperture Effect

Let us consider the case where a 4D CD ST PW is received by a DAA having $(2N_x + 1) \times (2N_y + 1)$, where $N_x, N_y \in \mathbb{Z}^+$, elemental antennas arranged rectangularly with the center at the origin. The 3D MD signal at the $(2N_x + 1) \times (2N_y + 1)$ outputs of the elemental antennas, $fpw_{3\mathrm{M}}(n_x, n_y, \mathrm{c}t)$, may be expressed in the form

$$fpw_{3\mathrm{M}}(n_x, n_y, \mathrm{c}t) = pw_{3\mathrm{M}}(n_x, n_y, ct)wn_{2\mathrm{Drec}}(n_x, n_y), \tag{2.14}$$

where $pw_{3\mathrm{M}}(n_x, n_y, \mathrm{c}t)$ is the 3D MD signal corresponding to a hypothetical DAA having an infinite number of elemental antennas arranged rectangularly, and the 2D rectangular window $wn_{\mathrm{rec}}(n_x, n_y)$ is defined by [1](pp. 119)[2](pp. 151)

$$wn_{2\mathrm{Drec}}(n_x, n_y) \triangleq \begin{cases} 1, & |n_x| \leq N_x \text{ and } |n_y| \leq N_y \\ 0, & \text{otherwise.} \end{cases} \tag{2.15}$$

According to [1](pp. 34)[2](pp. 21), Equation (2.14) can be written in terms of their 3D MDFTs as

$$FPW_{3\mathrm{M}}(\omega_x, \omega_y, \Omega_{ct}) = PW_{3\mathrm{M}}(\omega_x, \omega_y, \Omega_{ct}) *** [WN_{2\mathrm{Drec}}(\omega_x, \omega_y)\delta(\Omega_{ct})], \tag{2.16}$$

where $***$ denotes the 3D convolution, and $WN_{2\mathrm{Drec}}(\omega_x, \omega_y)$ alone is the 2D discrete-domain Fourier transform (DDFT) of $wn_{2\mathrm{Drec}}(n_x, n_y)$. By using the relationships in Equations (2.4) and (2.13), Equation (2.16) can be expressed as

$$\begin{aligned} FPW_{3\mathrm{M}}(\omega_x, \omega_y, \Omega_{ct}) = {} & \frac{1}{T_x T_y} \sum_{k_x=-\infty}^{\infty} \sum_{k_x=-\infty}^{\infty} W_{\mathrm{C}}(\Omega_{ct}) \\ & \times WN_{2\mathrm{Drec}}(\omega_x - T_x d_x \Omega_{ct} - 2\pi k_x, \omega_y - T_y d_y \Omega_{ct} - 2\pi k_y), \end{aligned} \tag{2.17}$$

where $d_x = \sin(\theta)\cos(\phi)$ and $d_y = \sin(\theta)\sin(\phi)$. It follows from Equation (2.17) that the ROS of $FPW_{3\mathrm{M}}(\omega_x, \omega_y, \Omega_{ct})$ is spread from the ideal straight lines along planes parallel to the $\Omega_{ct} = 0$ plane. The spreading is mainly determined by the 2D window function, in this case, the 2D rectangular window $wn_{2\mathrm{Drec}}(n_x, n_y)$.

In general, 2D windows are generated from their 1D counterparts [1](pp. 119)[2](pp. 151), hence, 2D windows inherit the properties of 1D counterparts. It is well known that, in general, a 1D DDFT of a 1D window function has one main lobe and many decaying side lobes. The spreading of the ROS of $FPW_{3\mathrm{M}}(\omega_x, \omega_y, \Omega_{ct})$ can be described from these two properties. The 1D rectangular window provides the narrowest main lobe for a given length [67](ch. 9.4). However, it exhibits higher and slowly decaying side lobes compared to other typical window functions [67](ch. 9.4). The magnitude of the 2D DDFT of the 2D rectangular window $((2N_x+1)\times(2N_y+1) = 15 \times 15)$ is shown in Figure 2.7 (a). The higher and slowly decaying side lobes of the 2D rectangular window cause to leak some energy from the passband to the stopband and vice versa. Further, these leakages even introduce spatial aliasing to the regions that were originally free from spatial aliasing due to the periodic nature of the 3D MDFT of $FPW_{3\mathrm{M}}(\omega_x, \omega_y, \Omega_{ct})$. These leakages can be reduced by spatially weighting the $pw_{3\mathrm{M}}(n_x, n_y, \mathrm{c}t)$ by an appropriate 2D window such as the 2D Hamming window at the expense of a wider main lobe compared to that resulting from the 2D rectangular window for the same spatial ROS as illustrated in Figures 2.7 and 2.8. The 2D Hamming window $((2N_x + 1) \times (2N_y + 1) = 15 \times 15)$ is generated as a *separable* window from its 1D counterpart [1](pp. 119)[2](pp. 151) as

$$wn_{s,2\mathrm{DHam}}(n_x, n_y) \triangleq wn_{\mathrm{DHam}}(n_x) wn_{\mathrm{DHam}}(n_y), \qquad |n_x| \leq N_x \text{ and } |n_y| \leq N_y, \tag{2.18}$$

where 1D Hamming window of length N is given by [67](ch. 9.4)

$$wn_{\mathrm{DHam}}(n) \triangleq \begin{cases} 0.54 + 0.46 \cos \frac{2\pi n}{N-1}, & |n| \leq \frac{N-1}{2} \\ 0, & \text{otherwise.} \end{cases} \tag{2.19}$$

It is important to take these *spectral spreading and leakages* into account while designing the 3D ST cone and frustum filters. That is, for example, for DAAs, we may need to employ a cone filter having a little-wider double-cone-shaped passband than that determined by the half-cone angle α_{Dmax} to encompass the main lobes of the ROSs of the SOIs that lie close to the surface of the double-cone section having a half-cone angle α_{Dmax}.

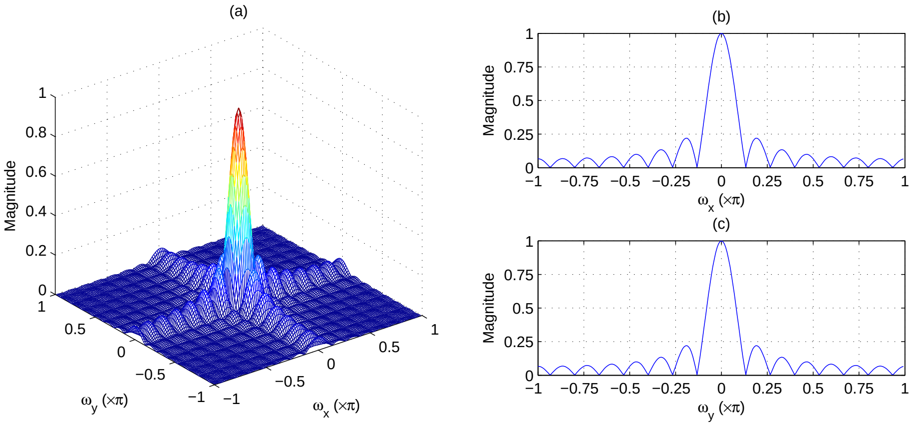

Figure 2.7: (a) Magnitude of the 2D DDFT of the 2D rectangular window $wn_{\text{2Drec}}(n_x, n_y)$, $(2N_x + 1) \times (2N_y + 1) = 15 \times 15$ (b) a slice at $\omega_y = 0$ (c) a slice at $\omega_x = 0$.

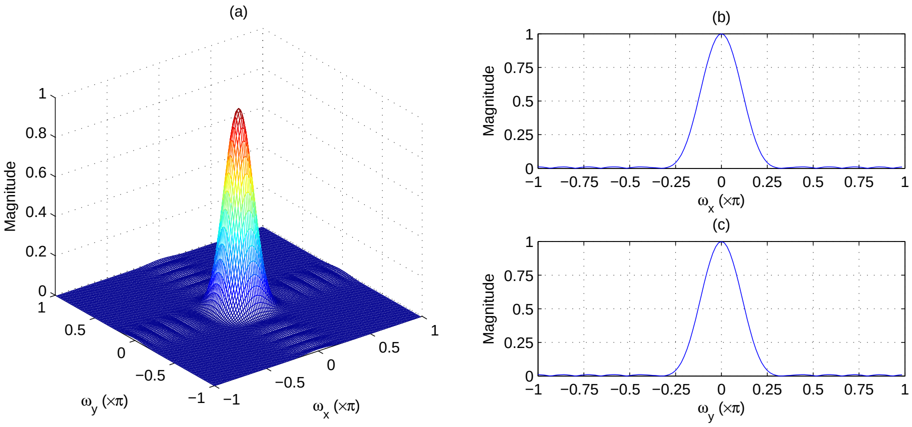

Figure 2.8: (a) Magnitude of the 2D DDFT of the 2D Hamming window $wn_{s,\text{2DHam}}(n_x, n_y)$, $(2N_x + 1) \times (2N_y + 1) = 15 \times 15$ (b) a slice at $\omega_y = 0$ (c) a slice at $\omega_x = 0$.

2.4 Analog Preprocessing and Temporal Sampling of DAA and FPA Signals

In this section, analog preprocessing and temporal sampling of DAA and FPA signals are briefly reviewed. A typical analog preprocessing system that can be employed in DAA and FPA receivers is shown in Figure 2.9. Here, in the temporal dimension, *direct sampling*, i.e., without down conversion, is employed because, for the SKA lower mid-band (0.5–1.5 GHz), it is expected that direct sampling will be more economical by the time of the construction of the SKA [68], with the ever decreasing cost of

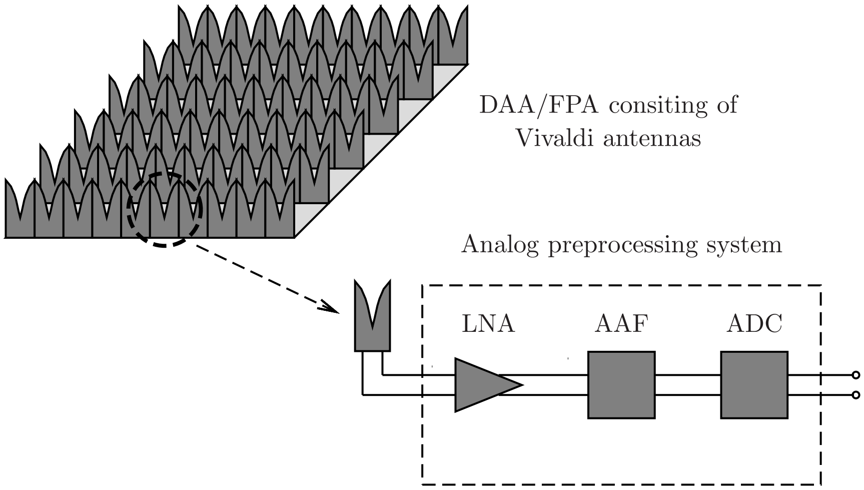

Figure 2.9: Typical analog preprocessing system that can be employed in DAA and FPA receivers.

digital signal processing and the emergence of *time-based* analog-to-digital converters (ADCs) [69][70][71][72].

First, the photonic responses from the elemental antennas are amplified by an array of LNAs. In addition to the amplified photonic responses for the SOIs and RFIs, the output signals of the LNAs contain receiver noise, which mainly consists of the thermal noise generated in the LNAs and due to the ohmic resistance in the elemental antennas [37](ch. 2). The power spectral density of the receiver noise may be assumed to be *uniform* in the 3D frequency space.

The output signals of the LNAs are then filtered with analog AAFs having lowpass frequency responses to reduce aliasing in the temporal dimension after sampling. The passband edge of the AAFs may be selected as $\max[f_{\text{soi}}]$. Note that, after filtering with AAFs, almost all of the spectra in the regions vulnerable to spatial aliasing (see Figure 2.6) are attenuated to the level of the stopband gain. The anti-alias-filtered signals are then analog-to-digital converted by an array of *synchronous* ADCs. *The temporal sampling frequency $f_{t,S}$ should be greater than or equal to twice the stopband edge of the AAFs in order to alleviate significant aliasing in the temporal dimension.* The effects of the analog preprocessing on the SOIs and, in particular, BD errors generated by perturbations and mismatches among the LNAs and AAFs are discussed in detail in Chapter 4.

2.5 Summary

Both SOIs and terrestrial RFI signals received by the DAAs may be modeled as 3D CD ST PWs. The ROS of the spectrum of a 3D CD ST PW lies on a straight line going through the origin of the 3D CD frequency space. In practice, the effective FoV of a DAA is limited to an angular range $\theta \in [0^\circ, \theta_{Dmax}]$, where θ_{Dmax} is the maximum inclination scan angle of the DAA sky beam. The terrestrial RFI signals are received by the DAAs with inclination angles $\theta > 80^\circ$. The ROSs of the spectra of the SOIs having DOAs inside the FoV of a DAA occupy a double-cone-shaped volume having a half-cone angle $\tan^{-1}(\sin(\theta_{Dmax}))$ whereas those of the terrestrial RFI signals lie on or close to the surface of a double cone having a half-cone angle 45°.

The EM field on the focal plane of a paraboloidal reflector due to dish-reflected BB SOIs can be obtained by means of the "Huygens' Principle". The FoV of a typical FPA mounted on a paraboloidal reflector is limited to a few square degrees. For such a FoV, the ROSs of the spectra of the focal fields due to the dish-reflected BB SOIs occupy a double-cone-shaped volume having a half-cone angle $\alpha_{Fmax} = \tan^{-1}(\sin(\theta_{Fmax}))$. Similar to the terrestrial RFI signals received by the DAAs, most of the terrestrial RFI signals are received by the FPAs directly with inclination angles $\theta > 75^\circ$, and they may be modeled as 3D CD ST PWs. Consequently, the ROSs of the spectra of the terrestrial RFIs lie on or close to the surface of a double cone having a half-cone angle 45°.

The elemental antennas of a DAA or an FPA spatially sample the SOIs and RFI signals. Under an ideal infinite-extent aperture, spatial aliasing in the interested temporal frequency range can be avoided by choosing sufficiently short uniform sampling distances along both spatial dimensions. In the case of real DAAs and FPAs which have finite-extent apertures, the ROSs of the MD spectra of the spatially sampled signals are spread around the ideal ROSs along planes parallel to the $\Omega_{ct} = 0$ plane. This causes to leak some energy from the passband to the stopband and vice versa. These leakages can be reduced by spatially weighting the spatially sampled signals by an appropriate 2D window at the expense of wider main lobes.

In the analog preprocessing system, the photonic responses from the elemental antennas of a DAA or an FPA are first amplified by an array of LNAs before filtering with AAFs. The anti-alias-filtered signals are then analog-to-digital converted by an array of synchronous ADCs. Aliasing in the temporal dimension can be significantly reduced by choosing a temporal frequency that is greater than or equal to twice the stopband edge of the AAFs as the temporal sampling frequency.

Chapter 3

Computationally Efficient 3D Spatio-Temporal FIR Cone and Frustum Filter Banks

3.1 Introduction

Three-dimensional ST cone filters can be employed in such fields as wireless communications, biomedical imaging, seismic imaging and directional audio systems [3][4][5][73][74]. In applications of these fields, desired ST PW SOIs are enhanced based on their DOAs while attenuating undesired signals such as other ST PWs having DOAs that differ from those of the SOIs and noise [4]. Recently, with the emergence of DAAs and FPAs, 3D ST cone and frustum filters have been proposed for radio astronomy applications as a means to improve the system sensitivity and survey speed of radio telescopes by attenuating terrestrial RFI signals and various types of noise signals [38][39][40][41][42][43][44](ch. 5).

A variety of design methods proposed for designing 3D cone filters can be found in the literature. In [5], the cone-shaped passband is approximated by cascading two 2D fan filters having wedge-shaped passbands, with different orientations, in the 3D frequency space. The same approach has been utilized in [75] using structurally passive 2D recursive fan filters. Optimization techniques have been employed in [76][77][78], and symmetries in the frequency response of a cone filter have been exploited to reduced the number of parameters to be optimized. Zervakis and Venetsanopoulos [79][80] proposed a method based on the coefficient transformation of 2D circularly symmetric filters. Furthermore, a closed form design method for recursive cone filters that are realized from passive 3D wave digital filters has been proposed in [81]. Another method based on numerical optimization has been proposed in [74]. A number of filter bank approaches that yield closed form approximations for the 3D transfer functions of cone filters have been reported in [3][53][4][73][82]. In particular, a computationally efficient DFT-polyphase filter bank structure is employed in [3][53]. Moreover, in [83] and, recently, in [84][85], cone filter design methods based on the McClellan transform have been proposed. Recently, Gunaratne and Bruton [40] proposed a non-separable FIR cone filter design method based on the well known windowing technique.

In [38](ch. 5.5)[39], a 3D ST FIR cone filter bank structure has been proposed especially for radio astronomy applications. As in [3][53][4][73], the double-cone-shaped passband is approximated by cascading a sufficient number of disc-shaped passbands having uniform height and appropriate radii. In contrast to previously reported techniques [45][46][47][48][49][50][51][52] which are mostly suitable for processing of temporally narrowband signals, the ST filtering approach with cone filters is inherently capable of processing temporally BB signals. This approach led to satisfactory results with respect to the improvement in SINR, but tends to be computationally intensive. In fact, the computational complexity is approximately proportional to the number of bands. However, *downsampling in the temporal dimension* can be exploited to significantly reduce the computational complexity without loss in the achievable improvement in SINR. In such a case, the computational complexity becomes almost independent of the number of bands.

Following [3][53], in this chapter, we propose two computationally efficient 3D cone filter bank structures to improve the computational efficiency of 3D cone filter banks. Furthermore, we extend this approach to design 3D frustum filter banks having double-frustum-shaped passbands oriented along the temporal axis. Next, it is confirmed numerically that the proposed 3D frustum filter banks provide a significant reduction of the computational complexity compared to the original filter bank without deteriorating the improvement in SINR. Early work of these improvements and extensions has been published in [42].

The organization of the chapter is as follows. In Section 3.2, a review of the 3D cone filter bank structure proposed in [38](ch. 5.5)[39] is presented. Next, computationally efficient 3D DFT-polyphase and modified DFT-polyphase cone filter bank structures are described in Sections 3.3 and 3.4, respectively. Then, a strategy that can be used to design 3D frustum filter banks from computationally efficient 3D cone filter banks without compromising the computational efficiency is described in Section 3.5. In Section 3.6, performance of the proposed filter bank structures, in terms of the achievable improvement in SINR and the computational complexity, is compared with the performance of the original filter bank structure with the aid of illustrative examples. Finally, summary of the chapter is presented in Section 3.7.

3.2 A Review of Undecimated 3D ST FIR Cone Filter Bank Structure

The 3D ST FIR cone filter bank structure proposed in [38](ch. 5.5)[39] is shown in Figure 3.1 (a). We refer to this cone filter bank as *undecimated cone filter bank* throughout this chapter. Each subband of the undecimated cone filter bank is comprised of a 1D temporal *linear-phase causal* FIR bandpass filter, $U_k(z_{ct})$, in cascade with a 2D spatial circularly symmetric *zero-phase* FIR lowpass filter, $V_k(z_x, z_y)$, where $k = 0, 1, \ldots, L-1$, $(z_x, z_y, z_{ct}) \in \mathbb{C}^3$ and $L \in \mathbb{Z}^+$ is the number of *real* bands. Here, we use the word "real" to emphasize that the transfer functions of all the 1D temporal filters have real-valued coefficients, and, hence they possess even symmetry. Further, each subband approximates a double-disc-shaped passband having an appropriate radius and a height of π/L. The double-cone-shaped passband oriented along the ω_{ct} axis is approximated by cascading those L double-disc-shaped passbands as illustrated in Figure 3.1 (b). The 3D transfer function of the undecimated cone filter bank, $CFB_{\mathrm{UD}}(z_x, z_y, z_{ct})$, is given by

$$CFB_{\mathrm{UD}}(z_x, z_y, z_{ct}) = \sum_{k=0}^{L-1} U_k(z_{ct}) V_k(z_x, z_y). \tag{3.1}$$

3.2.1 Design of 1D Temporal Bandpass Filters

The 1D temporal FIR bandpass filters are designed using the windowing technique [67] (ch. 9). The ideal frequency response $U_{\mathrm{I},k}(\mathrm{e}^{j\omega_{ct}})$ of the kth bandpass filter is given

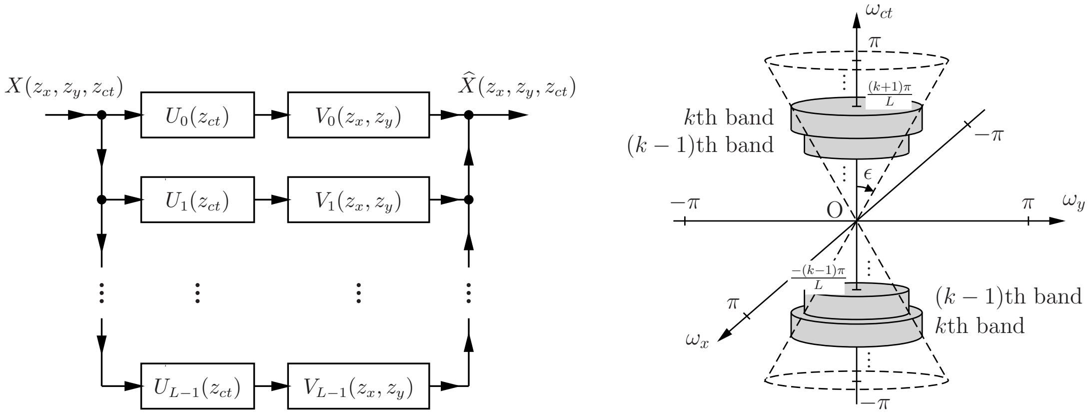

(a) (b)

Figure 3.1: (a) The 3D ST FIR cone filter bank structure proposed in [38](ch. 5.5)[39] (b) approximation of the double-cone-shaped passband oriented along the ω_{ct} axis by cascading L double-disc-shaped passbands having appropriate radii and a uniform height of π/L.

by

$$U_{\mathrm{I},k}(\mathrm{e}^{j\omega_{ct}}) = \begin{cases} 1, & \frac{k\pi}{L} \leq \omega_{ct} \leq \frac{(k+1)\pi}{L} \\ 0, & \text{otherwise.} \end{cases} \tag{3.2}$$

The ideal infinite-extent impulse response $u_{\mathrm{I},k}(n_{ct})$ of the kth 1D temporal bandpass filter is given by [67](pp. 452)

$$u_{\mathrm{I},k}(n_{ct}) = \frac{1}{n_{ct}\pi}\left[\sin\left(\frac{(k+1)\pi n_{ct}}{L}\right) - \sin\left(\frac{k\pi n_{ct}}{L}\right)\right]. \tag{3.3}$$

Finally, the finite-extent impulse response $u_k(n_{ct})$ of the kth 1D temporal *causal* bandpass filter $U_k(z_{ct})$ of order N_T is obtained as

$$u_k(n_{ct}) = u_{\mathrm{I},k}\left(n_{ct} - \frac{N_T}{2}\right) wn_{\mathrm{Ham}}\left(n_{ct} - \frac{N_T}{2}\right), \tag{3.4}$$

where $wn_{\mathrm{Ham}}(n_{ct})$ is the 1D Hamming window of length $N_T + 1$ that is given in Equation (2.19).

The amplitude responses of the 1D temporal bandpass filters are depicted in Figure 3.2. Note that, according to Equation (3.2), the lower cutoff frequency of the first ($k = 0$) bandpass filter and the upper cutoff frequency of the last ($k = L - 1$) bandpass filter are 0 rad/sample and π rad/sample, respectively. Therefore, $U_0(z_{ct})$

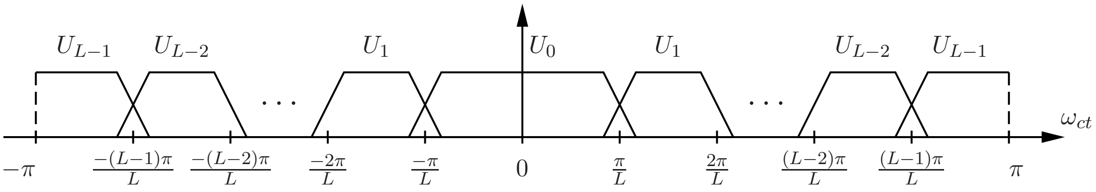

Figure 3.2: Amplitude responses of the 1D temporal bandpass filters.

and $U_{L-1}(z_{ct})$ possess the frequency responses that are similar to lowpass and highpass filters, respectively. Consequently, $U_0(z_{ct})$ can be designed as a lowpass filter, whereas $U_{L-1}(z_{ct})$ can be designed as a highpass filter.

3.2.2 Design of 2D Spatial Circularly Symmetric Lowpass Filters

The 2D spatial circularly symmetric lowpass filters are also designed using the windowing technique [1](ch. 3.3)[2](ch. 5.1.1). The ideal frequency response of the kth 2D lowpass filter, $V_{\mathrm{I},k}(\mathrm{e}^{j\omega_x}, \mathrm{e}^{j\omega_y})$, is given by

$$V_{\mathrm{I},k}(\mathrm{e}^{j\omega_x}, \mathrm{e}^{j\omega_y}) = \begin{cases} 1, & \sqrt{\omega_x^2 + \omega_y^2} \leq \omega_{sc,k} \\ 0, & \text{otherwise}, \end{cases} \tag{3.5}$$

where

$$\omega_{sc,k} = \frac{(k+1)\pi}{L} \tan \epsilon, \tag{3.6}$$

where ϵ is the half-cone angle of the double-cone-shaped passband. The 2D infinite-extent impulse response $v_{\mathrm{I},k}(n_x, n_y)$ of the circularly symmetric lowpass filter can be expressed as [2](pp. 23–24)

$$v_{\mathrm{I},k}(n_x, n_y) = \frac{\omega_{sc,k}}{2\pi\sqrt{n_x^2 + n_y^2}} J_1\left(\omega_{sc,k}\sqrt{n_x^2 + n_y^2}\right), \tag{3.7}$$

where $J_1(\cdot)$ is the first-order Bessel function of the first kind. The 2D finite-extent impulse response $v_k(n_x, n_y)$ of the spatial *zero-phase* lowpass filter $V_k(z_x, z_y)$ of order $N_{Sx} \times N_{Sy}$ is then obtained as

$$v_k(n_x, n_y) = v_{\mathrm{I},k}(n_x, n_y) wn_{\mathrm{2Ham}}(n_x, n_y), \tag{3.8}$$

where $wn_{2\text{Ham}}(n_x, n_y)$ is the 2D Hamming window that can be generated from its 1D counterpart as a *separable* window as given in Equation (2.18) (with $N_x = \frac{N_{Sx}}{2}$ and $N_y = \frac{N_{Sy}}{2}$) or as a *circular* window that is given by [86]

$$wn_{c,2\text{Ham}}(n_x, n_y) \triangleq wn_{\text{Ham}}\left(\sqrt{n_x^2 + n_y^2}\right), \qquad |n_x| \leq \frac{N_{Sx}}{2} \text{ and } |n_y| \leq \frac{N_{Sy}}{2}, \quad (3.9)$$

where $wn_{\text{Ham}}(\cdot)$ is the 1D Hamming window given in Equation (2.19).

3.3 Proposed 3D ST DFT-polyphase FIR Cone Filter Bank Structure

Here, a 3D ST cone filter bank structure is proposed in order to improve the computational complexity. The proposed 3D DFT cone filter bank structure that is based on [3][53] is illustrated in Figure 3.3. It consists of M *complex* bands[1]. In contrast to the transfer function of a 1D temporal filter corresponding to a real subband, the transfer function of a 1D temporal filter corresponding to a complex subband has complex-valued coefficients and does not possess even symmetry[2]. Each subband of the DFT cone filter bank is comprised of a 2D spatial circularly symmetric *zero-phase* FIR filter, $G_k(z_x, z_y)$, between 1D temporal *linear-phase causal* FIR analysis and synthesis filters, $H_k(z_{ct})$ and $F_k(z_{ct})$, respectively, where $k = 0, 1, \ldots, (M-1)$. In contrast to the *double*-disc-shaped passbands in the undecimated cone filter bank discussed in the previous section, each subband in the DFT cone filter bank approximates a *single*-disc-shaped passband having an appropriate radius and a height of $2\pi/M$ due to the complex nature of the subbands. Nevertheless, the double-cone-shaped passband oriented along the ω_{ct} axis is approximated by cascading the M single-disc-shaped passbands as in the undecimated counterpart. Also, note that M should be equal to $2L$ to have a similar approximation for the double-cone-shaped passband.

The subsampling matrix $\mathbf{M}$ is given by

$$\mathbf{M} = \text{diag}\left[1 \;\; 1 \;\; M/2\right], \qquad (3.10)$$

---

[1] M is assumed to be an even integer.

[2] Although the transfer functions of the 1D temporal filters in the 0 th and $\frac{M}{2}$th subbands have real-valued coefficients and possess even symmetry, we consider these two bands too as complex bands for brevity.

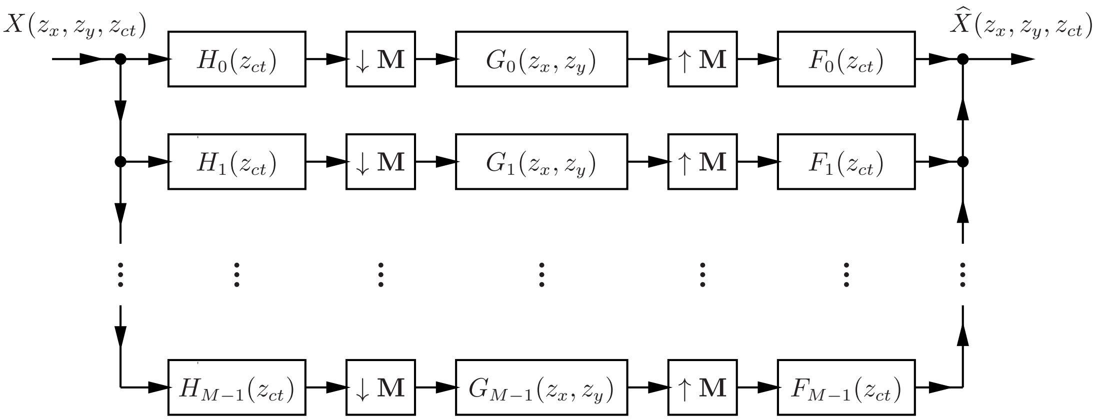

Figure 3.3: Proposed 3D DFT cone filter bank structure that is based on [3][53]. A 1D under-decimated DFT filter bank is used as the temporal filter bank.

where the term "diag" denotes a diagonal matrix. The DFT cone filter bank is therefore *temporally under decimated* (or oversampled), and, after downsampling, the number of samples in each 3D subband signal is $M/2$ times less than the number of samples in the 3D input signal. Here, under decimation means that the downsampling factor (a rational number) is between 1 and M excluding those two values.

3.3.1 Design of 1D Temporal Filter Bank

The well known DFT filter bank approach is followed to design the 1D temporal filter bank because of its well known advantages: low design and implementation complexities. In a 1D DFT filter bank, both 1D linear-phase causal analysis and synthesis filters, $H_k(z_{ct})$ and $F_k(z_{ct})$, respectively, are obtained by means of uniform complex modulation of a zero-phase 1D FIR lowpass prototype filter $P(z_{ct})$ having a cutoff frequency π/M and are given by [87]

$$H_k(z_{ct}) = F_k(z_{ct}) = z_{ct}^{-N_P/2} P(z_{ct} W_M^k), \qquad k = 0, 1, \ldots, (M-1), \tag{3.11}$$

where $W_M = \mathrm{e}^{-j2\pi/M}$ and N_P is the order of the prototype filter. In the temporal domain, the counterpart of Equation (3.11) can be expressed as

$$h_k(n_{ct}) = f_k(n_{ct}) = p\left(n_{ct} - \frac{N_P}{2}\right) W_M^{-k(n_{ct}-N_P/2)},$$
$$n_{ct} = 0, 1, \ldots, N_P, \qquad k = 0, 1, \ldots, (M-1), \tag{3.12}$$

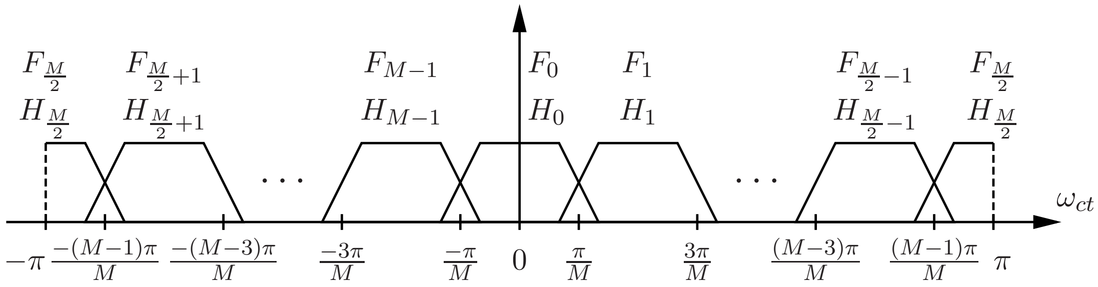

Figure 3.4: Amplitude responses of the 1D temporal analysis and synthesis filters, $H_k(z_{ct})$ and $F_k(z_{ct})$, respectively.

where $h_k(n_{ct})$, $f_k(n_{ct})$ and $p(n_{ct})$ are the impulse responses of the kth analysis filter, kth synthesis filter and the prototype filter, respectively [87]. The amplitude responses of the analysis filters $H_k(z_{ct})$ and synthesis filters $F_k(z_{ct})$ are depicted in Figure 3.4. Also, note that the amplitude response of the prototype filter $P(z_{ct})$ is the same as $H_0(z_{ct})$ and $F_0(z_{ct})$.

Design of the 1D Temporal Prototype Filter

The 1D temporal zero-phase prototype filter is derived from a zero-phase *square-root raised-cosine* FIR lowpass filter of which the *ideal* infinite-extent impulse response $p_{\mathrm{I}}(n_{ct})$ is given by [88]

$$p_{\mathrm{I}}(0) = 1 \tag{3.13a}$$

$$p_{\mathrm{I}}(n_{ct}) = \frac{\frac{4rn_{ct}}{M}\cos\left(\frac{\pi(1+r)n_{ct}}{M}\right) + \sin\left(\frac{\pi(1-r)n_{ct}}{M}\right)}{\left[1-\left(\frac{4rn_{ct}}{M}\right)^2\right]\left[\frac{4rn_{ct}}{M} + \frac{\pi(1-r)n_{ct}}{M}\right]}, \qquad n_{ct} \neq 0, \tag{3.13b}$$

where r ($0 < r \leq 1$) is the rolloff factor which determines the steepness of the transition band. For some values of M and r, $M/4r$ becomes an integer. In such cases Equation (3.13b) becomes indeterminate, and Equation (3.14) should be used instead of Equation (3.13b) to obtain $p_{\mathrm{I}}(\pm M/4r)$.

$$p_{\mathrm{I}}\left(\pm\frac{M}{4r}\right) = \frac{\pi(1+r)\sin\left(\frac{\pi(1+r)}{4r}\right) - 4r\cos\left(\frac{\pi(1+r)}{4r}\right) - \pi(1-r)\cos\left(\frac{\pi(1-r)}{4r}\right)}{8r\left[1+\frac{\pi(1-r)}{4r}\right]}. \tag{3.14}$$

The passband and stopband gains of the ideal square-root raised-cosine FIR lowpass filter are equal to unity and zero, respectively, and the passband edge, stopband edge and the cutoff frequency are, respectively, given by $(1-r)\pi/M$, $(1+r)\pi/M$ and π/M. Furthermore, the frequency response of the ideal prototype filter derived from the ideal square-root raised-cosine FIR lowpass filter is *power complementary* [88], i.e.,

$$\left|P_{\mathrm{I}}(\mathrm{e}^{j\omega_{ct}})\right|^2 + \left|P_{\mathrm{I}}(\mathrm{e}^{j(\omega_{ct}-2\pi/M)})\right|^2 = 1, \qquad 0 \leq \omega_{ct} \leq 2\pi/M. \tag{3.15}$$

However, the frequency response of a *non-ideal* prototype filter $P(z_{ct})$ of order N_P, of which the finite-extent impulse response $p(n_{ct})$ is obtained as

$$p(n_{ct}) = \sqrt{\frac{M}{2}}\, p_{\mathrm{I}}(n_{ct}) wn_{\mathrm{rec}}(n_{ct}), \tag{3.16}$$

where $wn_{\mathrm{rec}}(n_{ct})$ is the 1D rectangular window of length $N_P + 1$ which is defined as [67](ch. 9.4)

$$wn_{\mathrm{rec}}(n_{ct}) \triangleq \begin{cases} 1, & |n_{ct}| \leq \frac{N_P}{2} \\ 0, & \text{otherwise,} \end{cases} \tag{3.17}$$

is no longer power complementary and provides finite stopband attenuation. Note that, the term $\sqrt{M/2}$ is employed in Equation (3.16) to compensate the reduction of the amplitude response of the DFT cone filter bank resulting from the temporal downsampling by $M/2$. To achieve *near-perfect reconstruction*, $P(\mathrm{e}^{j\omega_{ct}})$ should closely resemble the power complementarity and should provide a sufficiently higher stopband attenuation simultaneously to minimize the amplitude distortion and the aliasing distortion, respectively. To this end, $P(\mathrm{e}^{j\omega_{ct}})$ is *optimized* with respect to r in the 2-norm sense for given N_P and M. The objective function to be minimized is defined as

$$\begin{aligned}\Phi(r, N_P, M, \omega_{ct}) \triangleq \gamma &\left(\sum_{\omega_i \in \boldsymbol{\omega}_{ct}} \left(1 - \left| \sum_{k=0}^{M-1} \left[P\left(\mathrm{e}^{j(\omega_i - 2\pi k/M)}\right)\right]^2 \right| \right)^2 \right)^{1/2} + (1-\gamma) \\ &\cdot \left(\sum_{\omega_i \in \boldsymbol{\omega}_{ct}} \sum_{l=1}^{M/2-1} \left| \sum_{k=0}^{M-1} P\left(\mathrm{e}^{j(\omega_i - 2\pi(2l+k)/M)}\right) P\left(\mathrm{e}^{j(\omega_i - 2\pi k/M)}\right) \right|^2 \right)^{1/2},\end{aligned} \tag{3.18}$$

where the elements ω_i, where $i \in \mathbb{Z}^+$, of $\boldsymbol{\omega}_{ct}$ densely cover the temporal frequency range $-\pi \leq \omega_{ct} < \pi$, and γ ($0 \leq \gamma \leq 1$) determines the weights of the two terms corresponding to the amplitude and aliasing distortions. For given N_P and M, $\Phi(r, N_P, M, \omega_{ct})$ is a 1D function, and the optimum r can be obtained using a simple line search algorithm [89](ch. 4).

3.3.2 Design of 2D Spatial Circularly Symmetric Lowpass Filters

The 2D spatial circularly symmetric lowpass filters $G_k(z_x, z_y)$ are designed using the windowing technique [1](ch. 3.3)[2](ch. 5.1.1) similar to the case of the undecimated cone filter bank. The same steps described in Subsection 3.2.2 are followed. However, the cutoff frequencies $\omega_{sc,k}$ are selected as

$$\omega_{sc,k} = \begin{cases} \frac{\pi}{M}\tan\epsilon, & k = 0 \\ \frac{2k\pi}{M}\tan\epsilon, & k = 1, 2, \ldots, (M/2) \\ \frac{2(M-k)\pi}{M}\tan\epsilon, & k = (M/2+1), (M/2+2), \ldots, (M-1), \end{cases} \tag{3.19}$$

where ϵ is the half-cone angle of the double-cone-shaped passband. According to Equation (3.19), it is clear that

$$\omega_{sc,k} = \omega_{sc,M-k}, \qquad k = 1, 2, \ldots, (M/2-1). \tag{3.20}$$

Hence,

$$g_k(n_x, n_y) = g_{M-k}(n_x, n_y), \qquad k = 1, 2, \ldots, (M/2-1), \tag{3.21}$$

and the design of M 2D spatial circularly symmetric lowpass filters is effectively reduced to the design of $M/2+1$ 2D filters. This reduction is almost a half of the original design cost.

3.3.3 Near-Perfect Reconstruction of the DFT Cone Filter Bank

Following [3][90], the 3D reconstructed (i.e., output) signal of the DFT cone filter bank shown in Figure 3.3, $\widehat{X}(z_x, z_y, z_{ct})$, can be expressed as

$$\widehat{X}(z_x, z_y, z_{ct}) = \sum_{l=0}^{M/2-1} A_l(z_x, z_y, z_{ct}) X(z_x, z_y, z_{ct} W_M^{2l}), \tag{3.22}$$

where

$$A_l(z_x, z_y, z_{ct}) = \frac{2}{M} \sum_{k=0}^{M-1} H_k(z_{ct} W_M^{2l}) G_k(z_x, z_y) F_k(z_{ct}), \qquad l = 0, 1, \ldots, (M/2-1). \tag{3.23}$$

To further analyze $\widehat{X}(z_x, z_y, z_{ct})$, Equation (3.22) is rewritten as

$$\widehat{X}(z_x, z_y, z_{ct}) = DSD_{\mathrm{DFT}}(z_x, z_y, z_{ct}) + ALS_{\mathrm{DFT}}(z_x, z_y, z_{ct}), \tag{3.24}$$

where

$$DSD_{\mathrm{DFT}}(z_x, z_y, z_{ct}) = \frac{2}{M} \sum_{k=0}^{M-1} H_k(z_{ct}) G_k(z_x, z_y) F_k(z_{ct}) X(z_x, z_y, z_{ct}) \tag{3.25}$$

is the *desired* component which is corresponding to $l = 0$ and free from aliasing distortion, and

$$ALS_{\mathrm{DFT}}(z_x, z_y, z_{ct}) = \sum_{l=1}^{M/2-1} A_l(z_x, z_y, z_{ct}) X(z_x, z_y, z_{ct} W_M^{2l}) \tag{3.26}$$

is the *undesired* aliased component having $M/2-1$ aliased terms corresponding to $l = 1, 2, \ldots, (M/2-1)$. To make the DFT cone filter bank *alias free*, $ALS_{\mathrm{DFT}}(z_x, z_y, z_{ct})$ should be zero. Since the 1D temporal analysis and synthesis filters are obtained according to Equation (3.11), $A_l(z_x, z_y, z_{ct})$ can be rewritten as

$$A_l(z_x, z_y, z_{ct}) = \frac{2\, z_{ct}^{-N_P} W_M^{-lN_P}}{M} \sum_{k=0}^{M-1} P(z_{ct} W_M^{2l+k}) G_k(z_x, z_y) P(z_{ct} W_M^{k}). \tag{3.27}$$

Furthermore, if $P(z_{ct})$ has a stopband edge that is less $2\pi/M$ and a sufficiently high stopband attenuation, then

$$P(z_{ct}W_M^{2l+k})P(z_{ct}W_M^k) \approx 0, \qquad l = 1, \ldots, (M/2-1), \quad k = 0, 1, \ldots, (M-1). \tag{3.28}$$

Note that, the stopband edge of the 1D prototype filter $P(z_{ct})$ designed in the previous subsection is always less than or equal to $2\pi/M$. It follows from Equations (3.27) and (3.28) that $A_l(z_x, z_y, z_{ct}) \approx 0$, for $l = 1, 2, \ldots, (M/2-1)$, and the DFT cone filter bank is *almost alias free*. Moreover, the higher the stopband attenuation of $P(z_{ct})$, the higher the degree of suppression of the aliased terms. In this case, the DFT cone filter bank is approximately *linear time invariant* [91](pp. 195), and the 3D transfer function $CFB_{\mathrm{DFT}}(z_x, z_y, z_{ct})$ can be expressed as

$$\begin{aligned} CFB_{\mathrm{DFT}}(z_x, z_y, z_{ct}) &\approx \frac{2}{M}\sum_{k=0}^{M-1} H_k(z_{ct})G_k(z_x, z_y)F_k(z_{ct}) \\ &\approx \frac{2\, z_{ct}^{-N_P}}{M}\sum_{k=0}^{M-1}\left[P(z_{ct}W_M^k)\right]^2 G_k(z_x, z_y). \end{aligned} \tag{3.29}$$

Since $P(z_{ct})$ is approximately power complementary and is designed to have a passband gain of $\sqrt{M/2}$ (see Equation (3.16)), $|CFB_{\mathrm{DFT}}(\mathrm{e}^{j\omega_x}, \mathrm{e}^{j\omega_y}, \mathrm{e}^{j\omega_{ct}})|$ is approximately unity inside the double-cone-shaped passband implying *near-perfect reconstruction* of the DFT cone filter bank. Furthermore, it follows from Equation (3.29) that the overall temporal delay of the DFT cone filter bank is N_P samples.

3.3.4 Efficient Implementation of the DFT Cone Filter Bank

As shown in [90][91](ch. 4.3.2)[92], by employing *polyphase decompositions*, 1D DFT filter banks can be implemented very efficiently. To demonstrate this , we first express $H_0(z_{ct})$ and $F_0(z_{ct})$ in terms of type-1 [91](ch. 4.3)[93](ch. 3.3.2) and type-3 [93](ch.

3.3.3) polyphase representations, respectively, as

$$H_0(z_{ct}) = \sum_{m=0}^{M-1} z_{ct}^{-m} E_m(z_{ct}^M) \tag{3.30a}$$

$$F_0(z_{ct}) = \sum_{m=0}^{M-1} z_{ct}^{m} R_m(z_{ct}^M), \tag{3.30b}$$

where $E_m(z_{ct})$ is the mth type-1 polyphase component of $H_0(z_{ct})$, and $R_m(z_{ct})$ is the mth type-3 polyphase component of $F_0(z_{ct})$. In the temporal domain, $e_m(n_{ct})$ and $r_m(n_{ct})$ are related to $h_0(n_{ct})$ and $f_0(n_{ct})$, respectively, as

$$e_m(n_{ct}) = h_0(Mn_{ct} + m), \qquad m = 0, 1, \ldots, M-1 \tag{3.31a}$$

$$r_m(n_{ct}) = f_0(Mn_{ct} - m), \qquad m = 0, 1, \ldots, M-1. \tag{3.31b}$$

Then, the transfer function of the kth analysis filter $H_k(z_{ct})$ can be expressed as

$$H_k(z_{ct}) = W_M^{kN_P/2} \sum_{m=0}^{M-1} W_M^{-km} z_{ct}^{-m} E_m(z_{ct}^M), \tag{3.32}$$

and the vector $\mathbf{h}(z_{ct}) = [H_0(z_{ct}) \;\; H_1(z_{ct}) \;\; \cdots \;\; H_{M-1}(z_{ct})]^{\mathrm{T}}$ can be expressed in the matrix form as

$$\mathbf{h}(z_{ct}) = \mathbf{A}\mathbf{W}^{*}\mathbf{E}(z_{ct}^M)\mathbf{e}(z_{ct}), \tag{3.33}$$

where

$$\mathbf{A} = \operatorname{diag}\left[1 \;\; W_M^{N_P/2} \;\; \cdots \;\; W_M^{N_P(M-1)/2}\right] \tag{3.34a}$$

$$\mathbf{W} = \begin{pmatrix} 1 & 1 & \cdots & 1 \\ 1 & W_M^1 & \cdots & W_M^{(M-1)} \\ \vdots & \vdots & \ddots & \vdots \\ 1 & W_M^{(M-1)} & \cdots & W_M^{(M-1)(M-1)} \end{pmatrix} \tag{3.34b}$$

$$\mathbf{E}(z_{ct}^M) = \operatorname{diag}\left[E_0(z_{ct}^M) \;\; E_1(z_{ct}^M) \;\; \cdots \;\; E_{M-1}(z_{ct}^M)\right] \tag{3.34c}$$

$$\mathbf{e}(z_{ct}) = \left[1 \;\; z_{ct}^{-1} \;\; \cdots \;\; z_{ct}^{-(M-1)}\right]^{\mathrm{T}}, \tag{3.34d}$$

and $(\cdot)^*$ denotes the conjugate of a matrix [90]. Note that, $\mathbf{W}$ is the $M \times M$ 1D DFT matrix. Furthermore, it is worth to note that $W_M^{kN_P/2}$ term in the right hand side of Equation (3.32) (hence, the matrix $\mathbf{A}$ in the right hand side of Equation (3.33)) is resulting from the delay introduced to make the kth analysis filter causal (see Equation (3.12)). Similarly, the transfer function of the kth synthesis filter $F_k(z_{ct})$ is written as

$$F_k(z_{ct}) = W_M^{kN_P/2} \sum_{m=0}^{M-1} W_M^{km} z_{ct}^m R_m(z_{ct}^M), \tag{3.35}$$

and the counterpart of Equation (3.33) is given by

$$\mathbf{f}(z_{ct}) = \mathbf{AWR}(z_{ct}^M)\mathbf{r}(z_{ct}), \tag{3.36}$$

where

$$\mathbf{f}(z_{ct}) = [F_0(z_{ct}) \;\; F_1(z_{ct}) \;\; \cdots \;\; F_{M-1}(z_{ct})]^{\mathrm{T}} \tag{3.37a}$$

$$\mathbf{R}(z_{ct}^M) = \operatorname{diag}\left[R_0(z_{ct}^M) \;\; R_1(z_{ct}^M) \;\; \cdots \;\; R_{M-1}(z_{ct}^M)\right] \tag{3.37b}$$

$$\mathbf{r}(z_{ct}) = \left[1 \;\; z_{ct}^1 \;\; \cdots \;\; z_{ct}^{(M-1)}\right]^{\mathrm{T}} \tag{3.37c}$$

[90]. Therefore, the implementation cost of the analysis (or synthesis) filter bank of the 1D DFT filter bank is given by the summation of the implementation costs of the prototype filter[3], 1D inverse DFT (IDFT) (or 1D DFT) matrix and the multiplications corresponding to the $W_M^{kN_P/2}$, $k = 0, 1, \ldots, (M-1)$, terms [90]. Furthermore, the implementation costs of the analysis and synthesis filter banks can be further reduced by employing 1D fast Fourier transform (FFT) algorithms to implement the 1D IDFT and DFT matrices, respectively [91](pp. 126)[92].

The efficient realization of the 3D DFT cone filter bank is illustrated in Figure 3.5. Here, the computationally efficient 1D DFT-polyphase realization described above is used to realize the 1D temporal DFT filter bank. Furthermore, $E_k(z_{ct}^M)$, $k = 0, 1, \ldots, (M-1)$, and the downsamplers and $R_k(z_{ct}^M)$, $k = 0, 1, \ldots, (M-1)$, and the upsamplers are interchanged by exploiting the first and second noble identities of 1D multirate systems [91](pp. 119–120), respectively (see Figure 3.3 for the original

---

[3] Note that, the implementation cost of $H_0(z_{ct})$ or $F_0(z_{ct})$ is the same as that of the prototype filter $P(z_{ct})$.

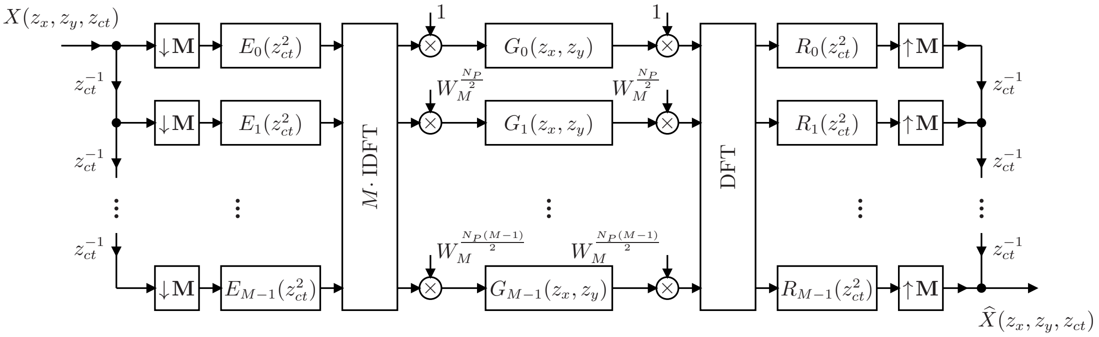

Figure 3.5: Efficient realization of the 3D DFT cone filter bank. Polyphase decompositions are employed to realize the 1D temporal DFT filter bank.

structure). *Consequently, both temporal and spatial filtering operations are carried out after the temporal downsampling and before the temporal upsampling. Hence, compared to the undecimated counterpart, a significant reduction of the computational complexity is achieved in the DFT cone filter bank despite an additional temporal filter bank. Moreover, in general, both temporal and spatial filtering operations can be performed at a $M/2$ times lower rate compared to the undecimated cone filter bank.*

3.4 Proposed 3D ST Modified DFT-Polyphase FIR Cone Filter Bank Structure

Although the DFT cone filter bank proposed in Section 3.3 provides significantly low computational complexity compared to the undecimated cone filter bank, about half of the computations are still redundant because of the *under decimation* in the temporal dimension. Furthermore, perfect reconstruction can not be achieved in the 1D DFT temporal filter bank itself. To overcome these disadvantages, the 1D DFT filter bank in Figure 3.3 is replaced with a 1D modified DFT filter bank which provides both maximal decimation in the temporal dimension and perfect reconstruction. A review of the 1D modified DFT filter banks is presented in the next subsection.

3.4.1 1D Modified DFT Filter Banks with Perfect Reconstruction: A Review

Among the different classes of M-channel maximally decimated filter banks, modulated filter banks, such as cosine modulated and modified DFT, have been widely used in many applications because of their low design and implementation complexities. Here, maximally decimation means that the downsampling factor is equal to the number of bands (channels) M or, in other words, maximum possible decimation is achieved. In modulated filter banks, both analysis and synthesis filters are generated by simply applying an appropriate modulation scheme to one or two prototype filters, hence, the design of the filter bank is effectively reduced to the design of the prototype filter(s) [94]. Furthermore, they can be implemented efficiently using fast algorithms [91](pp. 353)[95].

In comparison to the cosine modulated filter banks, the modified DFT filter banks offer the following advantages. First, an M-channel modified DFT filter bank has half of the propagation delay of an M-channel cosine modulated filter bank because the length of the prototype filter of the former is approximately half of that of the latter for a similar stopband attenuation [87]. This feature makes the modified DFT filter banks very useful in real-time applications. Second, the analysis and synthesis filters of the modified DFT filter banks are linear phase when the prototype filter is linear phase while this is not always true for the cosine modulated filter banks, although the overall filter bank is linear phase for both cases [87][94]. The linear-phase property of the analysis and synthesis filters is important in image processing applications, but for 3D cone filters, it is sufficient to have linear phase for the overall filter bank. Furthermore, modified DFT filter banks are particularly suitable for processing of *complex-valued* signals [87]. In the case of real-valued signals, a *pseudo* complex-valued signal can be generated using two real-valued signals each of which can be processed independently [87]. Therefore, it is very attractive in the design of filter banks to process radio astronomical signals, where *pseudo* complex-valued signals may be generated through the real-valued signals corresponding to orthogonal polarizations.

Structure-Inherent Odd Alias Spectra Cancellation

The basic structure of a 1D modified DFT filter bank[4] [87][95][96] is shown in Figure 3.6. Similar to the 1D DFT filter banks discussed in Subsection 3.3.1, both 1D *linear-phase causal* analysis and synthesis filters, $H_k(z_{ct})$ and $F_k(z_{ct})$, respectively, are obtained by means of uniform complex modulation of a zero-phase 1D FIR lowpass

---

[4] There are two types: type-1 and type-2, of modified DFT filter bank structures [96]. In the proposed 3D modified DFT cone filter bank structure, we employ the type-1 structure shown in Figure 3.6.

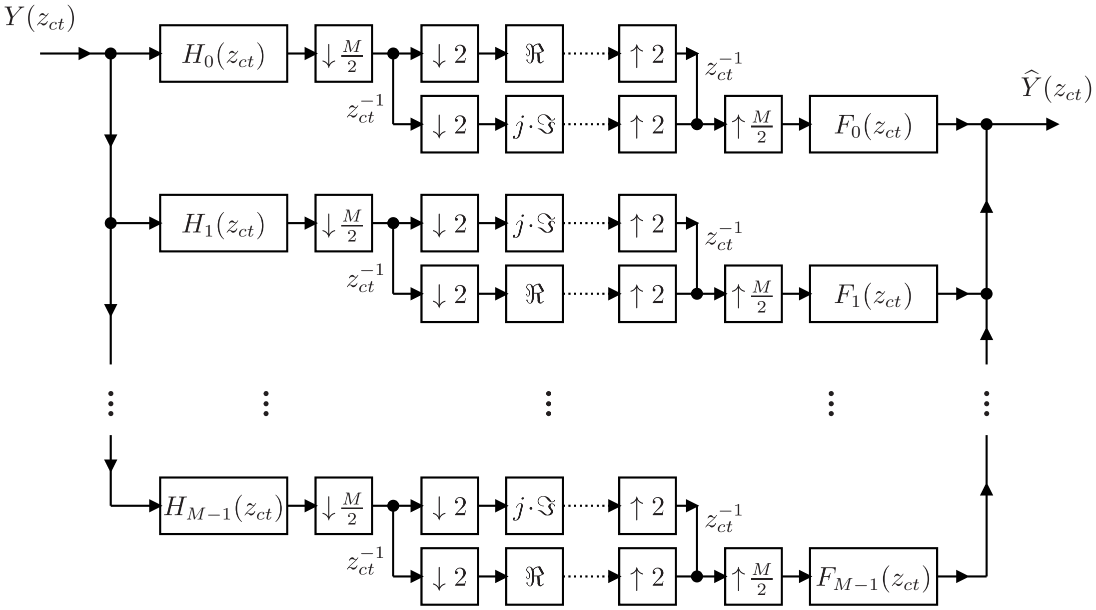

Figure 3.6: Structure of a 1D M-channel type-1 modified DFT filter bank.

prototype filter $P(z_{ct})$ having a cutoff frequency π/M as given in Equation (3.11) [87].

The main distinction of the modified DFT filter banks compared to the DFT filter banks is the way signals are decimated and interpolated [95]. As illustrated in Figure 3.6, both decimation and interpolation are carried out in two steps. In the decimation, the subband signals are first downsampled by $M/2$ (M is an even integer), following another downsampling by 2 with and without a unit delay. In fact, the second step of downsampling decomposes each subband signal into two polyphase components. Note that, after decimation, there are $2M$ polyphase components, and either the real or the imaginary part of each polyphase component is used. (Also, note that the polyphase component of which the real (imaginary) part is taken alternates from one subband to the next.) Therefore, maximal decimation is achieved for a complex-valued signal [87][95][96]. In the interpolation, the two polyphase components of each subband signal are upsampled by 2 before mixing with and without a unit delay to reconstruct the subband signal. In the second step, each subband signal is upsampled by $M/2$.

The reconstructed signal of the modified DFT filter bank $\widehat{Y}(z_{ct})$ is given by [87]

$$\widehat{Y}(z_{ct}) = \frac{z_{ct}^{-M/2}}{M} \sum_{k=0}^{M-1} \sum_{l=0}^{M/2-1} H_k(z_{ct}W_M^{2l})F_k(z_{ct})Y(z_{ct}W_M^{2l}). \tag{3.38}$$

It follows from Equation (3.38) that *all the odd alias spectra vanish, and only the even alias spectra exist.* This property only depends on the structure of the modified DFT filter bank and is independent of the prototype filter design [87].

Perfect Reconstruction in Modified DFT Filter Banks

A filter bank is said to have the perfect reconstruction property if it satisfies the following conditions:

- All alias spectra vanish
- Overall phase response is linear
- Overall amplitude response is allpass.

These conditions ensure that the overall transfer function of a filter bank is free from aliasing, phase and amplitude distortions, respectively, and is equivalent to a pure delay.

The type-1 polyphase decomposition of $H_0(z_{ct})$ and the type-3 polyphase decomposition of $F_0(z_{ct})$, given in Equations (3.30a) and (3.30b), respectively, are employed to discuss perfect reconstruction in modified DFT filter banks. Furthermore, the length of the prototype filter $(N_P + 1)$ is expressed as $(N_P + 1) = aM + b$, where $a \in \mathbb{N}$ and $b \in \{\mathbb{Z} \cup [0, M)\}$. Then, the set of conditions for perfect reconstruction, in terms of the polyphase components, can be expressed as [87][97]

$$E_m(z_{ct})\bar{R}_m(z_{ct}) + E_{m+M/2}(z_{ct})\bar{R}_{m+M/2}(z_{ct}) = \frac{2}{M}, \qquad k = 0, 1, \ldots, M/2 - 1, \quad (3.39)$$

where

$$\bar{R}_m(z_{ct}) = \begin{cases} z_{ct}^{a+1} R_{M-b+1+m}(z_{ct}), & m \leq (b-2) \\ z_{ct}^{a} R_{-b+1+m}(z_{ct}), & (b-1) \leq m < M. \end{cases} \quad (3.40)$$

The conditions given in Equation (3.39) and those for perfect reconstruction in cosine modulated filter banks given in [98][99][100] are equivalent, and, therefore, a prototype filter designed for an $M/2$-channel cosine modulated filter bank can be employed to an M-channel modified DFT filter bank by simply scaling the impulse response by $\sqrt{2}$ [87][97].

Efficient Realization of Modified DFT Filter Banks

An M-channel modified DFT filter bank can be implemented efficiently by means of two *M-channel maximally decimated* DFT-polyphase filter banks [95]. In contrast to the two step downsampling and upsampling employed in the original filter bank structure (see Figure 3.6), in the efficient implementation, illustrated in Figure 3.7, both downsampling and upsampling are carried out in one step in each of the DFT filter banks. In addition, the input signal of the second DFT filter bank is delayed by $M/2$ samples with respect to the input signal of the first DFT filter bank which is the original signal $y(n_{ct})$. Here, the terms *first* and *second* denote the *upper* and *lower* DFT filter banks in Figure 3.7, respectively. However, the pattern of taking either the real or the imaginary part from each of the $2M$ polyphase components is unchanged. In the synthesis side, the output signal of the first DFT filter bank is delayed by $M/2$ samples with respect to the output signal of the second DFT filter bank before adding them to form the output signal $\hat{y}(n_{ct})$. The implementation cost of the modified DFT filter bank is approximately twice the implementation cost of the DFT-polyphase filter bank [87].

3.4.2 Design of the Modified DFT Cone Filter Bank

The proposed 3D modified DFT cone filter bank structure is illustrated in Figure 3.8. Similar to the DFT cone filter bank proposed in the previous section, the modified DFT cone filter bank has M complex bands, each of which approximates a *single*-disc-shaped passband having an appropriate radius and a height of $2\pi/M$. However, in contrast to the DFT cone filter bank, each subband of the modified DFT cone filter bank is comprised of *two* 2D spatial filters having the same transfer function between the temporal analysis and synthesis filters.

The subsampling matrices $\mathbf{M_1}$ and $\mathbf{M_2}$ are given by

$$\mathbf{M_1} = \mathrm{diag}\,[1 \;\; 1 \;\; M/2] \tag{3.41a}$$

$$\mathbf{M_2} = \mathrm{diag}\,[1 \;\; 1 \;\; 2]\,, \tag{3.41b}$$

respectively. Consequently, the modified DFT cone filter provides *maximal decimation* in the temporal dimension for a complex-valued signal, and, therefore, the number of samples in each 3D subband signal after decimation is M times less than the number of samples in the 3D input signal.

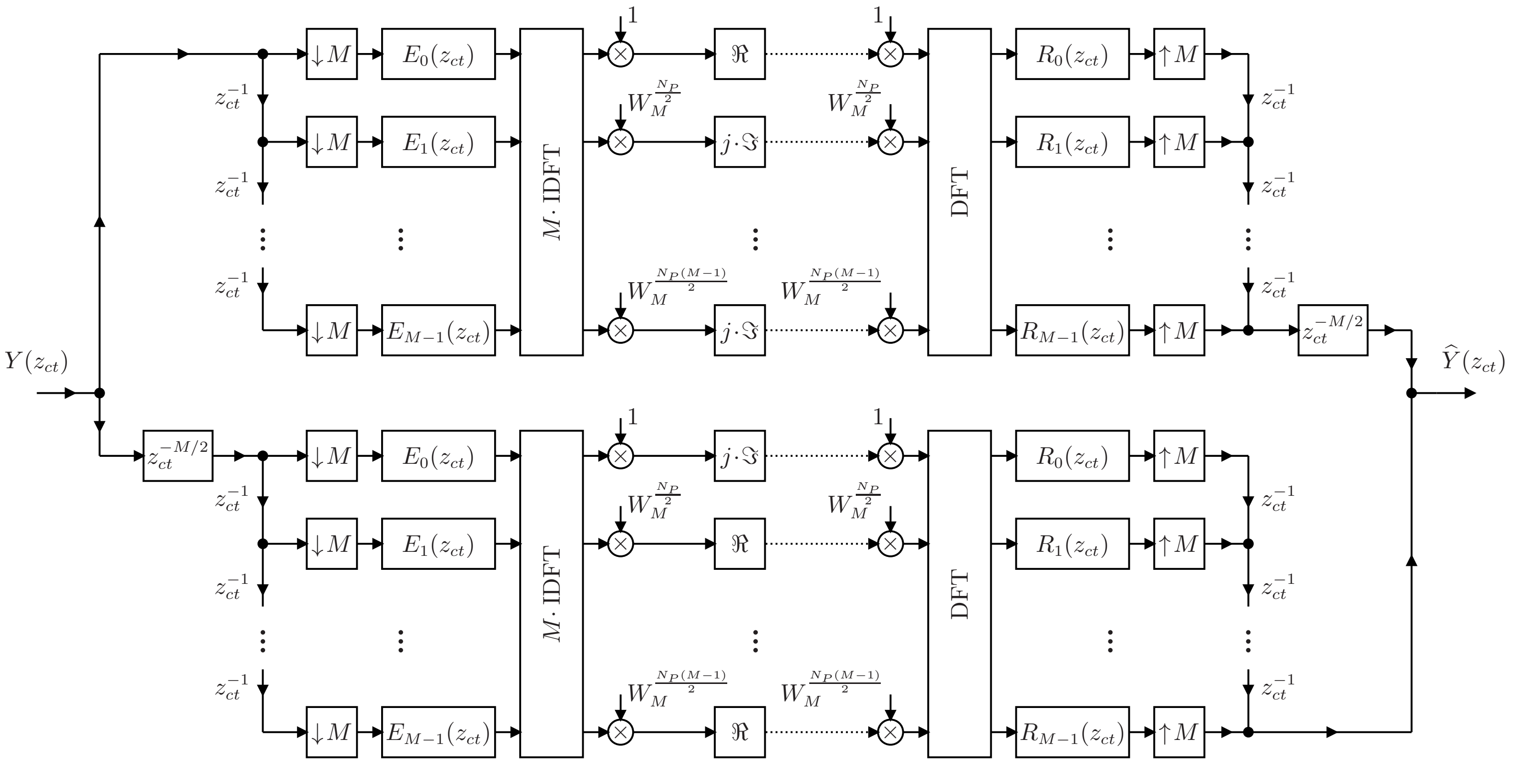

Figure 3.7: Efficient Realization of the 1D M-channel modified DFT filter bank shown in Figure 3.6.

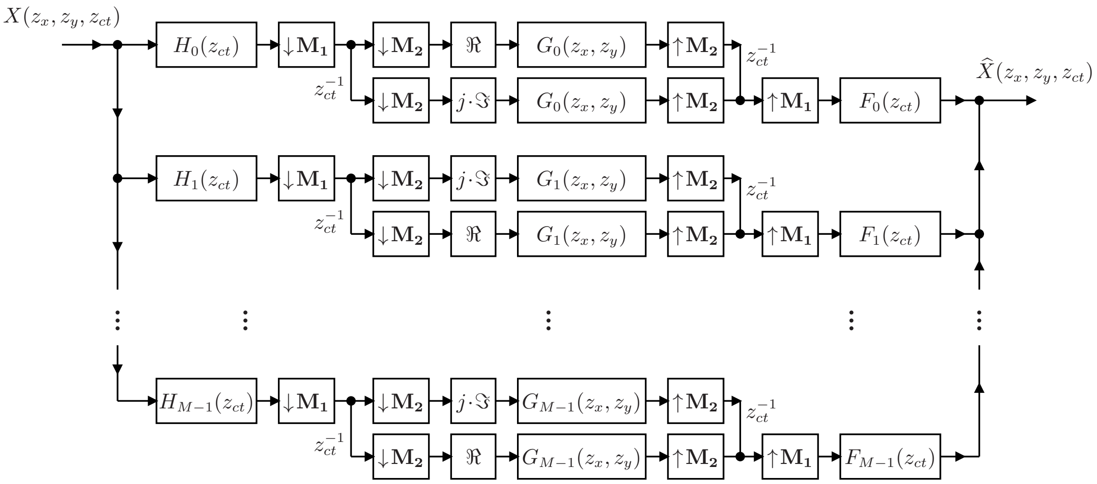

Figure 3.8: Proposed 3D ST FIR cone filter bank structure. A 1D modified DFT filter bank is used as the temporal filter bank.

The design of the 1D modified DFT filter bank is effectively limited to the design of the prototype filter. To ensure perfect reconstruction, the prototype filter should satisfy the set of conditions given in Equation (3.39), and, in general, the design has to be done through *nonlinear optimization techniques* [87]. Due to the fact that prototype filters designed for an $M/2$-channel cosine modulated filter bank can be employed to an M-channel modified DFT filter bank by simply scaling the impulse response by $\sqrt{2}$ [87][97], design methods proposed for prototypes of cosine modulated filter banks, such as those found in [98][101][102], can be used to design prototypes for modified DFT filter banks. In addition, for the special case $N_P = 2M - 1$, where N_P is the order of the prototype filter, the closed form expression derived as the *extended lapped transform* [103] can be exploited to design prototypes for the modified DFT filter banks [87]. In this case, the impulse response of the prototype filter $p(n_{ct})$ is given by

$$p(n_{ct}) = \frac{-1}{2\sqrt{M}} + \frac{1}{\sqrt{2M}} \cos\left(\frac{\pi}{2M}(2n_{ct} + 2M)\right),$$
$$n_{ct} = -M + 0.5, -M + 1.5, \ldots, M - 0.5 \qquad (3.42)$$

[87]. Note that, the amplitude response of the prototype filter $|P(\mathrm{e}^{j\omega_{ct}})|$ approximates $\sqrt{M}$ instead of unity in the passband to compensate the reduction of the amplitude response of the modified DFT cone filter bank resulting from the downsampling in the temporal dimension.

The windowing technique [1](ch. 3.3)[2](ch. 5.1.1) is employed to design the 2D spatial circularly symmetric lowpass filters $G_k(z_x, z_y)$. The same steps described in Subsection 3.3.2 are followed, and the same cutoff frequencies $\omega_{sc,k}$ selected for the DFT cone filter bank, given in Equation (3.19), are used in the design.

3.4.3 Near-Perfect Reconstruction of the Modified DFT Cone Filter Bank

Following [3][87], the 3D reconstructed signal of the modified DFT cone filter bank shown in Figure 3.8, $\widehat{X}(z_x, z_y, z_{ct})$, can be expressed as

$$\widehat{X}(z_x, z_y, z_{ct}) = z_{ct}^{-M/2} \sum_{l=0}^{M/2-1} A_l(z_x, z_y, z_{ct}) X(z_x, z_y, z_{ct} W_M^{2l}), \tag{3.43}$$

where

$$A_l(z_x, z_y, z_{ct}) = \frac{1}{M} \sum_{k=0}^{M-1} H_k(z_{ct} W_M^{2l}) G_k(z_x, z_y) F_k(z_{ct}), \qquad l = 0, 1, \ldots, (M/2 - 1). \tag{3.44}$$

To further analyze $\widehat{X}(z_x, z_y, z_{ct})$, Equation (3.43) is rewritten as

$$\widehat{X}(z_x, z_y, z_{ct}) = DSD_{\text{MoDFT}}(z_x, z_y, z_{ct}) + ALS_{\text{MoDFT}}(z_x, z_y, z_{ct}), \tag{3.45}$$

where

$$DSD_{\text{MoDFT}}(z_x, z_y, z_{ct}) = \frac{z_{ct}^{-M/2}}{M} \sum_{k=0}^{M-1} H_k(z_{ct}) G_k(z_x, z_y) F_k(z_{ct}) X(z_x, z_y, z_{ct}) \tag{3.46}$$

is the *desired* component which is corresponding to $l = 0$ and free from aliasing distortion, and

$$ALS_{\text{MoDFT}}(z_x, z_y, z_{ct}) = z_{ct}^{-M/2} \sum_{l=1}^{M/2-1} A_l(z_x, z_y, z_{ct}) X(z_x, z_y, z_{ct} W_M^{2l}) \tag{3.47}$$

is the *undesired* aliased component having $M/2 - 1$ aliased terms corresponding to $l = 1, 2, \ldots, (M/2 - 1)$.

Since the temporal modified DFT filter bank provides perfect reconstruction, if the impulse responses of the 2D spatial filters are scaled appropriately so that

$$G_k(\mathrm{e}^{j\omega_x}, \mathrm{e}^{j\omega_y})|_{\omega_x=\omega_y=0} = 1, \qquad k = 0, 1, \ldots, (M-1), \tag{3.48}$$

the modified DFT cone filter bank provides *perfect reconstruction* along the ω_{ct} axis. However, in general, it provides near-perfect reconstruction in other regions of the double-cone-shaped passband. That is, the modified DFT cone filter bank is *almost alias free*, and the amplitude response is approximately *unity* inside the double-cone-shaped passband. To confirm this, we can employ the same argument used in Section 3.3.3 for the DFT cone filter bank because the reconstructed signals of both filter banks, given in Equations (3.22) and (3.43), only differ in a scaling factor and an additional temporal delay. Note that, the higher the stopband attenuation of the prototype filter, the higher the degree of suppression of the aliased terms. With near-perfect reconstruction, the modified DFT cone filter bank is approximately *linear time invariant* [91](pp. 195), and the 3D transfer function $CFB_{\mathrm{MoDFT}}(z_x, z_y, z_{ct})$ can be expressed as

$$\begin{aligned} CFB_{\mathrm{MoDFT}}(z_x, z_y, z_{ct}) &\approx \frac{z_{ct}^{-M/2}}{M} \sum_{k=0}^{M-1} H_k(z_{ct}) G_k(z_x, z_y) F_k(z_{ct}) \\ &\approx \frac{z_{ct}^{-(N_P+M/2)}}{M} \sum_{k=0}^{M-1} \left[P(z_{ct} W_M^k)\right]^2 G_k(z_x, z_y), \end{aligned} \tag{3.49}$$

where $P(z_{ct})$ is the prototype filter. Furthermore, it follows from Equation (3.49) that the overall temporal delay of the modified DFT cone filter bank is $N_P + M/2$ samples.

3.4.4 Efficient Implementation of the Modified DFT Cone Filter Bank

The efficient realization of the 3D modified DFT cone filter bank is depicted in Figure 3.9. Here, the 1D modified DFT filter bank is realized by two 1D DFT-polyphase filter banks as described in Subsection 3.4.1, and the subsampling matrix $\mathbf{M}$ is given

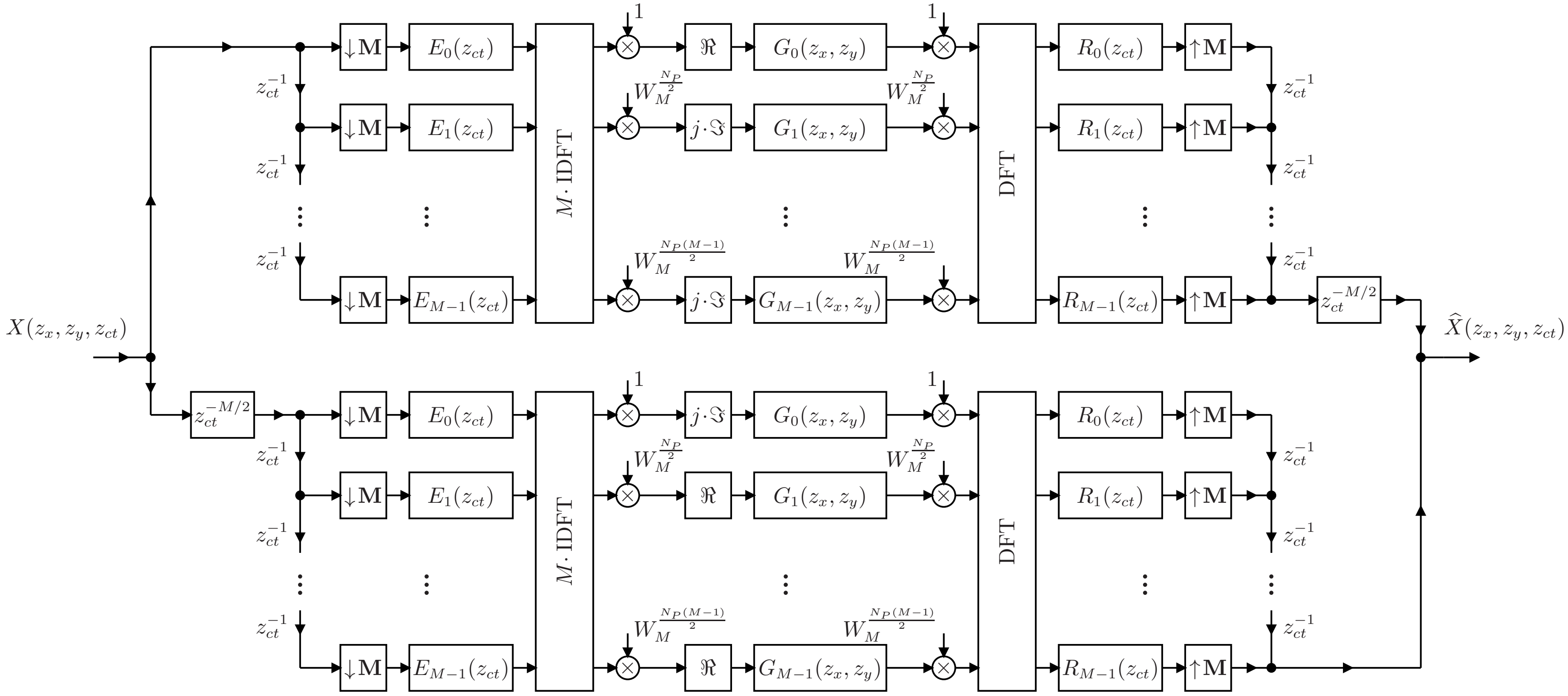

Figure 3.9: Efficient realization of the 3D ST modified DFT-polyphase FIR cone filter bank.

by

$$\mathbf{M} = \operatorname{diag}\left[1 \quad 1 \quad M\right]. \tag{3.50}$$

As in the DFT cone filter bank, both temporal and spatial filtering operations are carried out after the temporal downsampling and before the temporal upsampling. *Therefore, in general, both temporal and spatial filtering operations can be performed at a M times lower rate compared to the undecimated cone filter bank and at a half of the rate of the DFT cone filter bank. Furthermore, note that the number of samples processed by the $2M$ 2D spatial filters in the modified DFT cone filter bank is almost and exactly half of those processed by the M 2D spatial filters in the DFT cone filter bank for a real-valued and a complex-valued signal, respectively. Consequently, the computational complexity of the modified DFT cone filter bank is approximately M times and two times less than those of the undecimated and DFT cone filter banks, respectively. However, more than twice the hardware required for the DFT cone filter bank implementation has to be used to implement the modified DFT cone filter bank.*

3.5 3D ST DFT- and Modified DFT-Polyphase FIR Frustum Filter Bank Structures

In this section, we extend the proposed two 3D cone filter bank structures to 3D *frustum* filter bank structures. As the double-cone-shaped passband, the double-frustum-shaped passband is oriented along the ω_{ct} axis as illustrated in Figure 3.10. *Because the double-cone-shaped passband is approximated by means of disc-shaped passbands having appropriate radii and a uniform height of $2\pi/M$, a double-frustum-shaped passband can be approximated by employing an appropriate subset of bands.* Then, the 3D transfer functions of the DFT and modified DFT frustum filter banks can be expressed, respectively, as

$$FFB_{\mathrm{DFT}}(z_x, z_y, z_{ct}) \approx \frac{2}{M} \sum_{k \in \mathcal{F}} H_k(z_{ct}) G_k(z_x, z_y) F_k(z_{ct}) \tag{3.51}$$

$$FFB_{\mathrm{MoDFT}}(z_x, z_y, z_{ct}) \approx \frac{z_{ct}^{-M/2}}{M} \sum_{k \in \mathcal{F}} H_k(z_{ct}) G_k(z_x, z_y) F_k(z_{ct}), \tag{3.52}$$

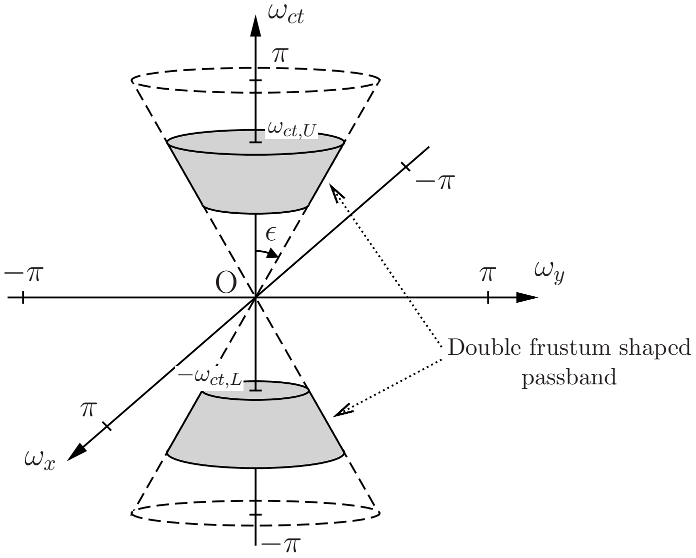

Figure 3.10: Double-frustum-shaped passband oriented along the ω_{ct} axis. The lower and upper temporal cutoff frequencies are denoted by $\omega_{ct,L}$ and $\omega_{ct,U}$, respectively.

where $\mathcal{F}$ is the set that contains the indices of the bands required to approximate the double-frustum-shaped passband. Furthermore, it is worthwhile to note that, for a particular design, the lower and upper temporal cutoff frequencies of the approximated double-frustum-shaped passband may be different from the specified ones because, in general, the lower cutoff frequency of the first temporal subband filter and the upper cutoff frequency of the last temporal subband filter used to approximate each frustum-shaped passband may not coincide with the specified lower and upper temporal cutoff frequencies, respectively. Nevertheless, by properly selecting the number of bands M in the cone filter, the error between the approximated and specified temporal cutoff frequencies can be minimized.

One major drawback that arises when all the bands are not employed in the approximation of the double-frustum-shaped passband is that the computationally efficient filter bank structures illustrated in Figures 3.5 and 3.9 can not be used since all the subband signals are necessary to perform the 1D IDFT and DFT in the implementations of analysis and synthesis temporal filters, respectively. To overcome this drawback, we propose the following procedure:

- Implement all the 1D analysis filters $H_k(z_{ct})$, $k = 0, 1, \ldots, (M-1)$, as in the cone filter banks.

- Implement only the 2D spatial filters necessary for the frustum filter bank, i.e.,

$G_k(z_x, z_y)$, $k \in \mathcal{F}$. The output signals of the 1D analysis filters corresponding to the bands that are not used in the frustum filter bank, i.e., $x_{\mathrm{IDFT},k}(n_x, n_y, n_{ct})$, $k \notin \mathcal{F}$, where $x_{\mathrm{IDFT},k}(n_x, n_y, n_{ct})$ is the output signal of the IDFT block(s) that is corresponding to the kth band, are discarded.

- Implement all the 1D synthesis filters $F_k(z_{ct})$, $k = 0, 1, \ldots, (M-1)$, as in the cone filter banks. Zeros are inserted as the input signals of the 1D synthesis filters corresponding to the bands that are not used in the frustum filter bank, i.e., $x_{\mathrm{DFT},k}(n_x, n_y, n_{ct}) = 0$, $k \notin \mathcal{F}$, where $x_{\mathrm{DFT},k}(n_x, n_y, n_{ct})$ is the input signal of the DFT block(s) that is corresponding to the kth band.

Note that, although both 1D analysis and synthesis filters are implemented for all the bands, the 3D transfer functions corresponding to the overall implementations are exactly the same as those given in Equations (3.51) and (3.52).

3.6 A Numerical Study of Performance of 3D ST FIR Frustum Filter Banks

In this section, a numerical study of the performance of the proposed DFT and modified DFT frustum filter banks is presented. First, a DFT and a modified DFT frustum filter bank satisfying given frequency specifications are designed, and characteristics of their frequency responses, such as passband ripple, stopband attenuation and aliasing distortion, are examined. Next, the improvement in SINR that can be achieved with the proposed frustum filter banks is compared to that obtained with the undecimated filter bank for both DAAs and FPAs. Finally, an analysis of the computational complexity of the three frustum filter banks is presented for both 3D real-valued and complex-valued signals.

3.6.1 Design of 3D ST Frustum Filter Banks: An Example

Here, we consider a design example for the 3D DFT and modified DFT frustum filter banks. The design specifications of the frustum filter banks are given in Table 3.1. The temporal passband of the frustum filter banks, i.e., 0.5–1.5 GHz, is selected such that it covers the so-called *SKA lower mid-band.* In the 3D discrete frequency domain, the lower and upper temporal cutoff frequencies ($\omega_{ct,L}$ and $\omega_{ct,U}$) can be, respectively, calculated as 0.25π rad/sample and 0.75π rad/sample. The order and *total* number

Design specification	Value
Maximum Passband Ripple, A_p	0.2 dB
Minimum Stopband Attenuation, A_a	50 dB
Temporal lower cutoff frequency, $f_{t,L}$	0.5 GHz
Temporal upper cutoff frequency, $f_{t,U}$	1.5 GHz
Spatial sampling distance, T_x and T_y	7.5 cm
Temporal sampling frequency, $f_{t,S}$	4 GHz
Half-cone angle, ϵ	30°

Table 3.1: Design specifications of the 3D frustum filter banks.

of bands of the frustum filter banks are chosen as $40 \times 40 \times 254$ and 32, respectively. Note that, the total number of bands is the number of bands M in the corresponding cone filter banks. Accordingly, the order of the temporal prototype filter, N_P, and the order of the 2D spatial filters, $N_{Sx} \times N_{Sy}$, are obtained as 127 (i.e., $4M - 1$) and 40×40, respectively.

Design Using the DFT-Polyphase Frustum Filter Bank

The prototype type filter of the temporal filter bank is designed as described in Section 3.3.1. The value of the parameter γ in the objective function given in (3.18) is selected as 0.5 so that the weights of the two terms, which represent the amplitude and aliasing distortions of the temporal filter bank, are the same. The optimum rolloff factor r_{opt} is obtained as 0.56. The normalized amplitude response of the prototype filter is illustrated in Figure 3.11. It is observed that the minimum stopband attenuation is greater than 30 dB.

In this example, 18 bands out of 32 bands are used to approximate the double-frustum-shaped passband. More specifically, the set $\mathcal{F}$ is given by $\mathcal{F} = \mathcal{F}_U \cup \mathcal{F}_L$, where $\mathcal{F}_U = \{4, 5, \ldots, 12\}$ and $\mathcal{F}_L = \{20, 21, \ldots, 28\}$ are the sets containing the indices of the bands used to form the upper ($\omega_{ct,L} \leq \omega_{ct} \leq \omega_{ct,U}$) and lower ($-\omega_{ct,U} \leq \omega_{ct} \leq -\omega_{ct,L}$) frustum-shaped passbands, respectively. The lower and upper temporal

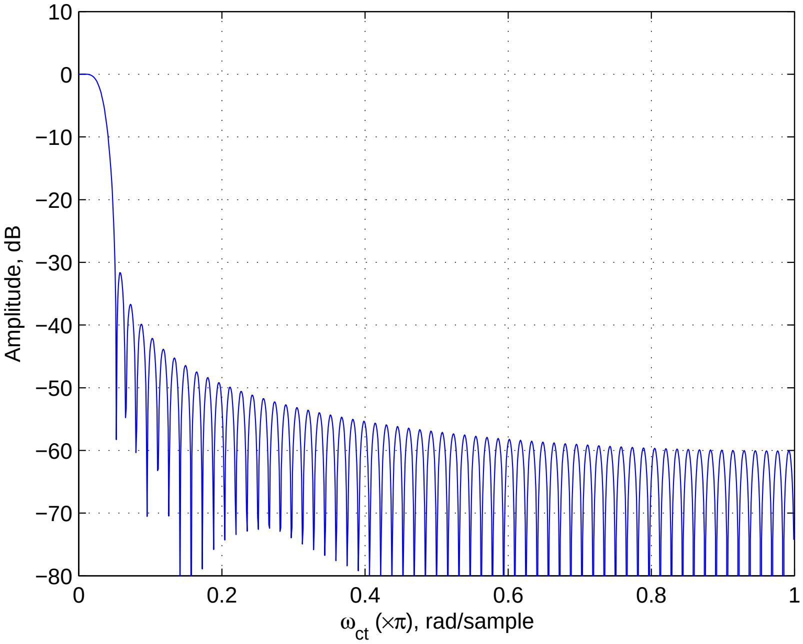

Figure 3.11: Amplitude response of the temporal prototype filter of the temporal DFT filter bank. Passband gain is normalized to unity.

cutoff frequencies of the approximated double-frustum-shaped passband are 0.22π rad/sample and 0.78π rad/sample, respectively. The error between the approximated and specified temporal cutoff frequencies is 0.03π rad/sample. In the design of the 2D spatial filters, the 2D circular Hamming window is used. The -3 dB iso-surface of the amplitude response of the DFT frustum filter $FFB_{\mathrm{DFT}}(z_x, z_y, z_{ct})$ is depicted in Figure 3.12. It is observed that the -3 dB iso-surface closely approximates the required double-frustum-shaped passband.

To further verify the amplitude response of the DFT frustum filter bank, that across planes and along lines in the 3D frequency space are considered. Figures 3.13(a) and 3.13 (b) depict $|FFB_{\mathrm{DFT}}(\mathrm{e}^{j\omega_x}, \mathrm{e}^{j\omega_y}, \mathrm{e}^{j\omega_{ct}})|$ across the $\omega_{ct} = 0.625\pi$ plane and along the line on the $\omega_{ct} = 0.625\pi$ plane that is parallel to the ω_x axis, respectively. According to these two figures, the minimum stopband attenuation of the DFT frustum filter bank at $\omega_{ct} = 0.625\pi$ is greater than 50 dB. An enlarged section corresponding to the passband of the amplitude response shown in Figure 3.13 (b) is shown in Figure 3.13 (c). It is observed that the maximum passband ripple is less than 0.2 dB. Furthermore, the amplitude response across the $\omega_y = 0$ plane and along the ω_{ct} axis is illustrated in Figures 3.13 (d) and 3.13 (e), respectively. As a result

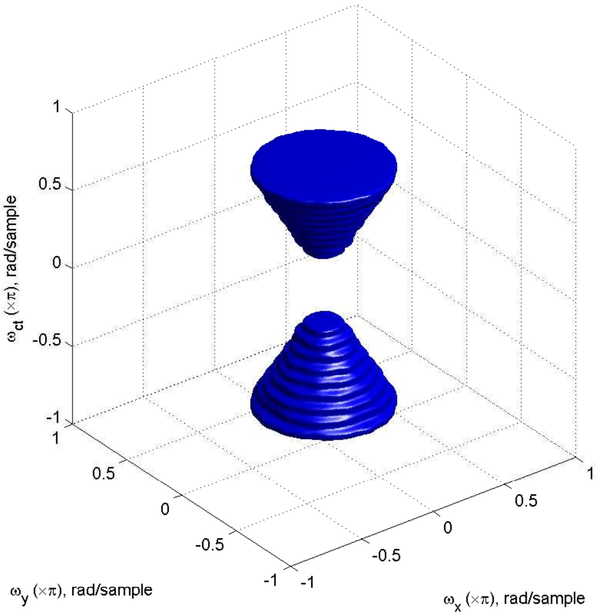

Figure 3.12: −3 dB iso-surface of the amplitude response of the 3D DFT frustum filter bank.

of the cascade of the temporal and spatial filters, hence, the multiplication of the corresponding frequency responses, the stopband attenuation across the $\omega_y = 0$ plane varies substantially from region to region. According to Figure 3.13 (d), the minimum stopband attenuation is roughly 60 dB while the maximum is approximately 150 dB. Figure 3.13 (f) depicts the amplitude response in the *specified* temporal passband (i.e., 0.25π–0.75π rad/sample) along the ω_{ct} axis. It is observed that the maximum passband ripple is approximately 0.15 dB. These illustrations confirm that the designed DFT frustum filter bank satisfies the design specifications.

In order to estimate the distortion due to aliasing, the 3D aliasing distortion function $D(\mathrm{e}^{j\omega_x}, \mathrm{e}^{j\omega_y}, \mathrm{e}^{j\omega_{ct}})$ is defined as [3][91](pp. 367)

$$D(\mathrm{e}^{j\omega_x}, \mathrm{e}^{j\omega_y}, \mathrm{e}^{j\omega_{ct}}) = \left[\sum_{l=1}^{M/2-1} \left| A_l(\mathrm{e}^{j\omega_x}, \mathrm{e}^{j\omega_y}, \mathrm{e}^{j\omega_{ct}}) \right|^2 \right]^{1/2}, \tag{3.53}$$

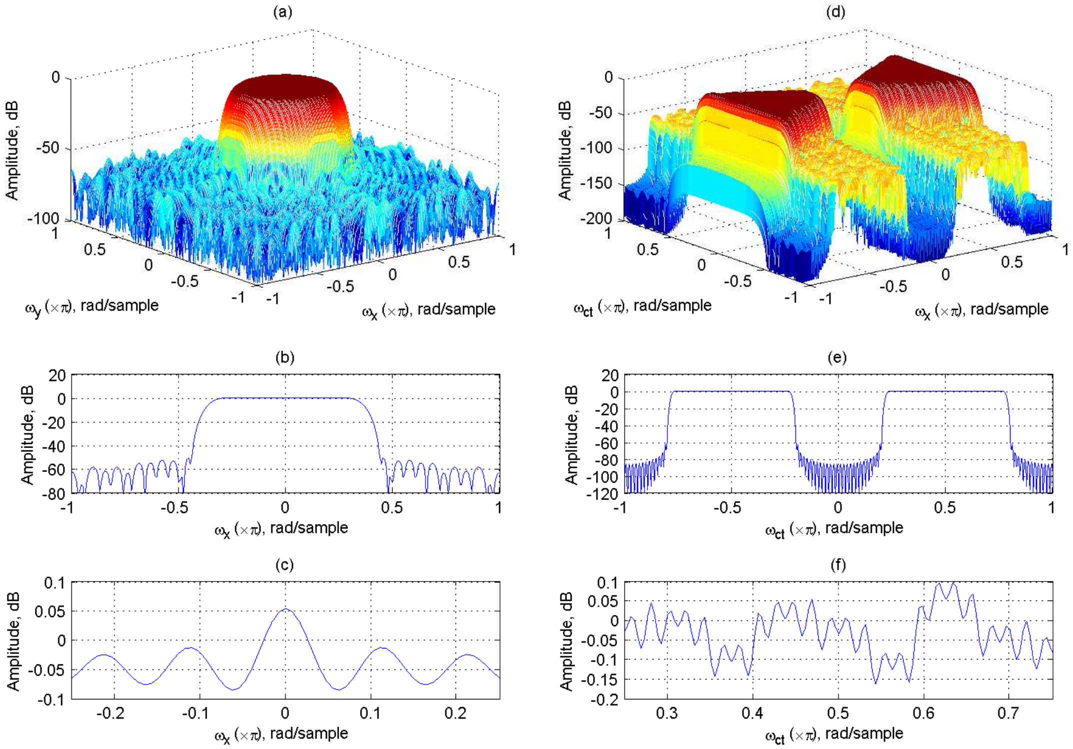

Figure 3.13: Amplitude response of the DFT frustum filter bank across the planes and along the lines in the 3D frequency space (a) across the $\omega_{ct} = 0.625\pi$ plane (b) along the line on the $\omega_{ct} = 0.625\pi$ plane that is parallel to the ω_x axis. (c) an enlarged section corresponding to the passband of the amplitude response shown in (b) (d) across the $\omega_y = 0$ plane (e) along the ω_{ct} axis (f) in the *specified* temporal passband (along the ω_{ct} axis).

where

$$A_l(\mathrm{e}^{j\omega_x}, \mathrm{e}^{j\omega_y}, \mathrm{e}^{j\omega_{ct}}) = \frac{2}{M} \sum_{k \in \mathcal{F}} H_k(\mathrm{e}^{j\omega_{ct}} W_M^{2l}) G_k(\mathrm{e}^{j\omega_x}, \mathrm{e}^{j\omega_y}) F_k(\mathrm{e}^{j\omega_{ct}}),$$

$$l = 1, 2, \ldots, (M/2 - 1). \tag{3.54}$$

Figure 3.14 depicts the maximum aliasing distortion, $\max[D(\mathrm{e}^{j\omega_x}, \mathrm{e}^{j\omega_y}, \mathrm{e}^{j\omega_{ct}})]$, along lines parallel to the ω_{ct} axis. It is observed that the maximum aliasing distortion is approximately -40 dB inside the double-frustum-shaped passband. Consequently, the DFT frustum filter bank is almost alias free and closely approximates a linear time-invariant system.

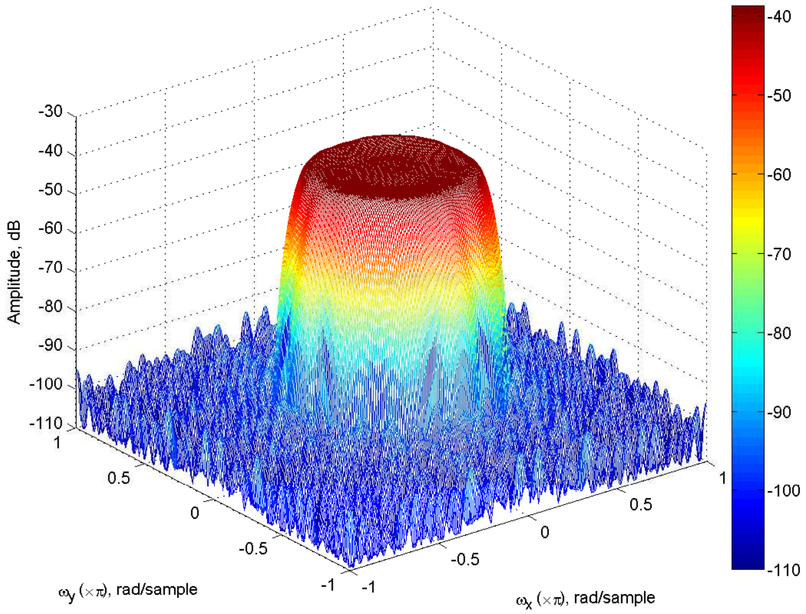

Figure 3.14: Maximum aliasing distortion of the DFT frustum filter bank, $\max[D(\mathrm{e}^{j\omega_x}, \mathrm{e}^{j\omega_y}, \mathrm{e}^{j\omega_{ct}})]$, along lines parallel to the ω_{ct} axis.

Design Using the Modified DFT-Polyphase Frustum Filter Bank

As mentioned in Section 3.4.2, for 1D modified DFT filter banks, the design of prototype filters leading to perfect reconstruction has to be carried out via nonlinear optimization techniques [87]. The coefficients of prototype filters that have been designed by means of the method described in [102] are given in [87] for several M values, and, for this design, the prototype filter of order 127, designed for 32 bands, is employed. The normalized amplitude response of the employed prototype filter is illustrated in Figure 3.15. It is observed that the average stopband attenuation is greater than 40 dB.

The same set of temporal frequency bands used to design the DFT frustum filter bank are used to approximate the double-frustum-shaped passband. Therefore, as in the DFT frustum filter bank, the lower and upper temporal cutoff frequencies of the approximated double-frustum-shaped passband are 0.22π rad/sample and 0.78π rad/sample, respectively, and the error between the approximated and specified temporal cutoff frequencies is 0.03π rad/sample. Furthermore, in the design of the 2D spatial filters, the 2D circular Hamming window is used. The -3 dB iso-surface of the amplitude response of the modified DFT frustum filter bank $FFB_{\mathrm{MoDFT}}(z_x, z_y, z_{ct})$ is

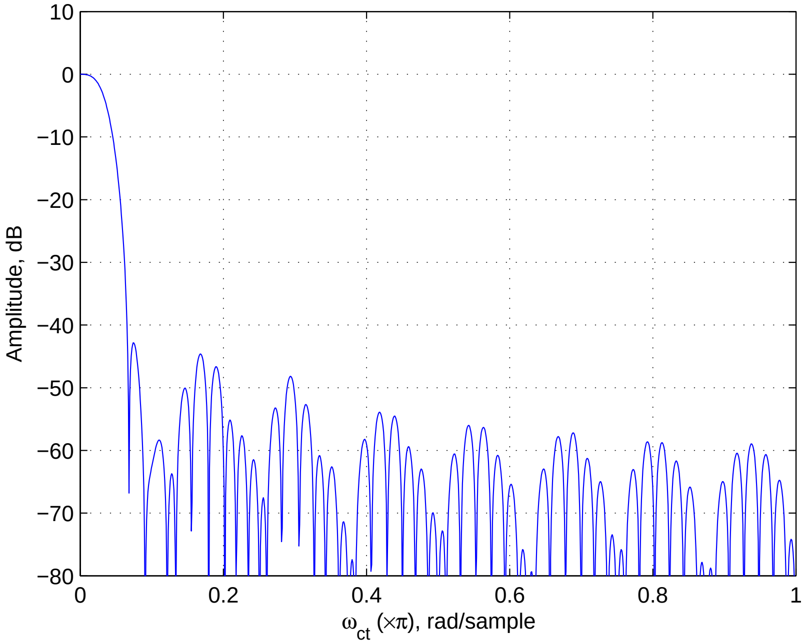

Figure 3.15: Amplitude response of the temporal prototype filter of the temporal modified DFT filter bank. Passband gain is normalized to unity.

depicted in Figure 3.16. It is observed that the -3 dB iso-surface closely approximates the required double-frustum-shaped passband.

The amplitude response of the modified DFT frustum filter bank across the $\omega_{ct} = 0.625\pi$ plane and along the line on the $\omega_{ct} = 0.625\pi$ plane that is parallel to the ω_x axis is illustrated in Figures 3.17 (a) and 3.17 (b), respectively. Accordingly, the minimum stopband attenuation of the modified DFT frustum filter bank at $\omega_{ct} = 0.625\pi$ is greater than 60 dB. Figure 3.17 (c) depicts an enlarged section corresponding to the passband of the amplitude response shown in Figure 3.17 (b). As in the DFT frustum filter bank, the maximum passband ripple is less than 0.2 dB. Furthermore, the amplitude response across the $\omega_y = 0$ plane and along the ω_{ct} axis are shown in Figures 3.17 (d) and 3.17 (e), respectively. Similar to the stopband attenuation of the DFT frustum filter bank, across the $\omega_y = 0$ plane, that of the modified DFT frustum filter bank varies substantially from region to region. According to Figure 3.17 (d), the minimum stopband attenuation is roughly 60 dB while the maximum is approximately 150 dB. Furthermore, the amplitude response in the *specified* temporal passband (i.e., 0.25π–0.75π rad/sample) along the ω_{ct} axis is illustrated in Figure 3.17 (f). It is observed that the maximum passband ripple is approximately 0.1

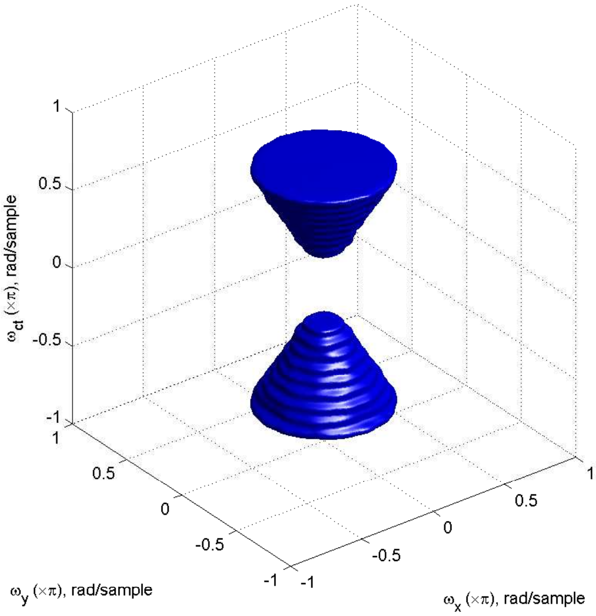

Figure 3.16: −3 dB iso-surface of the amplitude response of the 3D modified DFT frustum filter bank.

dB. Accordingly, we can conclude that the modified DFT frustum filter bank satisfies the design specifications.

The 3D aliasing distortion function $D(\mathrm{e}^{j\omega_x}, \mathrm{e}^{j\omega_y}, \mathrm{e}^{j\omega_{ct}})$ defined in Equation (3.53) is used to estimate the distortion due to aliasing. In this case, $A_l(\mathrm{e}^{j\omega_x}, \mathrm{e}^{j\omega_y}, \mathrm{e}^{j\omega_{ct}})$ is given by

$$A_l(\mathrm{e}^{j\omega_x}, \mathrm{e}^{j\omega_y}, \mathrm{e}^{j\omega_{ct}}) = \frac{1}{M} \sum_{k \in \mathcal{F}} H_k(\mathrm{e}^{j\omega_{ct}} W_M^{2l}) G_k(\mathrm{e}^{j\omega_x}, \mathrm{e}^{j\omega_y}) F_k(\mathrm{e}^{j\omega_{ct}}),$$
$$l = 1, 2, \ldots, (M/2 - 1). \tag{3.55}$$

The maximum aliasing distortion, $\max[D(\mathrm{e}^{j\omega_x}, \mathrm{e}^{j\omega_y}, \mathrm{e}^{j\omega_{ct}})]$, along lines parallel to the ω_{ct} axis is illustrated in Figure 3.18. It is observed that the maximum aliasing distortion is approximately −45 dB inside the double-frustum-shaped passband. Therefore, similar to the DFT frustum filter bank, the modified DFT frustum filter bank is almost alias free and closely approximates a linear time-invariant system.

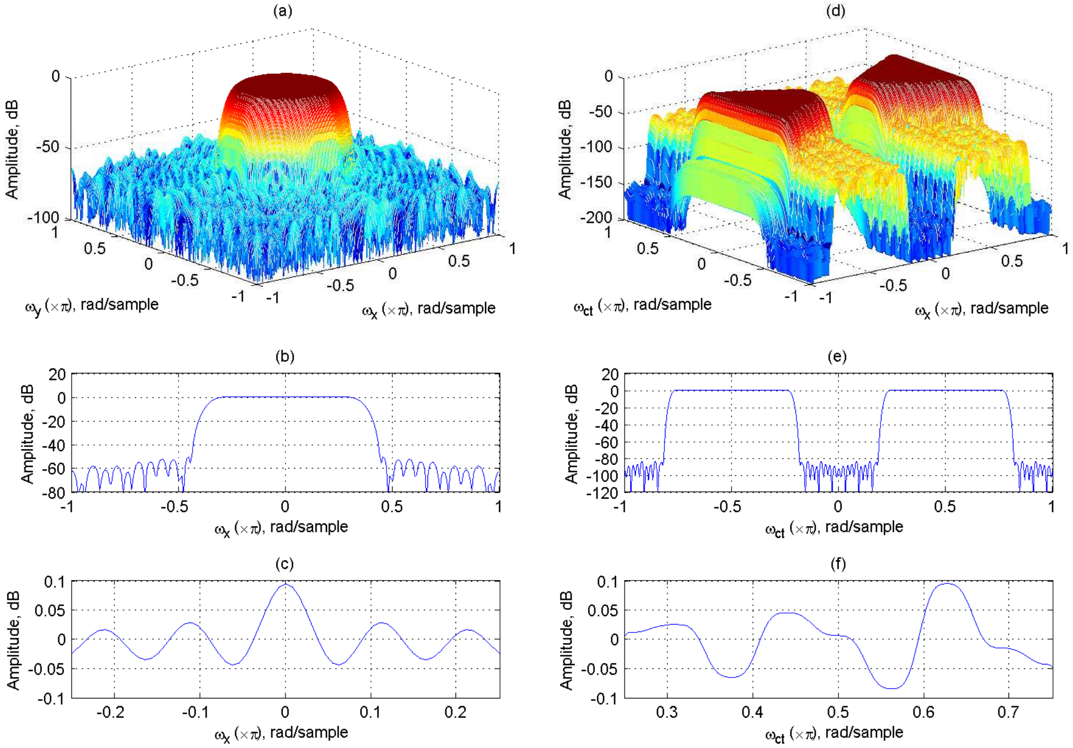

Figure 3.17: Amplitude response of the modified DFT frustum filter bank across the planes and along the lines in the 3D frequency space (a) across the $\omega_{ct} = 0.625\pi$ plane (b) along the line on the $\omega_{ct} = 0.625\pi$ plane that is parallel to the ω_x axis. (c) an enlarged section corresponding to the passband of the amplitude response shown in (b) (d) across the $\omega_y = 0$ plane (e) along the ω_{ct} axis (f) in the *specified* temporal passband (along the ω_{ct} axis).

3.6.2 A Comparative Analysis of the Improvement in SINR Achieved with 3D Frustum Filter Banks with DAAs

In the following numerical analysis, a BB SOI and two terrestrial BB RFI signals are considered to be received by a DAA consisting of 41 × 41 elemental antennas having *isotropic* radiation patterns. The elemental antennas are assumed to be arranged rectangularly with the inter antenna distance $T_x = T_y = 7.5$ cm. Furthermore, the temporal sampling frequency $f_{t,S}$ is chosen as 4 GHz (corresponding $f_{ct,S} = f_{t,S}/\mathrm{c} = 13.33\ \mathrm{m}^{-1}$, and $T_{ct} = 1/f_{ct,S} = 7.5$ cm, where $\mathrm{c} = 3 \times 10^8\ \mathrm{ms}^{-1}$). For simplicity, we assume the SOI and the two RFI signals are in only one linear polarization. Consequently, they are treated as *scalar* quantities. The specifications of the SOI

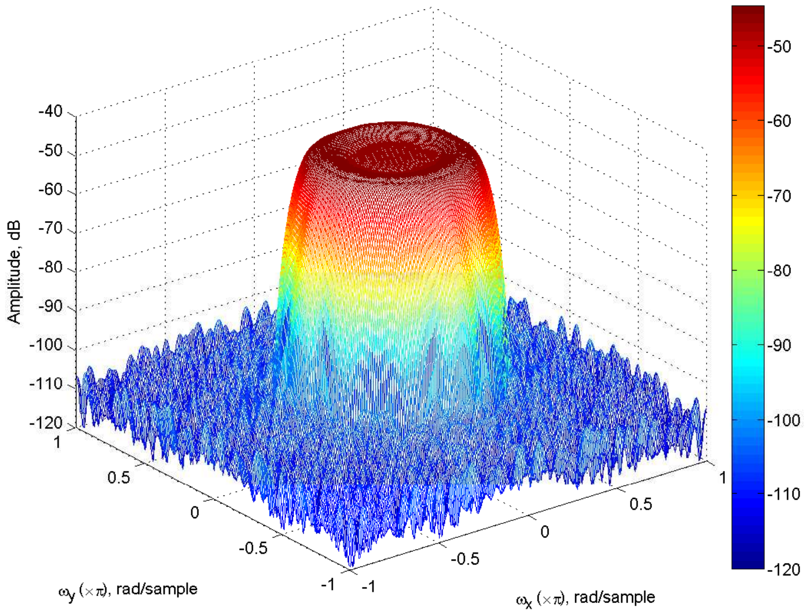

Figure 3.18: Maximum aliasing distortion of the modified DFT frustum filter bank, $\max[D(\mathrm{e}^{j\omega_x}, \mathrm{e}^{j\omega_y}, \mathrm{e}^{j\omega_{ct}})]$, along lines parallel to the ω_{ct} axis.

and the two RFI signals are given in Table 3.2. Note that, the bandwidth of the SOI entirely covers the SKA lower mid-band. In addition to the SOI and the two RFI signals, a white Gaussian noise signal that represents the receiver noise is incorporated in the simulations. The size of the each signal is chosen as $41 \times 41 \times 1024$. Furthermore, to represent a weak SOI, energy of the each RFI signal and that of the white Gaussian noise signal are, respectively, selected as 30 dB and 20 dB higher than the energy of the SOI, which is chosen as unity.

The sampled signal $x_{DAA}(n_x, n_y, n_{ct})$ at the input of a frustum filter bank can be expressed as

$$\begin{aligned} x_{DAA}(n_x, n_y, n_{ct}) = soi_{DAA}(n_x, n_y, n_{ct}) + rfi1_{DAA}(n_x, n_y, n_{ct}) \\ + rfi2_{DAA}(n_x, n_y, n_{ct}) + wgn_{DAA}(n_x, n_y, n_{ct}), \\ |n_x| \leq 20, \;\; |n_y| \leq 20 \;\; \text{and} \;\; 0 \leq n_{ct} \leq 1023, \end{aligned} \quad (3.56)$$

where $soi_{DAA}(n_x, n_y, n_{ct})$, $rfi1_{DAA}(n_x, n_y, n_{ct})$, $rfi2_{DAA}(n_x, n_y, n_{ct})$ are the sampled signals corresponding to the SOI, RFI signal 1 and the RFI signal 2, respectively, and $wgn_{DAA}(n_x, n_y, n_{ct})$ is the sampled white Gaussian noise signal. The sampled

Signal	(θ, ϕ)	(α, β)	Bandwidth
SOI	$(0^\circ, 0^\circ)$	$(0^\circ, 0^\circ)$	0.5–1.5 GHz
RFI 1	$(85^\circ, 40^\circ)$	$(44.89^\circ, 40^\circ)$	0.1–1.2 GHz
RFI 2	$(87^\circ, -110^\circ)$	$(44.96^\circ, -110^\circ)$	0.9–1.8 GHz

Table 3.2: Specifications of the SOI and the two RFI signals considered to be received by the DAA.

signals $soi_{DAA}(n_x, n_y, n_{ct})$, $rfi1_{DAA}(n_x, n_y, n_{ct})$ and $rfi2_{DAA}(n_x, n_y, n_{ct})$, which are *sampled* ST PWs having random-valued wavefronts, are numerically synthesized by superimposing monochromatic ST PWs having frequencies that densely cover the specified bandwidths. For example, the mathematical expression corresponding to the synthesis of the SOI is given by

$$soi_{DAA}(n_x, n_y, n_{ct}) = \sum_{k=0}^{N_{soi}} A_k \cos\left[\frac{2\pi(f_i + kf_g)}{\mathrm{c}}(d_x n_x T_x + d_y n_y T_y + n_{ct} T_{ct})\right],$$
$$|n_x| \leq 20, \;\; |n_y| \leq 20 \;\text{ and }\; 0 \leq n_{ct} \leq 1023, \qquad (3.57)$$

where $N_{soi} = 100$, $f_i = 0.5$ GHz, $f_g = 10$ MHz, A_k is the amplitude of the kth monochromatic signal that is drawn from a Gaussian distribution with zero mean and unity standard deviation, $d_x = \sin(\theta_{soi})\cos(\phi_{soi})$, $d_y = \sin(\theta_{soi})\sin(\phi_{soi})$ and $(\theta_{soi}, \phi_{soi})$ specifies the DOA of the SOI (Numerical values are given in Table 3.2.). Figure 3.19 depicts the iso-surface, drawn at 0.1, of the normalized magnitude spectrum of the signal obtained by summing the SOI and the two RFI signals[5]. According to Figure 3.19, as expected, the main lobes of the ROSs of the spectra of the two RFI signals do not overlap with the main lobe of the ROS of the spectrum of the SOI. Furthermore, first 501 samples of the 1D temporal sequence of the SOI that is corresponding to the middle elemental antenna of the DAA, i.e., $soi_{DAA}(21, 21, n_{ct})$, $0 \leq n_{ct} \leq 500$, is illustrated in Figure 3.20. The 41×41 temporal sequences of the white Gaussian noise signal are obtained from Gaussian distributions with zero mean and unity standard deviation, and the samples of the 3D signal are scaled appropriately so that the energy content is 20 dB higher than the energy of the SOI as required.

---

[5] To include the spectra of all three signals in the same figure, numerical values of the samples of the signals are scaled so that the energy of each signal is unity.

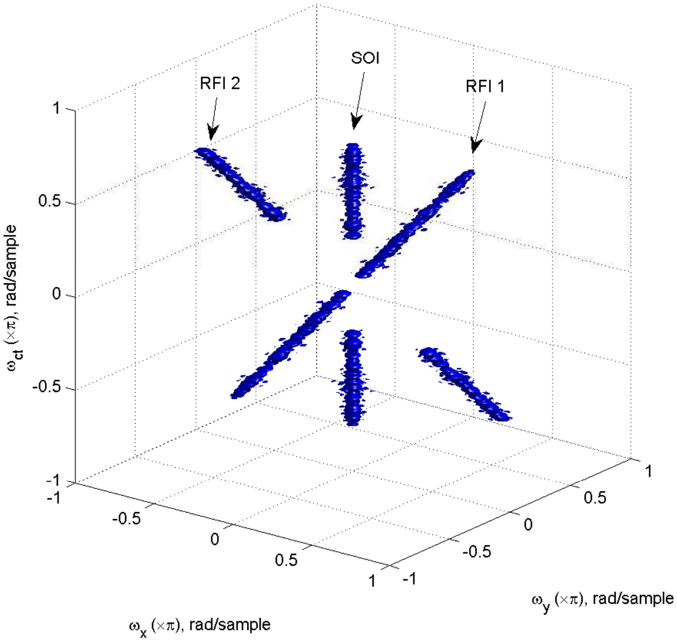

Figure 3.19: Iso-surface, drawn at 0.1, of the normalized magnitude spectrum of the signal obtained by summing the SOI and the two RFI signals received by the DAA.

A set of DFT and modified DFT frustum filter banks (order $40 \times 40 \times 254$) having half-cone angles $5°, 7.5°, \dots, 42.5°$ are used in the simulations. The same temporal cutoff frequencies (see Table 3.1), total bands M and the prototype filters that are used for the examples given in the previous subsection are used in the design. Also, a set of undecimated frustum filter banks having the same order and half-cone angles are designed from the undecimated cone filter banks following a similar approach used in the design of the DFT and modified DFT frustum filter banks. The number of *total* real bands L is selected as 16, and the middle 8 real bands are employed in the frustum filters. In contrast to the DFT and modified DFT frustum filter banks, in this case, the lower and upper temporal cutoff frequencies of the approximated double-frustum-shaped passband exactly coincide with the specified ones. Note that, the approximated double-frustum-shaped passband of an undecimated frustum filter bank is slightly wider than that of a DFT or a modified DFT frustum filter bank for the same half-cone angle since the cutoff frequencies of the 2D spatial filters of the former are different from those of the 2D spatial filters of the latter two.

The SINRs at the inputs and outputs of the three frustum filter banks are illustrated in Figure 3.21. The SINRs at the outputs of the frustum filter banks decrease

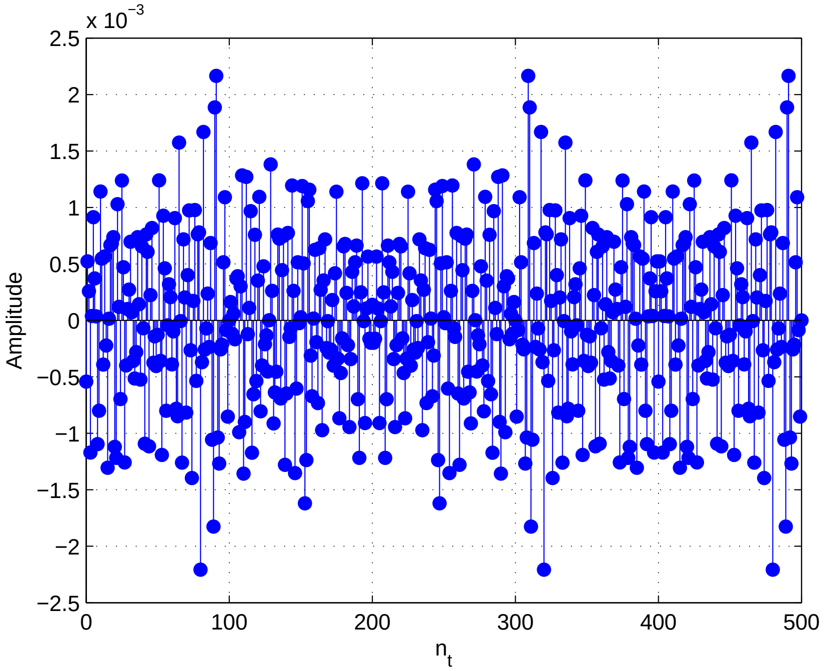

Figure 3.20: First 501 samples of the 1D temporal sequence of the SOI that is corresponding to the middle antenna of the DAA ($soi_{DAA}(21, 21, n_{ct})$, $0 \leq n_{ct} \leq 500$).

with the increased half-cone angle because more of the energy of the RFI and noise signals encroaches into the double-frustum-shaped passband. *More importantly, the SINR improvements achieved with the DFT and modified DFT frustum filter banks are comparable with that achieved with the undecimated frustum filter bank for most of the half-cone angles. Furthermore, the SINR improvements achieved with the DFT and modified DFT frustum filter banks are almost identical for all the half-cone angles used in the simulations.* It is observed that the DFT and modified DFT frustum filter banks provide a slightly better SINR improvement than that provides by the undecimated frustum filter bank for the half-cone angles greater than 35° whereas the opposite is true for the half-cone angles less than 7.5°. This discrepancy exists mainly as a result of the slightly wider passbands of the undecimated frustum filter banks. In fact, the volume of the ROS of the spectrum of a signal that is inside the double-frustum-shaped passband of a undecimated frustum filter bank is greater than the volume of the ROS of the spectrum of the same signal that is inside the double-frustum-shaped passbands of the DFT and modified DFT frustum filter banks for the same half-cone angle, and the difference between the energy content inside the double-frustum-shaped passbands is substantial when the boundary of the double

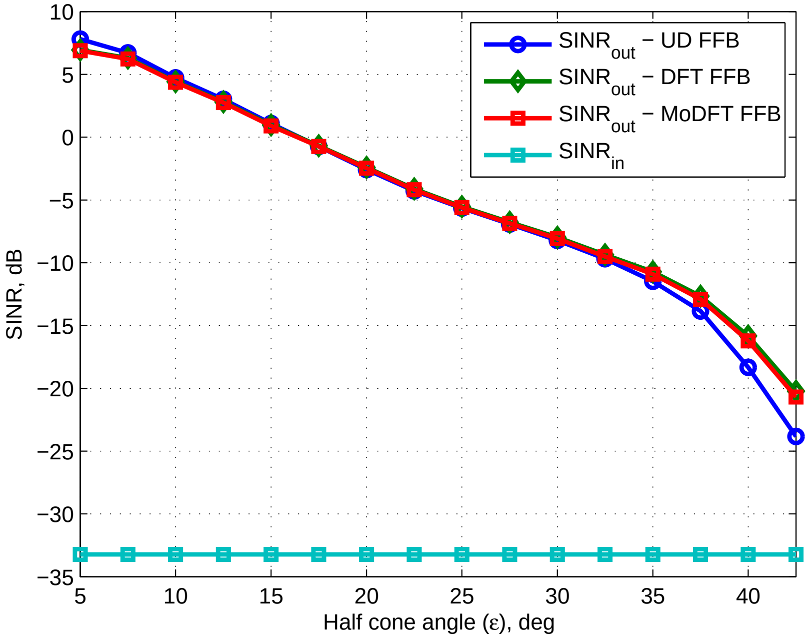

Figure 3.21: SINRs at the inputs and outputs of the undecimated, DFT and modified DFT frustum filter banks for the DAA.

frustum is close to the main lobe of the ROS of the spectrum of the signal.

3.6.3 A Comparative Analysis of the Improvement in SINR Achieved with 3D Frustum Filter Banks with FPAs

In this case, we consider an FPA consisting of 15 × 15 elemental antennas each of which has an *isotropic* radiation pattern. The FPA is assumed to be mounted on a prime-focus paraboloidal reflector of diameter $D = 15$ m and focal length $F = 6.75$ m. The focal length to diameter ratio F/D is 0.45, and the subtended angle θ_{Fmax} is 58.11° (corresponding $\alpha_{Fmax} = 40.33°$). As in the case of the DAA, the elemental antennas are assumed to be arranged rectangularly with the inter antenna distance $T_x = T_y = 7.5$ cm, and the temporal sampling frequency $f_{t,S}$ is chosen as 4 GHz. Furthermore, the same signal composition (i.e., a BB SOI, two BB RFI signals and a white Gaussian noise) and the same energy levels (i.e., the energy of the SOI is unity whereas the energy of the each RFI signal and that of the white Gaussian noise signal are 30 dB and 20 dB higher than the energy of the SOI, respectively.) are assumed. Moreover, the DOAs and bandwidths of the two RFI signals are chosen as the same as those of the two RFI signals employed in the case of the DAA (see Table 3.2). The DOA[6] and the bandwidth of the SOI are selected as $(-180°, 0°)$, i.e., the broadside direction, and 0.5–1.5 GHz, respectively. Note that, as in the case of the DAA, the bandwidth of the SOI entirely covers the SKA lower mid-band. The size of the each signal is chosen as $15 \times 15 \times 1024$. Furthermore, for simplicity, we assume the SOI and the two RFI signals are in only one linear polarization.

The sampled signal $x_{FPA}(n_x, n_y, n_{ct})$ at the input of a frustum filter bank can be expressed as

$$\begin{aligned} x_{FPA}(n_x, n_y, n_{ct}) = {} & soi_{FPA}(n_x, n_y, n_{ct}) + rfi1_{FPA}(n_x, n_y, n_{ct}) \\ & + rfi2_{FPA}(n_x, n_y, n_{ct}) + wgn_{FPA}(n_x, n_y, n_{ct}), \\ & |n_x| \leq 7, \ \ |n_y| \leq 7 \ \text{ and } \ 0 \leq n_{ct} \leq 1023, \end{aligned} \tag{3.58}$$

where $soi_{FPA}(n_x, n_y, n_{ct})$, $rfi1_{FPA}(n_x, n_y, n_{ct})$, $rfi2_{FPA}(n_x, n_y, n_{ct})$ are the sampled signals corresponding to the SOI, RFI signal 1 and the RFI signal 2, respectively, and $wgn_{FPA}(n_x, n_y, n_{ct})$ is the sampled white Gaussian noise signal. The same techniques used to numerically synthesize the two RFI signals and the white Gaussian noise signal in the previous subsection are used to synthesize the sampled signals $rfi1_{FPA}(n_x, n_y, n_{ct})$, $rfi2_{FPA}(n_x, n_y, n_{ct})$ and $wgn_{FPA}(n_x, n_y, n_{ct})$. However, the sampled SOI $soi_{FPA}(n_x, n_y, n_{ct})$ is synthesized using the *Focal Field Synthesizer* program [44](ch. 3) and the 1D inverse Fourier transform with respect to the temporal dimension. The iso-surface, drawn at 0.2, of the normalized magnitude spectrum of the SOI is illustrated in Figure 3.22. It is observed that, as expected, the ROS of the spectrum of the SOI is predominantly a double-frustum-shaped volume. Moreover, first 501 samples of the 1D temporal sequence of the SOI that is corresponding to the middle elemental antenna of the FPA, i.e., $soi_{FPA}(8, 8, n_{ct})$, $0 \leq n_{ct} \leq 500$, is shown in Figure 3.23.

A set of DFT, modified DFT and undecimated frustum filter banks having half-cone angles $40.5°, 40.75°, \ldots, 44.5°$ are used in the simulations. The order of the frustum filter banks is chosen as $14 \times 14 \times 254$, and the same design specifications used to design the frustum filter banks employed with the DAA are used here too. Furthermore, the same temporal prototype filters are used to design the DFT and modified DFT frustum filter banks.

---

[6] Here, we mean the DOA corresponding to the propagation of the SOI from the source to the paraboloidal reflector.

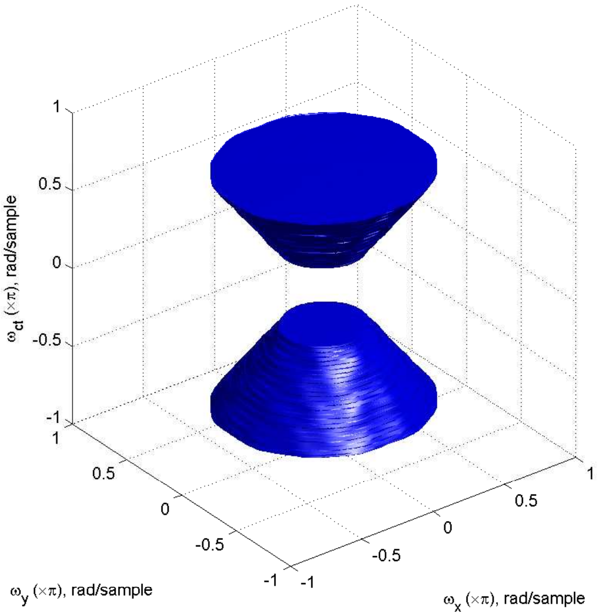

Figure 3.22: Iso-surface, drawn at 0.2, of the normalized magnitude spectrum of the SOI received by the FPA.

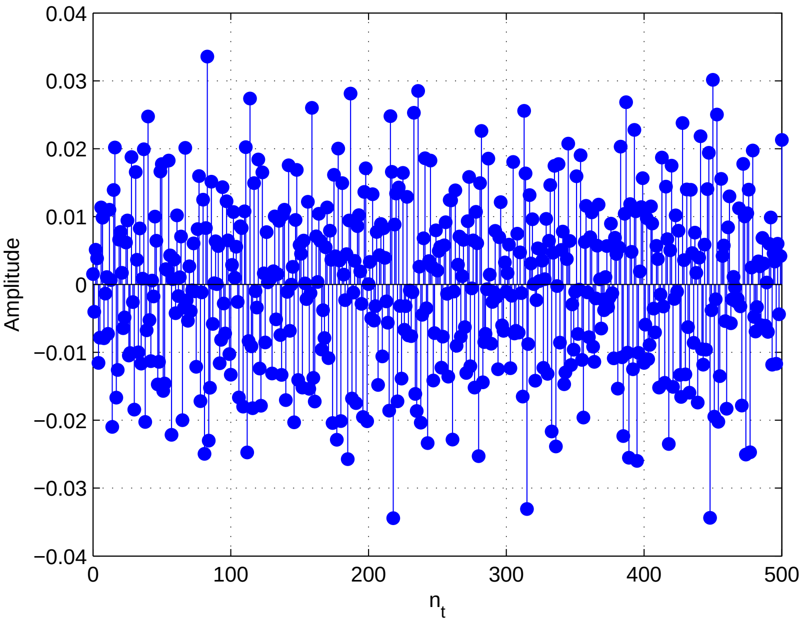

Figure 3.23: First 501 samples of the 1D temporal sequence of the SOI that is corresponding to the middle antenna of the FPA ($soi_{FPA}(8, 8, n_{ct})$, $0 \leq n_{ct} \leq 500$).

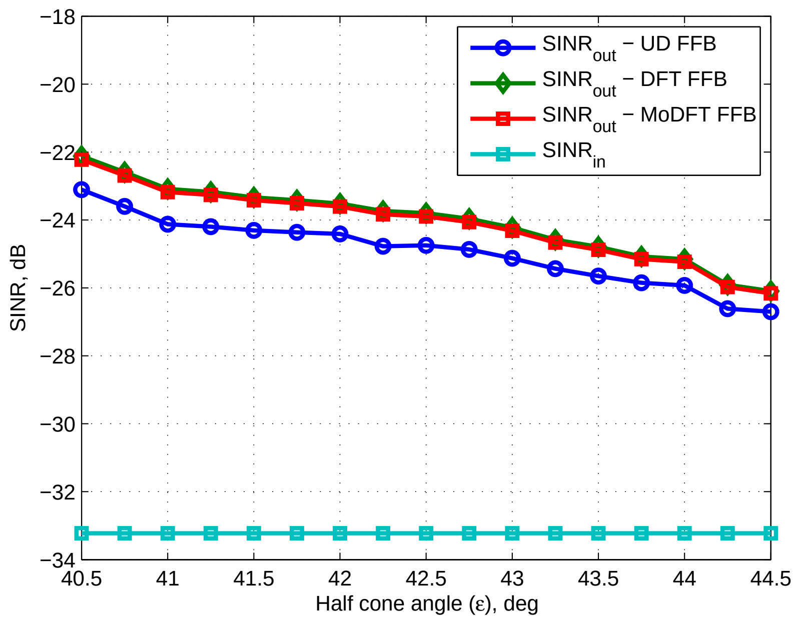

Figure 3.24: SINRs at the inputs and outputs of the undecimated, DFT and modified DFT frustum filter banks for the FPA.

The SINRs at the inputs and outputs of the three frustum filter banks are illustrated in Figure 3.24. Similar to the case of the DAA, the SINRs at the outputs of the frustum filter banks decrease with the increased half-cone angle because more energy of the RFI and noise signals encroaches into the double-frustum-shaped passbands. *It is observed that an additional SINR improvement about* 1 *dB can be achieved with the DFT and modified DFT frustum filter banks for all the half-cone angles used in the simulations.* One main reason among others for this additional improvement may be the difference between the approximated double-frustum-shaped passbands.

3.6.4 A Comparative Study of Computational Complexity of 3D FIR Frustum Filter Banks

In order to numerically confirm the lower computational complexity of a DFT and a modified DFT frustum filter bank compared to a undecimated frustum filter bank having the same order, hence, a similar frequency response, here, we present the *nontrivial* real multiplications and additions (i.e., excluding the multiplications with ± 1 and $\pm j$ and the addition with 0, respectively) required by each of three frustum filter banks to process a real-valued and a complex-valued sample. As illustrative

Filter order	DFT		Modified DFT		Undecimated	
	Mul.	Add.	Mul.	Add.	Mul.	Add.
$40 \times 40 \times 254$	3813.375	3834.25	1921.125	1940.875	15488	15479
$14 \times 14 \times 254$	537.375	558.25	283.125	302.875	3840	3831

Table 3.3: Number of nontrivial real multiplications and additions required to process a real-valued sample by the DFT, modified DFT and the undecimated frustum filter banks of order $40 \times 40 \times 254$ and $14 \times 14 \times 254$.

examples, we consider the frustum filter banks employed in the processing of the ST signals on the DAA and the FPA in Sections 3.6.2 and 3.6.3, respectively.

The number of nontrivial real multiplications and additions required by the DFT, modified DFT and the undecimated frustum filter banks to process a real-valued and a complex-valued sample are given in Tables 3.3 and 3.4, respectively. A detailed derivation of the computational complexities of the three cone and frustum filter bank types is presented in Appendix A. In this case, it is assumed that the *split-radix* FFT algorithm is used to implement the DFT and IDFT blocks. The nontrivial real multiplications and additions required to perform a 32-point DFT (or IDFT) by the real-valued and complex-valued split-radix FFT algorithms are 34 and 164 [104] and 68 and 388 [105], respectively. The percentage reduction (or saving) of the total arithmetic operations, i.e., the summation of the nontrivial real multiplications and additions, required to process a real-valued and a complex-valued sample by the DFT and modified DFT frustum filter banks relative to the undecimated frustum filter bank is presented in Table 3.5. *It is observed that approximately* $75\% - 95\%$ *reduction of the total arithmetic operations can be achieved with the DFT and modified DFT frustum filter banks relative to the undecimated counterpart. Also, the saving of the total arithmetic operations is higher for a complex-valued signal. Furthermore, the percentage reduction of the total arithmetic operations required to process a real-valued sample by the modified DFT frustum filter bank relative to the DFT frustum filter bank is* 49.50% *and* 46.51% *for the frustum filter banks of order* $40 \times 40 \times 254$ *and* $14 \times 14 \times 254$*, respectively. In the case of a complex-valued sample, the percentage reduction is* 48.84% *and* 42.48%*, respectively. Consequently, roughly* $40\% - 50\%$ *reduction of the total arithmetic operations can be achieved with the modified DFT frustum filter banks relative to the DFT frustum filter banks at the expense of higher hardware cost.*

Filter order	DFT		Modified DFT		Undecimated	
	Mul.	Add.	Mul.	Add.	Mul.	Add.
$40 \times 40 \times 254$	3842	3909.75	1949.75	2016.375	30976	30958
$14 \times 14 \times 254$	566	633.75	311.75	378.375	7680	7662

Table 3.4: Number of nontrivial real multiplications and additions required to process a complex-valued sample by the DFT, modified DFT and the undecimated frustum filter banks of order $40 \times 40 \times 254$ and $14 \times 14 \times 254$.

Filter order	Real-valued signal		Complex-valued signal	
	DFT	Modified DFT	DFT	Modified DFT
$40 \times 40 \times 254$	75.30%	87.53%	87.48%	93.60%
$14 \times 14 \times 254$	85.72%	92.36%	92.18%	95.50%

Table 3.5: Percentage reduction of the total arithmetic operations required to process a real-valued and a complex-valued sample by the DFT and modified DFT frustum filter banks relative to the undecimated frustum filter bank.

3.7 Summary

In this chapter, we proposed two computationally efficient 3D cone filter bank structures: DFT and modified DFT, following [3][53] to improve the computational efficiency of 3D cone filter banks proposed in [38](ch. 5.5)[39]. In the DFT cone filter bank, a 1D under-decimated filter bank is used as the temporal filter bank, and each subband is comprised of a 2D spatial circularly symmetric zero-phase FIR filter between the 1D temporal linear-phase causal FIR analysis and synthesis filters. However, in the modified DFT cone filter bank, a 1D maximally decimated modified DFT filter bank is employed as the temporal filter bank, and each subband is comprised of two 2D spatial circularly symmetric zero-phase FIR filters having the same transfer function between a 1D temporal linear-phase causal analysis and a synthesis filter. Each subband of both cone filter banks forms a disc-shaped passband having an appropriate radius and a height of $2\pi/M$, where M is the number of bands in the cone filter banks, and the double-cone-shaped passbands are approximated by cascading those M disc-shaped passbands. Furthermore, we extend the 3D DFT and modified DFT cone filter bank structures to the 3D DFT and modified DFT frustum filter bank structures. In the frustum filter banks, the double-frustum-shaped passbands are approximated by employing appropriate subsets of bands out of the M total bands in the respective cone filter banks. Both DFT and modified DFT cone and frustum filter banks provide near-perfect reconstruction. That is, they are almost alias free, and the amplitude responses are approximately unity inside the double-cone-shaped and double-frustum-shaped passbands. Computationally efficient DFT-polyphase structures are employed in the implementation of the DFT and modified DFT cone and frustum filter banks. Both temporal and spatial filtering operations can be carried out at a significantly lower rate in the DFT and modified DFT cone and frustum filter banks compared to the undecimated cone and frustum filter banks implying lower power consumption in the DFT and modified DFT cone and frustum filter banks.

Design examples of the DFT and modified DFT frustum filter banks indicate that they can be designed to have a small passband ripple and a good stopband attenuation. Furthermore the distortion due to aliasing is almost negligible. Furthermore, numerical simulations confirm that the improvement in SINR that can be achieved with the DFT and modified DFT frustum filter banks by attenuating RFI and noise signals is comparable with that can be achieved with the undecimated frustum filter banks having the same order for the DAAs and slightly better than for the FPAs. More importantly, a significant reduction of the computational complexity can be achieved with the DFT and modified DFT frustum filter banks relative to the undecimated frustum filter banks. Furthermore, the computational complexity of a modified DFT frustum filter bank is approximately half of that of a DFT frustum filter bank having the same order. However, the implementation of the former requires approximately twice the hardware required by the implementation of the latter.

Chapter 4

Brightness Distribution Errors in Synthetic Aperture Radio Astronomy due to Perturbations in Receiver Transfer Functions

4.1 Introduction

In both radio and optical astronomy, the *angular resolution* of a telescope is a key factor that determines the quality of images obtained. The angular resolution of a typical single-antenna radio telescope[1] is in the range of a few tens to a few hundreds of arcseconds that is insufficient for many astronomical purposes [35](ch. 1.1). For example, the angular resolution of a radio telescope of which the antenna is a paraboloidal reflector of diameter 100 m is around 413 arcseconds at the wavelength of 20 cm. In comparison, the angular resolution of an optical telescope[2] of diameter 1 m is *theoretically* around 0.1 arcseconds at the wavelength of 500 nm. Nevertheless, the angular resolution of a radio telescope can be significantly improved by employing interferometry techniques [35][36](ch. 9), through which angular resolutions as high as a few milliarcseconds can be achieved.

---

[1] The angular resolution θ_r of a single-antenna radio telescope is given by $\theta_r = k\lambda/D$, where λ is the wavelength of the cosmic SOI, D is the diameter of the antenna and k is a factor of order unity that depends on details of antenna illumination [36](ch. 9.1).

[2] In optical astronomy, practically achievable angular resolution from the ground by conventional techniques is limited to around 1 arcseconds by turbulence in the troposphere [35](ch. 1.1).

A typical aperture synthesis radio telescope consists of more than one antenna, ranging from a few tens to a few thousands. For example, the VLA telescope consists of 27 paraboloidal reflectors [34] whereas the SKA will have 2000–3000 paraboloidal reflectors in addition to other types of antennas [6][7]. Each antenna pair forms a *baseline*, for which a sample of the visibility function of a cosmic source(s) is estimated through cross correlation. The BD and the visibility function of a spatially incoherent cosmic source are related to each other through the Fourier transform in accordance with the van Cittert-Zernike theorem [35](ch. 14). When we have a sufficiently large number of samples of the visibility function, an accurate image of the BD can be obtained through the inverse Fourier transform and a deconvolution procedure such as the CLEAN algorithm [35](ch. 11.2)[36](ch. 9.4).

The transfer functions of the elemental antennas in DAAs and FPAs and those of receivers connected to them tend to be slightly mismatched due to small random perturbations and tolerances in elemental-antenna and circuit parameters. In [26][27][28] [29][30][31], the impact of limitations of the receiver and antenna subsystems on the performance of aperture synthesis interferometric radiometers used in remote sensing [32] are thoroughly analyzed. In the context of aperture synthesis radio telescopes, Thompson and D'Addario [33] have analyzed and estimated loss in sensitivity and the introduction of errors in the calibration procedure due to various limitations and mismatches in RF and IF amplifiers and transmission lines and due to delay errors for the VLA radio telescope [34]. Nevertheless, there appears to be little analytical information in the literature about how parameter perturbations and mismatches among the many ideally-matched LNAs and AAFs employed in analog receiver channels impact on the BD of a synthesized image.

In this chapter, we analyze BD errors caused by parameter perturbations and mismatches among the ideally-matched transfer functions of receivers employed in synthetic aperture systems. For simplicity, we consider 1D aperture synthesis with a synthetic aperture system consisting of 1D DLAs, which mimic the 1D version of the more general 2D DAAs. However, the extension of the analysis from 1D to 2D aperture synthesis is straightforward. The analysis is mainly divided into two parts. First, we consider the BD errors caused by perturbations in the transfer functions of LNAs and AAFs. For LNAs and AAFs, those perturbations are primarily caused by process variations in manufacturing [54][55] and typical element tolerances [56](ch. 7), respectively. Here, we present a detailed theoretical analysis of characteristics of the *additive BD error* and its effects on the *synthesized BD* under three cases: completely matched, partially matched and unmatched transfer functions of the LNAs and AAFs.

It is well known that typical FIR digital filters and beamformers having *linear-phase responses* (or *constant group delays*) are widely used in many applications where minimum phase distortion is necessary because they do not introduce phase distortions on the signals being processed. However, for applications where some phase distortion is either tolerable or unimportant, in general, typical IIR digital filters and beamformers having *nonlinear-phase responses* are attractive because, for similar performance, an IIR filter or a beamformer needs fewer parameters (i.e., lower order in the transfer function) compared to an FIR counterpart, and, hence, its implementation requires less memory and has lower computational complexity [106](pp. 614). More importantly, it has been assumed that the phase responses of ST multidimensional filters and beamformers proposed to be employed in aperture synthesis radio telescopes [38][39][40][41][42] should be linear in order to avoid phase distortions. As the second part of the analysis, we investigate the conditions that should be satisfied by the transfer functions of 2D beamformers to eliminate errors caused by their phase responses. Here, we show that the sufficient condition to eliminate those errors is that the transfer functions are *matched* and their phase responses *are not necessary to be linear* suggesting the possible use of typical IIR beamformers.

Furthermore, we present a numerical study of the BD errors caused by parameter perturbations and mismatches in the transfer functions of LNAs and AAFs. The study is mainly focused on the BD errors caused by the typical tolerances of passive L and C elements used to implement LC AAFs and those caused by the random variations of gain from LNA to LNA. With perturbed AAFs, the percentage errors of the synthesized BDs for both partially matched and unmatched cases are substantial at frequencies near the passband edge. The variations of the percentage errors due to the random variations of the gains of the LNAs are random and depend on additive perturbations for both partially matched and unmatched cases.

The organization of the chapter is as follows. In Section 4.2, an idealized model of a 2D synthetic aperture system is reviewed. The theoretical analysis of BD errors caused by perturbations in the receiver transfer functions is presented in Section 4.3. In Section 4.4, the BD errors caused by the typical tolerances of passive L and C elements used to implement LC AAFs and the random variations of gain from LNA to LNA are numerically studied using an illustrative example. Finally, in Section 4.5, summary of the chapter is presented.

4.2 An Idealized Model of a 2D Synthetic Aperture System: A Review

Here, we present a review of an ideal model of a simplified 2D synthetic aperture system. The telescope is assumed to be comprised of N_D 1D DLAs that are sparsely placed in the east-west direction, where $N_D \in \mathbb{Z}^+$, and the pth such DLA, where $p \in \{\mathbb{Z} \cap [1, N_D]\}$, and the corresponding simplified receiver architecture is illustrated in Figure 4.1. In the following analysis, each 1D DLA is considered to be associated with a separate Cartesian coordinate system of which the origin and the x axis are positioned at the middle of the corresponding 1D DLA and parallel to the east-west direction, respectively. Each DLA consists of $2N_x + 1$ elemental antennas, where $N_x \in \mathbb{Z}^+$, which are uniformly distributed with inter-antenna distance T_x, and the telescope is comprised of $(2N_x + 1)N_D$ *matched* (or *identical*) analog receiving channels. Although, in practice, the employed antennas are BB directional ones such as Vivaldi antennas [12], for simplicity, we assume the elemental antennas have *isotropic* radiation patterns over the desired bandwidth. Furthermore, DLAs are assumed to be configured according to the minimum-redundancy (general) array configuration [107] so that the highest possible number of baselines are obtained for a given N_D.

In the following analysis, we consider only the processing of a BB cosmic SOI emanating from a *point source*. The location of the point source is considered as the *phase center*. In fact, the synthesized BD of the point source can be considered as the 1D *point spread function* of the radio telescope. As in the previous chapters, the cosmic SOI is assumed to be *mono polarized*, and, hence, it is treated as a *scalar* quantity. Furthermore, we assume that the cosmic SOI is band limited and the Nyquist condition is satisfied by the spatial sampling with the elemental antennas.

We begin the analysis by writing the relationship between the incoming 4D CD ST PW $pw(x, y, z, \mathrm{c}t)$ and the 2D MD spatially sampled PW $pw^p_{ANT}(n_x, \mathrm{c}t)$;

$$pw^p_{ANT}(n_x, \mathrm{c}t) = pw(n_x T_x, 0, 0, \mathrm{c}t)wn(n_x), \tag{4.1}$$

where $wn(n_x)$ is the 1D window function that incorporates the finite length of the DLAs. In this case, $wn(n_x)$ is the 1D rectangular window of length $2N_x + 1$. In the 2D mixed frequency space, the spectrum of $pw^p_{ANT}(n_x, \mathrm{c}t)$, $PW^p_{ANT}(\omega_x, \Omega_{ct})$, is given

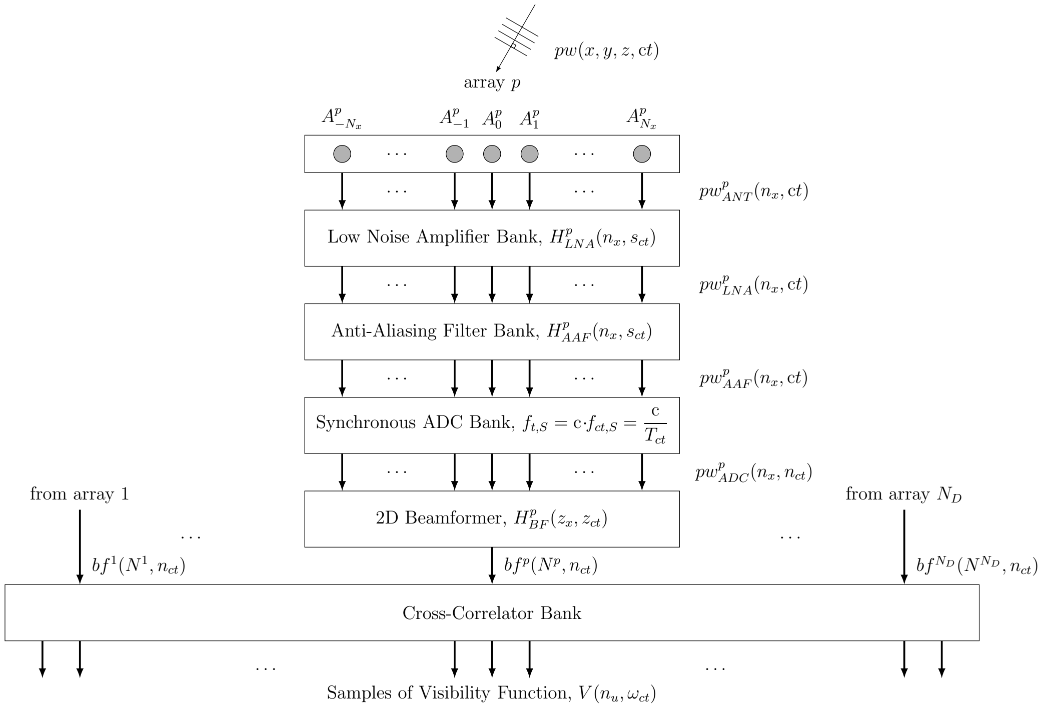

Figure 4.1: A Simplified schematic diagram of a 2D synthetic aperture system having N_D 1D DLAs that are sparsely placed in the east-west direction.

by [59](ch. 3)

$$\begin{aligned} PW^p_{ANT}(\omega_x, \Omega_{ct}) &= W(\Omega_{ct})[\delta(\omega_x - T_x \sin(\theta)\cos(\phi)\Omega_{ct}) *_x WN(\omega_x)] \\ &= W(\Omega_{ct})WN(\omega_x - T_x \sin(\theta)\cos(\phi)\Omega_{ct}), \\ &\qquad \text{for } (\omega_x, \Omega_{ct}) \in [-\pi, \pi] \times \mathbb{R}, \end{aligned} \tag{4.2}$$

where $W(\Omega_{ct})$ is the 1D CDFT of the 1D temporal function $w(\mathrm{c}t)$ that describes the amplitude of the wavefronts in the DOA, (θ, ϕ) specifies the DOA of $pw(x, y, z, \mathrm{c}t)$, $WN(\omega_x)$ is the 1D CDFT of $wn(n_x)$], and $*_x$ denotes the 1D convolution with respect to the spatial dimension. Next, the output of the LNA in the n_xth receiving channel in the pth DLA is given by the 1D temporal convolution

$$pw^p_{LNA}(n_x, \mathrm{c}t) = h^p_{LNA}(n_x, \mathrm{c}t) *_{ct} pw^p_{ANT}(n_x, \mathrm{c}t), \tag{4.3}$$

where $h^p_{LNA}(n_x, ct)$ is the impulse response of the LNA, and $*_{ct}$ denotes the 1D convolution with respect to the temporal dimension. Then, each LNA-amplified analog signal is lowpass filtered with an AAF having an appropriate frequency response prior to *synchronous* analog-to-digital conversion in order to alleviate significant aliasing. The lowpass-filtered signal $pw^p_{AAF}(n_x, \mathrm{c}t)$ can then be expressed as

$$\begin{aligned} pw^p_{AAF}(n_x, \mathrm{c}t) &= h^p_{AAF}(n_x, \mathrm{c}t) *_{ct} pw^p_{LNA}(n_x, \mathrm{c}t) \\ &= h^p_{AAF}(n_x, \mathrm{c}t) *_{ct} [h^p_{LNA}(n_x, \mathrm{c}t) *_{ct} pw^p_{ANT}(n_x, \mathrm{c}t)], \end{aligned} \tag{4.4}$$

where $h^p_{AAF}(n_x, \mathrm{c}t)$ is the impulse response of the corresponding AAF. After the synchronous analog-to-digital conversion, the resulting signal is a 2D DD signal, which can be written as

$$pw^p_{ADC}(n_x, n_{ct}) = pw^p_{AAF}(n_x, n_{ct}T_{ct}). \tag{4.5}$$

Here, for simplicity, we do not consider quantization effects caused by the finite word length of the synchronous ADCs. With the aid of Equations (4.2), (4.4) and (4.5), the spectrum of $pw^p_{ADC}(n_x, n_{ct})$, $PW^p_{ADC}(\omega_x, \omega_{ct})$, in the 2D discrete frequency space can be obtained as

$$\begin{aligned} PW^p_{ADC}(\omega_x, \omega_{ct}) = &\frac{1}{T_{ct}} H_{AAF}\left(j\frac{\omega_{ct}}{T_{ct}}\right) H_{LNA}\left(j\frac{\omega_{ct}}{T_{ct}}\right) W\left(\frac{\omega_{ct}}{T_{ct}}\right) \\ &\times WN\left(\omega_x - \frac{T_x}{T_{ct}}\sin(\theta)\cos(\phi)\,\omega_{ct}\right) \qquad \text{for } (\omega_x, \omega_{ct}) \in [-\pi, \pi]^2. \end{aligned} \tag{4.6}$$

Note that, when deriving Equation (4.6), the transfer functions of the LNAs and AAFs are considered to be independent of both p and n_x since all the LNAs and AAFs are ideally *matched*.

The main purpose of a beamformer is to extract the samples of the 1D temporal function $w(\mathrm{c}t)$ associated with the cosmic SOI with minimum distortion. In the receiver architecture illustrated in Figure 4.1, we employ a 2D ST beamformer, which is capable of processing BB signals. The output of the 2D beamformer $bf^p(n_x, n_{ct})$ can be expressed as

$$bf^p(n_x, n_{ct}) = h_{BF}(n_x, n_{ct}) ** pw^p_{ADC}(n_x, n_{ct}), \tag{4.7}$$

where $h_{BF}(n_x, n_{ct})$ is the impulse response of the beamformer, and $**$ denotes the 2D convolution. Here also, the transfer functions of all the beamformers are considered to be *matched*, hence, independent of p. In the 2D discrete frequency space, the equivalent equation of Equation (4.7) can be written as

$$BF^p(\omega_x, \omega_{ct}) = H_{BF}(\mathrm{e}^{j\omega_x}, \mathrm{e}^{j\omega_{ct}})PW^p_{ADC}(\omega_x, \omega_{ct}), \qquad \text{for } (\omega_x, \omega_{ct}) \in [-\pi, \pi]^2. \quad (4.8)$$

Although the output signal of a 2D beamformer is, in general, a 2D signal, only one 1D temporal sequence corresponding to a particular n_x (e.g., $n_x = N^p$ for the DLA p) is obtained as the beamformed signal. Let us assume $bf^p(n_x, n_{ct})$ is in the spatial steady state for N_{ss} spatial indices out of $2N_x+1$ spatial indices for which $bf^p(n_x, n_{ct})$ is calculated, and $\mathcal{N}$ is the set that contains those N_{ss} spatial indices. To facilitate the extraction of the samples of $w(ct)$ with minimum distortion through beamforming, N^p should be one out of N_{ss} spatial indices that are elements of $\mathcal{N}$.

In the cross-correlator bank, N_u cross power spectra, where N_u is the number of baselines that can be obtained with N_D DLAs and the minimum-redundancy array configuration, are calculated. The cross power spectrum $S_{pq}(\omega_{ct})$, which is calculated from $bf^p(N^p, n_{ct})$ and $bf^q(N^q, n_{ct})$, can be considered as the complex visibility $V(n_u, \omega_{ct})|_{n_u=n_u^{pq}}$, where $n_u \in \{\mathbb{Z} \cap [1, N_u]\}$ and n_u^{pq} represents the index that is corresponding to the baseline determined by the DLAs p and q, where $p, q \in \{\mathbb{Z} \cap [1, N_D]\}$, as a function of the temporal frequency ω_{ct} [35](pp. 284). It is well known that the cross power spectrum and the cross-correlation sequence of two DD signals form a Fourier transform pair;

$$S_{pq}(\omega_{ct}) = \mathcal{F}^1_{\tau_{ct}}\Big[R_{pq}(\tau_x, \tau_{ct})|_{\tau_x=0}\Big], \quad (4.9)$$

where $\mathcal{F}^n_{x_1,x_2,\ldots,x_n}[\cdot]$ denotes the nD Fourier transform with respect to $x_1, x_2, \ldots, x_n$, and the 2D cross-correlation sequence $R_{pq}(\tau_x, \tau_{ct})$ is given by

$$R_{pq}(\tau_x, \tau_{ct}) = \frac{1}{(2N_x+1)N_{ct}} \sum_{n_x=-N_x}^{N_x} \sum_{n_{ct}=0}^{N_{ct}-1} bf^p(n_x, n_{ct}) bf^{q,*}(n_x - \tau_x, n_{ct} - \tau_{ct}), \quad (4.10)$$

where $(\tau_x, \tau_{ct}) \in \{\mathbb{Z}^2 \cap \{[-2N_x, 2N_x] \times [-(N_{ct}-1), N_{ct}-1]\}\}$, N_{ct} is the number of temporal samples and $bf^{q,*}(\cdot,\cdot)$ denotes the conjugate of $bf^q(\cdot,\cdot)$. In Equation (4.9), $R_{pq}(\tau_x, \tau_{ct})|_{\tau_x=0}$ can be considered as a *slice* of $R_{pq}(\tau_x, \tau_{ct})$. Consequently, $S_{pq}(\omega_{ct})$ can be expressed, by using the projection-slice theorem [35](pp. 65–66), as

$$S_{pq}(\omega_{ct}) = \mathrm{K}\int_{-\pi}^{\pi} BF^{p}(\omega_x,\omega_{ct})BF^{q,*}(\omega_x,\omega_{ct})\,\mathrm{d}\omega_x, \qquad \text{for } \omega_{ct}\in[-\pi,\pi], \tag{4.11}$$

where $\mathrm{K} = 1/[2\pi(2N_x+1)N_{ct}]$ and

$$BF^{q,*}(\omega_x,\omega_{ct}) = H^{*}_{BF}(\mathrm{e}^{j\omega_x},\mathrm{e}^{j\omega_{ct}})PW^{q,*}_{ADC}(\omega_x,\omega_{ct}), \quad \text{for } (\omega_x,\omega_{ct})\in[-\pi,\pi]^2, \tag{4.12}$$

where

$$\begin{aligned} PW^{q,*}_{ADC}(\omega_x,\omega_{ct}) = {} & \frac{1}{T_{ct}}H^{*}_{AAF}\left(j\frac{\omega_{ct}}{T_{ct}}\right)H^{*}_{LNA}\left(j\frac{\omega_{ct}}{T_{ct}}\right)W^{*}\left(\frac{\omega_{ct}}{T_{ct}}\right) \\ & \times WN^{*}\left(\omega_x - \frac{T_x}{T_{ct}}\sin(\theta)\cos(\phi)\,\omega_{ct}\right) \quad \text{for } (\omega_x,\omega_{ct})\in[-\pi,\pi]^2. \end{aligned} \tag{4.13}$$

Note that, in the derivation of Equation (4.11)*, it is assumed that* $N^p = N^q$*, and, therefore, the slice of* $R_{pq}(\tau_x,\tau_{ct})$ *at* $\tau_x = 0$ *is used to obtain* $S_{pq}(\omega_{ct})$*. Furthermore, it is assumed that the geometric delay* t_g^{pq} *corresponding to the distance between the two arrays (i.e., the distance between the two origins of the corresponding coordinate systems) is compensated by an equivalent adjustable electronic delay. If the two beamformed signals are obtained with* $N^p \neq N^q$*, and if* t_g^{pq} *is not compensated, a term,* $\mathrm{e}^{j[\omega_x(N^p-N^q)+\omega_{ct}t_g^{pq}]}$*, should be included inside the integral of Equation* (4.11). Although S_{pq} is a function of the *continuous* variable ω_{ct}, in *digital* correlators employed in radio telescopes, it is calculated at *discrete* values of ω_{ct} through 1D FFT techniques [35](ch. 8.7). Let $\mathcal{B}$ is the set that contains the temporal discrete frequencies at which S_{pq} is calculated. Then, at a temporal discrete frequency $\omega_{ct}^i \in \mathcal{B}$, where $i \in \{\mathbb{Z}\cap[1,N_c]\}$ and N_c is the number of frequency channels of the cross-correlators, the *sample* of the visibility function $V(n_u^{pq},\omega_{ct}^i)$ is given by

$$\begin{aligned} V(n_u^{pq},\omega_{ct}^i) &= 2S_{pq}(\omega_{ct}^i) \\ &= \frac{2\mathrm{K}}{T_{ct}^2}\int_{-\pi}^{\pi}\left|W\left(\frac{\omega_{ct}^i}{T_{ct}}\right)\right|^2\left|WN\left(\omega_x - \frac{T_x}{T_{ct}}\sin(\theta)\cos(\phi)\,\omega_{ct}^i\right)\right|^2 \\ &\qquad \times\left|H_{AAF}\left(j\frac{\omega_{ct}^i}{T_{ct}}\right)H_{LNA}\left(j\frac{\omega_{ct}^i}{T_{ct}}\right)H_{BF}(\mathrm{e}^{j\omega_x},\mathrm{e}^{j\omega_{ct}^i})\right|^2\,\mathrm{d}\omega_x. \end{aligned} \tag{4.14}$$

Note that, $S_{pq}(\omega_{ct}^i)$ is multiplied by 2 to incorporate the power associated with $S_{pq}(-\omega_{ct}^i)$. Furthermore, if N_x is assumed to be sufficiently large,

$$WN\left(\omega_x - \frac{T_x}{T_{ct}}\sin(\theta)\cos(\phi)\,\omega_{ct}^i\right) \approx \delta\left(\omega_x - \frac{T_x}{T_{ct}}\sin(\theta)\cos(\phi)\,\omega_{ct}^i\right), \tag{4.15}$$

and, in this case, finite length effect is negligible. Under this condition, Equation (4.14) is reduced as

$$V(n_u^{pq}, \omega_{ct}^i) \approx \frac{2\mathrm{K}}{T_{ct}^2}\left|W\left(\frac{\omega_{ct}^i}{T_{ct}}\right)\right|^2 \left|H_{AAF}\left(j\frac{\omega_{ct}^i}{T_{ct}}\right) H_{LNA}\left(j\frac{\omega_{ct}^i}{T_{ct}}\right) H_{BF}(\mathrm{e}^{j\omega_x^i}, \mathrm{e}^{j\omega_{ct}^i})\right|^2 \tag{4.16}$$

where $\omega_x^i = (T_x/T_{ct})\sin(\theta)\cos(\phi)\,\omega_{ct}^i$. Note that, the expression in the right hand side of Equation (4.16) is independent of p and q. Therefore, all N_u samples of the visibility function $V(n_u, \omega_{ct}^i)$ have the same value.

The visibility function $V(n_u, \omega_{ct}^i)$ is symmetrical about the origin of the n_u axis in the *hermitian* sense, i.e., $V(n_u, \omega_{ct}^i) = V^*(-n_u, \omega_{ct}^i)$, since the BD of a cosmic source is real [35](pp. 61). Consequently, $V(n_u, \omega_{ct}^i)$, for $n_u = -N_u, -N_u+1, \ldots, -1$ can be obtained from the available samples of the visibility function, $V(n_u, \omega_{ct}^i)$, $n_u \in \{\mathbb{Z} \cap [1, N_u]\}$. Furthermore, $V(0, \omega_{ct}^i)$ can be estimated through the power spectrum of any beamformed sequence. In fact, this relates to an estimation of an autocorrelation sequence rather than a cross-correlation sequence. *It is worth to note that, $V(0, \omega_{ct}^i)$ represents the average value of the BD of the cosmic source, and, consequently, an estimation of $V(0, \omega_{ct}^i)$ should be incorporated in the aperture synthesis process. In other words, synthesis of BD only from the $2N_u$ samples, $V(n_u, \omega_{ct}^i)$, $|n_u| \in \{\mathbb{Z} \cap [1, N_u]\}$, with $V(0, \omega_{ct}^i) = 0$ leads to an additional error in the BD.* In general, the definitions of 1D DFT and IDFT are associated with the set of integers $\{0, 1, \ldots, 2N_u\}$ [106](ch. 5.1) rather than $\{-N_u, -N_u+1, \ldots, N_u\}$. Because $V(n_u, \omega_{ct}^i)$ can be considered as periodic with the period $2N_u+1$, $V(n_u, \omega_{ct}^i)$, for $n_u = N_u+1, N_u+2, \ldots, 2N_u$, can be obtained from $V(n_u, \omega_{ct}^i)$, $n_u \in \{\mathbb{Z} \cap [-N_u, -1]\}$ as

$$V(n_u, \omega_{ct}^i) = V(n_u - (2N_u+1), \omega_{ct}^i), \qquad \text{for } n_u = N_u+1, N_u+2, \ldots, 2N_u. \tag{4.17}$$

Then, the BD of the cosmic source $I(n_l, \omega_{ct}^i)$ can be obtained from the 1D IDFT as

$$I(n_l, \omega_{ct}^i) = \frac{1}{2N_u + 1} \sum_{n_u=0}^{2N_u} V(n_u, \omega_{ct}^i) e^{-j2\pi n_u n_l}, \qquad \text{for } n_l = 0, 1, \ldots, 2N_u. \tag{4.18}$$

It is intuitive to prefer $I(n_l, \omega_{ct}^i)$ for $n_l = -N_u, -N_u + 1, \ldots, N_u$ to that for $n_l = 0, 1, \ldots, 2N_u$ so that the origin of the n_l axis is in the middle. Because 1D IDFT results a periodic sequence [106](ch. 5.2), $I(n_l, \omega_{ct}^i)$ for $n_l = -N_u, -N_u + 1, \ldots, -1$ can be obtained from $I(n_l, \omega_{ct}^i)$, $n_u \in \{\mathbb{Z} \cap [N_u + 1, 2N_u]\}$ as

$$I(n_l, \omega_{ct}^i) = I(n_l + (2N_u + 1), \omega_{ct}^i), \qquad \text{for } n_l = -N_u, -N_u + 1, \ldots, -1. \tag{4.19}$$

In this case, $I(n_l, \omega_{ct}^i)$ is given by

$$I(n_l, \omega_{ct}^i) = \begin{cases} \frac{2\mathrm{K}}{T_{ct}^2} \left| W\left(\frac{\omega_{ct}^i}{T_{ct}}\right) \right|^2 \left| H_{AAF}\left(j\frac{\omega_{ct}^i}{T_{ct}}\right) H_{LNA}\left(j\frac{\omega_{ct}^i}{T_{ct}}\right) H_{BF}(\mathrm{e}^{j\omega_x^i}, \mathrm{e}^{j\omega_{ct}^i}) \right|^2, \\ \qquad \text{for } n_l = 0 \\ 0, \qquad \text{for } |n_l| \in \{\mathbb{Z} \cap [1, N_u]\}. \end{cases} \tag{4.20}$$

It follows from Equation (4.20) *that* $I(0, \omega_{ct}^i)$ *may have only a discrepancy in the magnitude due to the non-ideal amplitude responses of the LNAs, AAFs and the beamformers.*

4.3 Brightness Distribution Errors Caused by Perturbations in Receiver Transfer Functions

We now consider the 1D aperture synthesis of the point source located at the phase center with a synthetic aperture system having *perturbed* receiver transfer functions. The same specifications of the telescope and assumptions specified in the first two paragraphs in the above section are used in the following analysis too, and, for brevity, we do not mention those here again. We mean, by the term *receiver transfer function*, the overall transfer function corresponding to the cascaded subsystems: the LNA bank, AAF bank, synchronous ADC bank and the 2D beamformer followed by a DLA (see Figure 4.1). The analysis is mainly divided into two parts. Firstly, we consider the BD errors caused by perturbations in the transfer functions of the LNAs and AAFs. Secondly, we examine the conditions under which the BD errors caused by the phase responses of the 2D beamformers vanish.

4.3.1 Brightness Distribution Errors Caused by Perturbations in Transfer Functions of LNAs and AAFs

Here, we first establish a relationship between the errors on the samples of the visibility function and the perturbed transfer functions of the LNAs and AAFs.

Lemma 4.1. *Let the transfer functions of the LNA and the AAF in the n_xth receiving channel in the pth DLA be, respectively, expressed as*

$$H^p_{LNA}(n_x, s_{ct}) = H_{LNA}(s_{ct}) + \widetilde{\Delta H}^p_{LNA}(n_x, s_{ct}) \tag{4.21a}$$

$$H^p_{AAF}(n_x, s_{ct}) = H_{AAF}(s_{ct}) + \widetilde{\Delta H}^p_{AAF}(n_x, s_{ct}), \tag{4.21b}$$

and the transfer functions of the LNA and the AAF in the n_xth receiving channel in the qth DLA be, respectively, expressed as

$$H^q_{LNA}(n_x, s_{ct}) = H_{LNA}(s_{ct}) + \widetilde{\Delta H}^q_{LNA}(n_x, s_{ct}) \tag{4.22a}$$

$$H^q_{AAF}(n_x, s_{ct}) = H_{AAF}(s_{ct}) + \widetilde{\Delta H}^q_{AAF}(n_x, s_{ct}), \tag{4.22b}$$

where $H_{LNA}(s_{ct})$ and $H_{AAF}(s_{ct})$ are the matched components of the perturbed transfer functions of the LNAs and AAFs, respectively, and $\widetilde{\Delta H}^p_{LNA}(n_x, s_{ct})$, $\widetilde{\Delta H}^p_{AAF}(n_x, s_{ct})$, $\widetilde{\Delta H}^q_{LNA}(n_x, s_{ct})$ and $\widetilde{\Delta H}^q_{AAF}(n_x, s_{ct})$ are the components of the perturbed transfer functions that represent the respective perturbations. Then, at a temporal discrete frequency $\omega^i_{ct} \in \mathcal{B}$, the additive error $V_e(n^{pq}_u, \omega^i_{ct})$ on the sample of the visibility function caused by the perturbations is given by

$$\begin{aligned} V_e(n^{pq}_u, \omega^i_{ct}) = 2\mathrm{K}\int_{-\pi}^{\pi} \Big[& PW^p_{ADC}(\omega_x, \omega^i_{ct}) E^{q,*}(\omega_x, \omega^i_{ct}) + PW^{q,*}_{ADC}(\omega_x, \omega^i_{ct}) E^p(\omega_x, \omega^i_{ct}) \\ & + E^p(\omega_x, \omega^i_{ct}) E^{q,*}(\omega_x, \omega^i_{ct}) \Big] \Big| H_{BF}(\mathrm{e}^{j\omega_x}, \mathrm{e}^{j\omega^i_{ct}}) \Big|^2 \, \mathrm{d}\omega_x, \end{aligned} \tag{4.23}$$

where $\mathrm{K} = 1/[2\pi(2N_x+1)N_{ct}]$, $H_{BF}(z_x, z_{ct})$ is the matched transfer function of the 2D beamformers, $PW^p_{ADC}(\omega_x, \omega_{ct})$ and $PW^{q,*}_{ADC}(\omega_x, \omega_{ct})$ are, respectively, given in Equa-

tions (4.6) *and* (4.13),

$$
\begin{aligned}
E^{p}(\omega_x, \omega_{ct}) = \frac{1}{T_{ct}} W\left(\frac{\omega_{ct}}{T_{ct}}\right) WN\left(\omega_x - \frac{T_x}{T_{ct}} \sin(\theta)\cos(\phi)\,\omega_{ct}\right) *_{\omega_x} \Bigg[H_{AAF}\left(j\frac{\omega_{ct}}{T_{ct}}\right) \\
\times \Delta H^{p}_{LNA}\left(\omega_x, j\frac{\omega_{ct}}{T_{ct}}\right) + H_{LNA}\left(j\frac{\omega_{ct}}{T_{ct}}\right) \Delta H^{p}_{AAF}\left(\omega_x, j\frac{\omega_{ct}}{T_{ct}}\right) \\
+ \Delta H^{p}_{AAF}\left(\omega_x, j\frac{\omega_{ct}}{T_{ct}}\right) *_{\omega_x} \Delta H^{p}_{LNA}\left(\omega_x, j\frac{\omega_{ct}}{T_{ct}}\right) \Bigg],
\end{aligned}
$$

$$\textit{for } (\omega_x, \omega_{ct}) \in [-\pi, \pi]^2 \tag{4.24}$$

and

$$
\begin{aligned}
E^{q,*}(\omega_x, \omega_{ct}) = \frac{1}{T_{ct}} W^{*}\left(\frac{\omega_{ct}}{T_{ct}}\right) WN^{*}\left(\omega_x - \frac{T_x}{T_{ct}} \sin(\theta)\cos(\phi)\,\omega_{ct}\right) *_{\omega_x} \Bigg[H^{*}_{AAF}\left(j\frac{\omega_{ct}}{T_{ct}}\right) \\
\times \Delta H^{q,*}_{LNA}\left(\omega_x, j\frac{\omega_{ct}}{T_{ct}}\right) + H^{*}_{LNA}\left(j\frac{\omega_{ct}}{T_{ct}}\right) \Delta H^{q,*}_{AAF}\left(\omega_x, j\frac{\omega_{ct}}{T_{ct}}\right) \\
+ \Delta H^{q,*}_{AAF}\left(\omega_x, j\frac{\omega_{ct}}{T_{ct}}\right) *_{\omega_x} \Delta H^{q,*}_{LNA}\left(\omega_x, j\frac{\omega_{ct}}{T_{ct}}\right) \Bigg],
\end{aligned}
$$

$$\textit{for } (\omega_x, \omega_{ct}) \in [-\pi, \pi]^2, \tag{4.25}$$

where

$$\Delta H^{a}_{b}(\omega_x, s_{ct}) = \mathcal{F}^{1}_{n_x}\left[\widetilde{\Delta H}^{a}_{b}(n_x, s_{ct})\right], \qquad a = p, q \quad \textit{and} \quad b = LNA, AAF \tag{4.26}$$

and $*_{\omega_x}$ *denotes the 1D convolution with respect to the discrete spatial frequency.*

Proof. Let the output signal of the AAF in the n_xth receiving channel in the pth DLA be $\widehat{pw}^{p}_{AAF}(n_x, \mathrm{ct})$. Following a similar approach used in Section 4.2, $\widehat{pw}^{p}_{AAF}(n_x, \mathrm{ct})$ can be expressed as

$$\widehat{pw}^{p}_{AAF}(n_x, \mathrm{ct}) = h^{p}_{AAF}(n_x, \mathrm{ct}) *_{ct} [h^{p}_{LNA}(n_x, \mathrm{ct}) *_{ct} pw^{p}_{ANT}(n_x, \mathrm{ct})], \tag{4.27}$$

where $h^{p}_{LNA}(n_x, \mathrm{ct})$ and $h^{p}_{AAF}(n_x, \mathrm{ct})$ are the impulse responses of the corresponding LNA and AAF. Furthermore, the 2D DD signal $\widehat{pw}^{p}_{ADC}(n_x, \mathrm{ct})$ at the output of the synchronous ADC can be written as

$$\widehat{pw}^{p}_{ADC}(n_x, n_{ct}) = \widehat{pw}^{p}_{AAF}(n_x, n_{ct}T_{ct}). \tag{4.28}$$

In the 2D discrete frequency space, the 2D DDFT of $\widehat{pw}^{p}_{ADC}(n_x, n_{ct})$ can be obtained as

$$\begin{aligned}\widehat{PW}^{p}_{ADC}(\omega_x, \omega_{ct}) &= \mathcal{F}^2_{n_x,n_{ct}}\left[\widehat{pw}^{p}_{ADC}(n_x, n_{ct})\right]\\ &= \frac{1}{T_{ct}}\mathcal{F}^1_{n_x}\left[H^p_{AAF}\left(n_x, j\frac{\omega_{ct}}{T_{ct}}\right) H^p_{LNA}\left(n_x, j\frac{\omega_{ct}}{T_{ct}}\right) PW^p_{ANT}\left(n_x, \frac{\omega_{ct}}{T_{ct}}\right)\right],\\ &\qquad \text{for } (n_x, \omega_{ct}) \in \{\{\mathbb{Z} \cap [-N_x, N_x]\} \times [-\pi, \pi]\}.\end{aligned} \tag{4.29}$$

By writing $H^p_{LNA}(n_x, s_{ct})$ and $H^p_{AAF}(n_x, s_{ct})$ as additions of the respective matched and perturbed components (see Equations (4.21a) and (4.21b)), Equation (4.29) is rewritten as

$$\begin{aligned}\widehat{PW}^{p}_{ADC}(\omega_x, \omega_{ct}) &= \frac{1}{T_{ct}}\mathcal{F}^1_{n_x}\left[\left\{H_{AAF}\left(j\frac{\omega_{ct}}{T_{ct}}\right) + \widetilde{\Delta H}^{p}_{AAF}\left(n_x, j\frac{\omega_{ct}}{T_{ct}}\right)\right\}\left\{H_{LNA}\left(j\frac{\omega_{ct}}{T_{ct}}\right)\right.\right.\\ &\qquad \left.\left. + \widetilde{\Delta H}^{p}_{LNA}\left(n_x, j\frac{\omega_{ct}}{T_{ct}}\right)\right\} PW^p_{ANT}\left(n_x, \frac{\omega_{ct}}{T_{ct}}\right)\right]\\ &= PW^p_{ADC}(\omega_x, \omega_{ct}) + E^p(\omega_x, \omega_{ct}),\\ &\qquad \text{for } (\omega_x, \omega_{ct}) \in [-\pi, \pi]^2,\end{aligned} \tag{4.30}$$

where $PW^p_{ADC}(\omega_x, \omega_{ct})$ is resulted from the matched components of the transfer functions and is given in Equation (4.6), and the error $E^p(\omega_x, \omega_{ct})$ being resulted from perturbations is given by

$$\begin{aligned}E^p(\omega_x, \omega_{ct}) = &\frac{1}{T_{ct}}W\left(\frac{\omega_{ct}}{T_{ct}}\right) WN\left(\omega_x - \frac{T_x}{T_{ct}}\sin(\theta)\cos(\phi)\,\omega_{ct}\right) *_{\omega_x} \left[H_{AAF}\left(j\frac{\omega_{ct}}{T_{ct}}\right)\right.\\ &\times \Delta H^p_{LNA}\left(\omega_x, j\frac{\omega_{ct}}{T_{ct}}\right) + H_{LNA}\left(j\frac{\omega_{ct}}{T_{ct}}\right)\Delta H^p_{AAF}\left(\omega_x, j\frac{\omega_{ct}}{T_{ct}}\right)\\ &\left. + \Delta H^p_{AAF}\left(\omega_x, j\frac{\omega_{ct}}{T_{ct}}\right) *_{\omega_x} \Delta H^p_{LNA}\left(\omega_x, j\frac{\omega_{ct}}{T_{ct}}\right)\right],\\ &\qquad \text{for } (\omega_x, \omega_{ct}) \in [-\pi, \pi]^2.\end{aligned} \tag{4.31}$$

Note that, Equation (4.2) is used to derive Equation (4.31). The 2D output of the

2D beamformer can be expressed in the 2D discrete frequency space as

$$\widehat{BF}^{p}(\omega_x,\omega_{ct}) = H_{BF}(\mathrm{e}^{j\omega_x},\mathrm{e}^{j\omega_{ct}})\widehat{PW}^{p}_{ADC}(\omega_x,\omega_{ct}), \qquad \text{for } (\omega_x,\omega_{ct}) \in [-\pi,\pi]^2, \tag{4.32}$$

and, assuming that two beamformed temporal sequences are obtained with $N^p = N^q$, and the geometric delay t_g^{pq} corresponding to the distance between the two arrays is compensated by an equivalent adjustable electronic delay, the cross power spectrum $S_{pq}(\omega_{ct})$ can be expressed as

$$S_{pq}(\omega_{ct}) = \mathrm{K}\int_{-\pi}^{\pi} \widehat{BF}^{p}(\omega_x,\omega_{ct})\widehat{BF}^{q,*}(\omega_x,\omega_{ct})\,\mathrm{d}\omega_x, \qquad \text{for } \omega_{ct} \in [-\pi,\pi], \tag{4.33}$$

where $\mathrm{K} = 1/[2\pi(2N_x+1)N_{ct}]$ and

$$\widehat{BF}^{q,*}(\omega_x,\omega_{ct}) = H^{*}_{BF}(\mathrm{e}^{j\omega_x},\mathrm{e}^{j\omega_{ct}})\widehat{PW}^{q,*}_{ADC}(\omega_x,\omega_{ct}), \quad \text{for } (\omega_x,\omega_{ct}) \in [-\pi,\pi]^2. \tag{4.34}$$

Similar to Equation (4.30), $\widehat{PW}^{q,*}_{ADC}(\omega_x,\omega_{ct})$ can be expressed as

$$\widehat{PW}^{q,*}_{ADC}(\omega_x,\omega_{ct}) = PW^{q,*}_{ADC}(\omega_x,\omega_{ct}) + E^{q,*}(\omega_x,\omega_{ct}), \\ \text{for } (\omega_x,\omega_{ct}) \in [-\pi,\pi]^2, \tag{4.35}$$

where $PW^{q,*}_{ADC}(\omega_x,\omega_{ct})$ is resulted from the matched components of the transfer functions and is given in Equation (4.13), and the error $E^{q,*}(\omega_x,\omega_{ct})$ being resulted from perturbations is given by

$$\begin{aligned} E^{q,*}(\omega_x,\omega_{ct}) = {} & \frac{1}{T_{ct}} W^{*}\left(\frac{\omega_{ct}}{T_{ct}}\right) WN^{*}\left(\omega_x - \frac{T_x}{T_{ct}}\sin(\theta)\cos(\phi)\,\omega_{ct}\right) *_{\omega_x} \left[H^{*}_{AAF}\left(j\frac{\omega_{ct}}{T_{ct}}\right) \right. \\ & \times \Delta H^{q,*}_{LNA}\left(\omega_x, j\frac{\omega_{ct}}{T_{ct}}\right) + H^{*}_{LNA}\left(j\frac{\omega_{ct}}{T_{ct}}\right) \Delta H^{q,*}_{AAF}\left(\omega_x, j\frac{\omega_{ct}}{T_{ct}}\right) \\ & \left. + \Delta H^{q,*}_{AAF}\left(\omega_x, j\frac{\omega_{ct}}{T_{ct}}\right) *_{\omega_x} \Delta H^{q,*}_{LNA}\left(\omega_x, j\frac{\omega_{ct}}{T_{ct}}\right) \right], \\ & \text{for } (\omega_x,\omega_{ct}) \in [-\pi,\pi]^2. \end{aligned} \tag{4.36}$$

By substituting Equations (4.30), (4.32), (4.34) and (4.35), Equation (4.33) is rewritten as

$$S_{pq}(\omega_{ct}) = \mathrm{K}\int_{-\pi}^{\pi} \Big[PW^{p}_{ADC}(\omega_x,\omega_{ct}) + E^{p}(\omega_x,\omega_{ct})\Big]\Big[PW^{q,*}_{ADC}(\omega_x,\omega_{ct}) + E^{q,*}(\omega_x,\omega_{ct})\Big]$$
$$\times \Big|H_{BF}(\mathrm{e}^{j\omega_x},\mathrm{e}^{j\omega_{ct}})\Big|^2 \,\mathrm{d}\omega_x, \qquad \text{for } \omega_{ct} \in [-\pi,\pi]. \tag{4.37}$$

Finally, at a temporal discrete frequency $\omega_{ct}^i \in \mathcal{B}$, the sample of the visibility function $\widehat{V}(n_u^{pq},\omega_{ct}^i)$ can be obtained as

$$\begin{aligned}\widehat{V}(n_u^{pq},\omega_{ct}^i) &= 2S_{pq}(\omega_{ct}^i)\\ &= V(n_u^{pq},\omega_{ct}^i) + V_e(n_u^{pq},\omega_{ct}^i),\end{aligned} \tag{4.38}$$

where $V(n_u^{pq},\omega_{ct}^i)$ is resulted from the matched components of the transfer functions and is given in Equation (4.14), and

$$V_e(n_u^{pq},\omega_{ct}^i) = 2\mathrm{K}\int_{-\pi}^{\pi} \Big[PW^{p}_{ADC}(\omega_x,\omega_{ct}^i)E^{q,*}(\omega_x,\omega_{ct}^i) + PW^{q,*}_{ADC}(\omega_x,\omega_{ct}^i)E^{p}(\omega_x,\omega_{ct}^i)$$
$$+ E^{p}(\omega_x,\omega_{ct}^i)E^{q,*}(\omega_x,\omega_{ct}^i)\Big]\Big|H_{BF}(\mathrm{e}^{j\omega_x},\mathrm{e}^{j\omega_{ct}^i})\Big|^2 \,\mathrm{d}\omega_x \tag{4.39}$$

is the additive error on the sample of the visibility function. □

We next obtain the BD of the point source under the perturbed transfer functions of the LNAs and AAFs $\widehat{I}(n_l,\omega_{ct}^i)$ through the 1D DDFT as

$$\widehat{I}(n_l,\omega_{ct}^i) = \frac{1}{2N_u+1}\sum_{n_u=0}^{2N_u} \widehat{V}(n_u,\omega_{ct}^i)e^{-j2\pi n_u n_l}, \qquad \text{for } n_l = 0,1,\ldots,2N_u. \tag{4.40}$$

Note that, $\widehat{V}(0,\omega_{ct}^i)$ and $\widehat{V}(n_u,\omega_{ct}^i)$, for $n_u = N_u+1, N_u+2,\ldots,2N_u$, are obtained following a similar approach used in Section 4.2. By substituting Equation (4.38), Equation (4.40) can be expressed as

$$\widehat{I}(n_l,\omega_{ct}^i) = I(n_l,\omega_{ct}^i) + I_e(n_l,\omega_{ct}^i), \qquad \text{for } n_l = 0,1,\ldots,2N_u, \tag{4.41}$$

where

$$I(n_l, \omega_{ct}^i) = \frac{1}{2N_u + 1} \sum_{n_u=0}^{2N_u} V(n_u, \omega_{ct}^i) e^{-j2\pi n_u n_l}, \qquad \text{for } n_l = 0, 1, \ldots, 2N_u \tag{4.42}$$

is the *desired component*, and

$$I_e(n_l, \omega_{ct}^i) = \frac{1}{2N_u + 1} \sum_{n_u=0}^{2N_u} V_e(n_u, \omega_{ct}^i) e^{-j2\pi n_u n_l}, \qquad \text{for } n_l = 0, 1, \ldots, 2N_u \tag{4.43}$$

is the *additive error* caused by the perturbations in the transfer functions of the LNAs and AAFs. We now present a detailed analysis of characteristics of $I_e(n_l, \omega_{ct}^i)$ and its effects on $\widehat{I}(n_l, \omega_{ct}^i)$ under three cases: *completely matched, partially matched* and *unmatched* transfer functions of the LNAs and AAFs. Note that, in the following analysis, the range of n_l is taken as $\{\mathbb{Z} \cap [-N_u, N_u]\}$.

Completely Matched Case

Obviously, when all the transfer functions of the LNAs and AAFs are *completely matched*, i.e.,

$$\widetilde{\Delta H}_{LNA}^{p}(n_x, s_{ct}) = 0 \tag{4.44a}$$

$$\widetilde{\Delta H}_{AAF}^{p}(n_x, s_{ct}) = 0, \tag{4.44b}$$

$$\forall\, n_x \in \{\mathbb{Z} \cap [-N_x, N_x]\} \quad \text{and} \quad \forall\, p \in \{\mathbb{Z} \cap [1, N_D]\},$$

it follows from Lemma 4.1 that

$$V_e(n_u, \omega_{ct}^i) = 0, \qquad \forall\, n_u \in \{\mathbb{Z} \cap [0, N_u]\}. \tag{4.45}$$

Consequently,

$$I_e(n_l, \omega_{ct}^i) = 0, \qquad \forall\, n_l \in \{\mathbb{Z} \cap [-N_u, N_u]\}, \tag{4.46}$$

and

$$\widehat{I}(n_l, \omega_{ct}^i) = I(n_l, \omega_{ct}^i), \qquad \forall\, n_l \in \{\mathbb{Z} \cap [-N_u, N_u]\}. \tag{4.47}$$

Partially Matched Case

Here, *partially matched* means that the transfer functions of the LNAs and AAFs are spatial index-wise matched for all the DLAs, i.e.,

$$\begin{aligned}
&\widetilde{\Delta H}^{p}_{LNA}(n_x, s_{ct}) = \widetilde{\Delta H}^{q}_{LNA}(n_x, s_{ct}) && \text{(4.48a)}\\
&\widetilde{\Delta H}^{p}_{AAF}(n_x, s_{ct}) = \widetilde{\Delta H}^{q}_{AAF}(n_x, s_{ct}), && \text{(4.48b)}\\
&\qquad \forall\, n_x \in \{\mathbb{Z} \cap [-N_x, N_x]\} \quad \text{and} \quad \forall\, p, q \in \{\mathbb{Z} \cap [1, N_D]\}.
\end{aligned}$$

In this case, according to Equations (4.31) and (4.36),

$$E^p(\omega_x, \omega^i_{ct}) = E^q(\omega_x, \omega^i_{ct}), \qquad \text{for } \omega_x \in [-\pi, \pi] \quad \text{and} \quad \forall\, p, q \in \{\mathbb{Z} \cap [1, N_D]\}. \tag{4.49}$$

Furthermore, it follows from Equations (4.6) and (4.13) that

$$PW^p_{ADC}(\omega_x, \omega^i_{ct}) = PW^q_{ADC}(\omega_x, \omega^i_{ct}), \quad \text{for } \omega_x \in [-\pi, \pi] \quad \text{and} \quad \forall\, p, q \in \{\mathbb{Z} \cap [1, N_D]\}. \tag{4.50}$$

Therefore, under the partially matched condition, Equation (4.39) reduces to

$$\begin{aligned}
V_e(n_u, \omega^i_{ct}) = 2\mathrm{K} \int_{-\pi}^{\pi} & \Big[2\, \Re\big[PW_{ADC}(\omega_x, \omega^i_{ct}) E^*(\omega_x, \omega^i_{ct}) \big] + \big| E(\omega_x, \omega^i_{ct}) \big|^2 \Big] \\
& \times \Big| H_{BF}(\mathrm{e}^{j\omega_x}, \mathrm{e}^{j\omega^i_{ct}}) \Big|^2 \, \mathrm{d}\omega_x, \qquad \forall\, n_u \in \{\mathbb{Z} \cap [0, N_u]\},
\end{aligned} \tag{4.51}$$

where $\Re\,[\cdot]$ denotes the *real* part of a complex number, and the superscripts p and q are omitted because Equation (4.51) is independent of the indices of the DLAs. *In this case, it is clear that* $V_e(n_u, \omega^i_{ct})$, $n_u \in \{\mathbb{Z} \cap [0, N_u]\}$, *is real and constant, and, hence,* $V_e(n_u, \omega^i_{ct})$, $n_u \in \{\mathbb{Z} \cap [-N_u, N_u]\}$ *is real, even and constant. Consequently,* $I_e(n_l, \omega^i_{ct})$, $n_l \in \{\mathbb{Z} \cap [-N_u, N_u]\}$ *is real and even. Furthermore,* $I_e(n_l, \omega^i_{ct}) = 0$, *for* $|n_l| = 1, 2, \ldots, N_u$. Therefore,

$$\widehat{I}(n_l, \omega^i_{ct}) = \begin{cases} I(n_l, \omega^i_{ct}) + I_e(n_l, \omega^i_{ct}), & \text{for } n_l = 0 \\ I(n_l, \omega^i_{ct}), & \text{for } |n_l| \in \{\mathbb{Z} \cap [1, N_u]\}, \end{cases} \tag{4.52}$$

where $I_e(0, \omega^i_{ct}) \neq 0$. *Accordingly, under the partially matched condition,* $\widehat{I}(n_l, \omega^i_{ct})$ *has only a magnitude error at* $n_l = 0$ *compared to* $I(n_l, \omega^i_{ct})$.

Unmatched Case

We now consider the more realistic case where the transfer functions of the LNAs and AAFs are *unmatched*, i.e.,

$$\widetilde{\Delta H}^{p}_{LNA}(n_x, s_{ct}) \neq \widetilde{\Delta H}^{q}_{LNA}(n_x, s_{ct}) \tag{4.53a}$$

$$\widetilde{\Delta H}^{p}_{AAF}(n_x, s_{ct}) \neq \widetilde{\Delta H}^{q}_{AAF}(n_x, s_{ct}), \tag{4.53b}$$

$$\forall\, n_x \in \{\mathbb{Z} \cap [-N_x, N_x]\} \quad \text{and} \quad \forall\, p, q \in \{\mathbb{Z} \cap [1, N_D]\}.$$

In this case, it follows from Equations (4.31) and (4.36) that

$$E^p(\omega_x, \omega^i_{ct}) \neq E^q(\omega_x, \omega^i_{ct}), \qquad \text{for } \omega_x \in [-\pi, \pi] \quad \text{and} \quad \forall\, p, q \in \{\mathbb{Z} \cap [1, N_D]\}. \tag{4.54}$$

According to Equation (4.39), $V_e(n_u, \omega^i_{ct})$, $n_u \in \{\mathbb{Z} \cap [1, N_u]\}$, *is complex-valued, and only* $V_e(0, \omega^i_{ct})$ *is real-valued. Consequently,*

$$I_e(n_l, \omega^i_{ct}) \neq 0, \qquad \text{for } n_l \in \{\mathbb{Z} \cap [-N_u, N_u]\}. \tag{4.55}$$

This has two consequences on $\widehat{I}(n_l, \omega^i_{ct})$, $n_l \in \{\mathbb{Z} \cap [-N_u, N_u]\}$*: first, nonzero* $I_e(0, \omega^i_{ct})$ *causes a magnitude error at* $n_l = 0$ *compared to* $I(0, \omega^i_{ct})$*; second, nonzero* $I_e(n_l, \omega^i_{ct})$*, for* $|n_l| = 1, 2, \ldots, N_u$*, pretend faint sources.*

4.3.2 On the 2D Beamformers Employed in a 2D Synthetic Aperture System

Here, we first examine the conditions under which the *phase responses* of the 2D beamformers do not introduce errors on the synthesized BD of the point source.

Lemma 4.2. *Let all the transfer functions of LNAs and AAFs be matched, and* $H^p_{BF}(z_x, z_{ct})$ *and* $H^q_{BF}(z_x, z_{ct})$ *be the transfer functions of the 2D beamformers employed in the pth and qth DLAs, respectively. If,*

$$H^p_{BF}(z_x, z_{ct}) = H^q_{BF}(z_x, z_{ct}), \qquad \forall\, p, q \in \{\mathbb{Z} \cap [1, N_D]\}, \tag{4.56}$$

then, at a temporal discrete frequency $\omega^i_{ct} \in \mathcal{B}$*,*

$$I_e(n_l, \omega^i_{ct}) = 0, \qquad \forall\, n_l \in \{\mathbb{Z} \cap [-N_u, N_u]\}, \tag{4.57}$$

where $I_e(n_l, \omega_{ct}^i)$ *is the additive error on the BD of the point source, which is caused by the phase responses of the 2D beamformers.*

Proof. Here, we make use of the analysis in Section 4.2 for brevity. In this case, the 2D output of the beamformer in the pth DLA can be expressed in the 2D discrete frequency space as

$$BF^p(\omega_x, \omega_{ct}) = H_{BF}^p(\mathrm{e}^{j\omega_x}, \mathrm{e}^{j\omega_{ct}}) PW_{ADC}^p(\omega_x, \omega_{ct}), \qquad \text{for } (\omega_x, \omega_{ct}) \in [-\pi, \pi]^2, \tag{4.58}$$

where $PW_{ADC}^p(\omega_x, \omega_{ct})$ is given in Equation (4.6). Similarly, the conjugate of the 2D of the beamformer in the qth DLA can be expressed in the 2D discrete frequency space as

$$BF^{q,*}(\omega_x, \omega_{ct}) = H_{BF}^{q,*}(\mathrm{e}^{j\omega_x}, \mathrm{e}^{j\omega_{ct}}) PW_{ADC}^{q,*}(\omega_x, \omega_{ct}), \quad \text{for } (\omega_x, \omega_{ct}) \in [-\pi, \pi]^2, \tag{4.59}$$

where $PW_{ADC}^{q,*}(\omega_x, \omega_{ct})$ is given in Equation (4.13). By substituting Equations (4.58) and (4.59), Equation (4.11) is rewritten as

$$\begin{aligned} S_{pq}(\omega_{ct}) &= \mathrm{K}\int_{-\pi}^{\pi} PW_{ADC}^p(\omega_x, \omega_{ct}) PW_{ADC}^{q,*}(\omega_x, \omega_{ct}) H_{BF}^p(\mathrm{e}^{j\omega_x}, \mathrm{e}^{j\omega_{ct}}) H_{BF}^{q,*}(\mathrm{e}^{j\omega_x}, \mathrm{e}^{j\omega_{ct}})\, \mathrm{d}\omega_x \\ &= \mathrm{K}\int_{-\pi}^{\pi} PW_{ADC}^p(\omega_x, \omega_{ct}) PW_{ADC}^{q,*}(\omega_x, \omega_{ct}) \left| H_{BF}^p(\mathrm{e}^{j\omega_x}, \mathrm{e}^{j\omega_{ct}}) \right| \left| H_{BF}^q(\mathrm{e}^{j\omega_x}, \mathrm{e}^{j\omega_{ct}}) \right| \\ &\qquad \times \mathrm{e}^{j\left[\Phi_{BF}^p(\omega_x, \omega_{ct}) - \Phi_{BF}^q(\omega_x, \omega_{ct})\right]}\, \mathrm{d}\omega_x, \qquad \text{for } \omega_{ct} \in [-\pi, \pi], \end{aligned} \tag{4.60}$$

where $\mathrm{K} = 1/[2\pi(2N_x + 1)N_{ct}]$ and $\Phi_{BF}^p(\omega_x, \omega_{ct})$ and $\Phi_{BF}^q(\omega_x, \omega_{ct})$ are the phase responses of the 2D beamformers employed in the pth and qth DLAs, respectively. Next, at a temporal discrete frequency $\omega_{ct}^i \in \mathcal{B}$, the sample of the visibility function $\widehat{V}(n_u^{pq}, \omega_{ct}^i)$ can be obtained as

$$\begin{aligned} \widehat{V}(n_u^{pq}, \omega_{ct}^i) &= 2S_{pq}(\omega_{ct}^i) \\ &= 2\mathrm{K}\int_{-\pi}^{\pi} PW_{ADC}^p(\omega_x, \omega_{ct}^i) PW_{ADC}^{q,*}(\omega_x, \omega_{ct}^i) \left| H_{BF}^p(\mathrm{e}^{j\omega_x}, \mathrm{e}^{j\omega_{ct}^i}) \right| \\ &\qquad \times \left| H_{BF}^q(\mathrm{e}^{j\omega_x}, \mathrm{e}^{j\omega_{ct}^i}) \right| \mathrm{e}^{j\left[\Phi_{BF}^p(\omega_x, \omega_{ct}^i) - \Phi_{BF}^q(\omega_x, \omega_{ct}^i)\right]}\, \mathrm{d}\omega_x. \end{aligned} \tag{4.61}$$

By writing

$$\widehat{V}(n_u^{pq},\omega_{ct}^i) = V(n_u^{pq},\omega_{ct}^i) + V_e(n_u^{pq},\omega_{ct}^i), \tag{4.62}$$

where $V(n_u^{pq},\omega_{ct}^i)$ is the desired component, and $V_e(n_u^{pq},\omega_{ct}^i)$ is the additive error caused by the phase responses of the 2D beamformers employed in the pth and qth DLAs, the BD of the point source $\widehat{I}(n_l,\omega_{ct}^i)$ can be obtained through the 1D DDFT as

$$\begin{aligned}\widehat{I}(n_l,\omega_{ct}^i) &= \frac{1}{2N_u+1}\sum_{n_u=0}^{2N_u}\widehat{V}(n_u,\omega_{ct}^i)e^{-j2\pi n_u n_l}\\ &= I(n_l,\omega_{ct}^i) + I_e(n_l,\omega_{ct}^i), \qquad \text{for } n_l = 0,1,\ldots,2N_u, \end{aligned} \tag{4.63}$$

where

$$I(n_l,\omega_{ct}^i) = \frac{1}{2N_u+1}\sum_{n_u=0}^{2N_u}V(n_u,\omega_{ct}^i)e^{-j2\pi n_u n_l}, \qquad \text{for } n_l = 0,1,\ldots,2N_u \tag{4.64}$$

is the desired component, and

$$I_e(n_l,\omega_{ct}^i) = \frac{1}{2N_u+1}\sum_{n_u=0}^{2N_u}V_e(n_u,\omega_{ct}^i)e^{-j2\pi n_u n_l}, \qquad \text{for } n_l = 0,1,\ldots,2N_u \tag{4.65}$$

is the additive error caused by the phase responses of the 2D beamformers. Note that, $\widehat{V}(0,\omega_{ct}^i)$ and $\widehat{V}(n_u,\omega_{ct}^i)$, for $n_u = N_u+1, N_u+2,\ldots,2N_u$, are obtained following a similar approach used in Section 4.2.

If,

$$H_{BF}^p(z_x,z_{ct}) = H_{BF}^q(z_x,z_{ct}), \qquad \forall\, p,q \in \{\mathbb{Z}\cap[1,N_D]\}, \tag{4.66}$$

then,

$$\left|H_{BF}^p(\mathrm{e}^{j\omega_x},\mathrm{e}^{j\omega_{ct}})\right| = \left|H_{BF}^q(\mathrm{e}^{j\omega_x},\mathrm{e}^{j\omega_{ct}})\right|, \qquad \forall\, p,q \in \{\mathbb{Z}\cap[1,N_D]\} \tag{4.67a}$$

$$\Phi_{BF}^p(\omega_x,\omega_{ct}) = \Phi_{BF}^q(\omega_x,\omega_{ct}), \qquad \forall\, p,q \in \{\mathbb{Z}\cap[1,N_D]\}. \tag{4.67b}$$

Under the conditions in Equations (4.67a) and (4.67b),

$$\mathrm{e}^{j\left[\Phi^{p}_{BF}(\omega_x,\omega^{i}_{ct})-\Phi^{q}_{BF}(\omega_x,\omega^{i}_{ct})\right]}=1, \qquad \forall\, p,q\in\{\mathbb{Z}\cap[1,N_D]\}, \tag{4.68}$$

and Equation (4.61) reduces to Equation (4.14). (Note that, the superscripts p and q in Equation (4.61) can be omitted because, under these conditions, Equation (4.61) is independent of the indices of the DLAs.) Therefore,

$$\widehat{V}(n_u,\omega^{i}_{ct})=V(n_u,\omega^{i}_{ct}), \qquad \forall\, n_u\in\{\mathbb{Z}\cap[0,2N_u]\}, \tag{4.69}$$

and according to Equation (4.62),

$$V_e(n_u,\omega^{i}_{ct})=0, \qquad \forall\, n_u\in\{\mathbb{Z}\cap[0,2N_u]\}. \tag{4.70}$$

In this case, Equation (4.65) reduces to

$$I_e(n_l,\omega^{i}_{ct})=0, \qquad \forall\, n_l\in\{\mathbb{Z}\cap[0,2N_u]\} \tag{4.71}$$

implying that

$$I_e(n_l,\omega^{i}_{ct})=0, \qquad \forall\, n_l\in\{\mathbb{Z}\cap[-N_u,N_u]\}. \tag{4.72}$$

($I_e(n_l,\omega^{i}_{ct})$, for $n_l=-N_u,-N_u+1,\ldots,-1$, are obtained according to Equation (4.19).) □

According to Lemma 4.2, we note that, the *sufficient* condition to vanish the errors on the BD of a point source that are due to the phase responses of the 2D beamformers is that the transfer functions of the 2D beamformers are *matched*. Furthermore, the phase responses *are not necessary* to be *linear*. *Consequently, typical matched 2D IIR beamformers having nonlinear-phase responses can be used in the synthetic aperture systems as well as typical matched 2D FIR beamformers having linear-phase responses. This seems to be an especially interesting potential application of 2D IIR beamformers because they are arithmetically- and hardware-wise less complex than FIR counterparts.*

In real synthetic aperture system receivers, 2D beamformers are implemented using finite-word-length [67](ch. 14)[106](pp. 556–598) hardware in high speed very large scale integrated (VLSI) circuits [108][109][110]. In this case, the ideal transfer functions of the beamformers are obviously perturbed. However, interestingly, those perturbations are equal since the same word-length and the same realization are typically employed for the implementations of all the beamformers. *Consequently, the perturbed transfer functions are still matched, and, in general, the condition given in Lemma 4.2 (Equation* (4.56)*) is always satisfied.*

4.4 A Numerical Study of Brightness Distribution Errors Caused by Perturbations in Receiver Transfer Functions

Here, we present a numerical study of the BD errors introduced by parameter perturbations in the receiver transfer functions. We consider an illustrative example where the BD of a point source located at the phase center is synthesized. The study is mainly focused on the BD errors caused by the typical tolerances of passive L and C elements used to implement LC AAFs and the random variations of gain from LNA to LNA.

The synthetic aperture system is assumed to consist of 11 1D DLAs each of which has 101 elemental antennas ($N_x = 50$). The elemental antennas are assumed to have *isotropic* radiation patterns over the desired bandwidth, and the DLAs are assumed to be configured according to the minimum-redundancy (general) array configuration [107] with inter array distance T_{pq}, where $p, q \in \{\mathbb{Z} \cap [1, 11]\}$, being equal to integer multiples of 150 m. Note that, 45 baselines can be formed with 11 DLAs. The temporal bandwidth of the SOI is taken as 0.5–1.5 GHz, and accordingly, the inter antenna distance T_x and temporal sampling frequency $f_{t,S}$ are chosen as 7.5 cm and 4 GHz, respectively, so that the Nyquist conditions in both dimensions are satisfied. The DOA of the SOI is taken as $(\theta, \phi) = (10.0787^\circ, 0^\circ)$. The geometric delay corresponding to each array pair is an integer multiple of 350 ($= \min[T_{pq}] f_{t,S} \sin(\theta) \cos(\phi)/\mathrm{c}$, where $\mathrm{c} = 3 \times 10^8\ \mathrm{ms}^{-1}$) samples. A 2D FIR bandpass (passband $= 0.25\pi$–0.75π rad/sample) fan filter of order 80×80, designed following [111][112], is used as the 2D BB beamformer. The axis and half-width angle of the 2D FIR fan filter are the ω_{ct} axis and 20°, respectively. The cross-correlators are assumed to have the FX architecture, i.e., Fourier transformation to the temporal frequency domain is performed before cross multiplication of data from different DLAs [35](ch. 8.7), and the number of frequency channels in the desired temporal-frequency range, 0.5 GHz $< f_t \leq$ 1.5 GHz, is chosen

Design specification	Value
Maximum passband ripple	0.3 dB
Minimum stopband attenuation	40 dB
Passband edge	1.5 GHz
Stopband edge	2 GHz

Table 4.1: Design specifications of the AAFs.

as 1024.

4.4.1 BD Errors Caused by Typical Tolerances of Passive L and C Elements of AAFs

In this subsection, the BD errors caused by the typical tolerances of passive L and C elements used to implement LC AAFs are considered. Lowpass passive LC ladder filters are employed as the AAFs in analog receiver channels. The design specifications of the AAFs are given in Table 4.1. These specifications are satisfied by a fifth-order elliptic filter, a realization of which is illustrated in Figure 4.2. The values of the inductors and capacitors are obtained by appropriately denormalizing the values available in [113](ch. 5). Note that, both source and load resistors are of 1 Ω.

The tolerances of the L and C elements are incorporated by adding *fractional errors* to the desired values shown in Figure 4.2. The deviations of the amplitude and phase responses of the AAFs of which all the L and C elements are perturbed by the same amount ϵ_{AAF} are illustrated in Figure 4.3. The deviation of the amplitude response is substantial near the passband edge and in the transition band whereas that of the phase response is substantial near the passband edge and in both transition band and stopband.

Next, errors introduced to the synthesized BD of the point source by the tolerances of the L and C elements of the AAFs are calculated for the completely matched, partially matched and unmatched cases. For both partially matched and unmatched cases, the values of fractional errors are drawn from Gaussian distributions having zero mean and standard deviation σ_{AAF}. For all three cases, all the LNAs are considered to

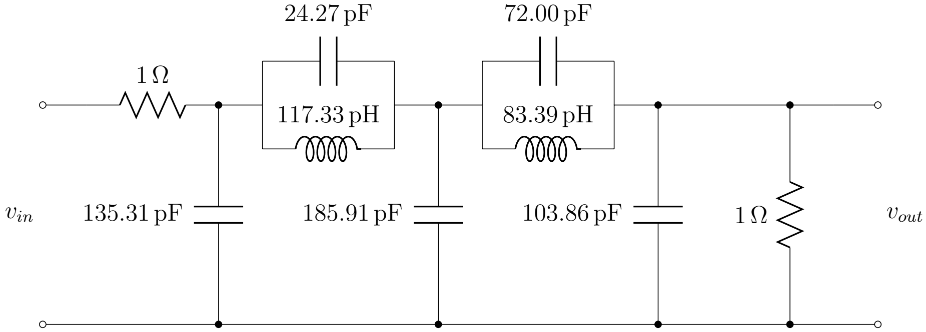

Figure 4.2: Realization of the fifth-order elliptic lowpass AAF.

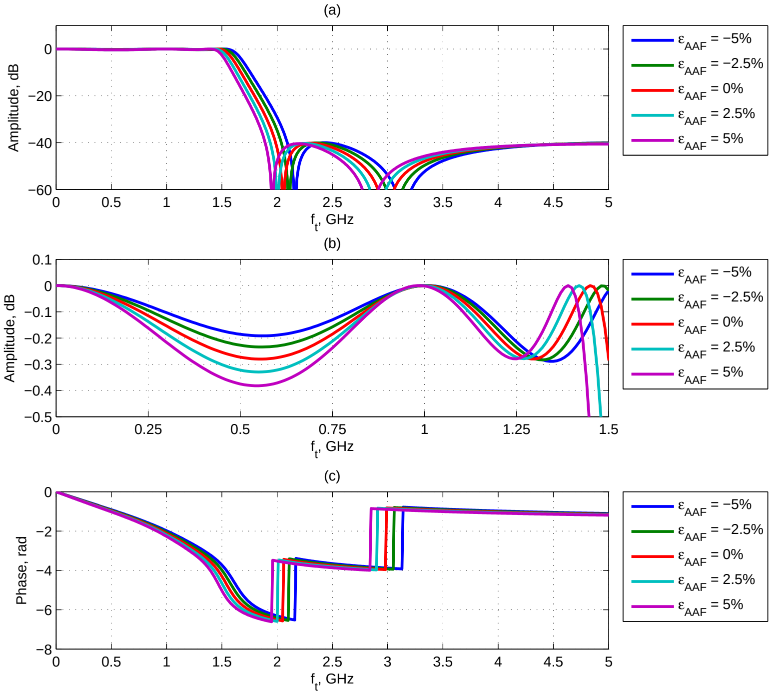

Figure 4.3: (a) Deviation of the amplitude response (b) an enlarged section of (a) corresponding to the passband and (c) deviation of the phase response of the AAFs from the desired amplitude and phase responses due to the perturbations in the L and C elements. The gain is normalized to 1 (0 dB) in the passband.

have the same (i.e., matched) gain of 20 dB. The synthesized BDs of the point source at 1.495 GHz are depicted in Figures 4.4 (a), 4.4 (b) and 4.4 (c) for the completely matched, partially matched and unmatched AAFs, respectively. For the partially matched and unmatched cases, σ_{AAF} is chosen as 2.5%. As predicted in the theoretical analysis in Section4.3.1, the BD has only a magnitude error in the partially matched

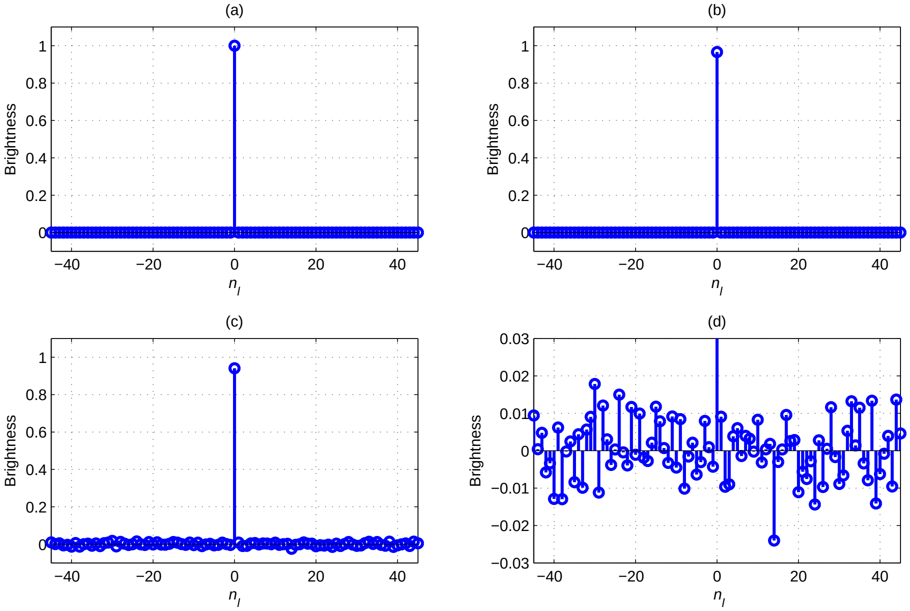

Figure 4.4: Synthesized BD of the point source at 1.495 GHz, $\sigma_{AAF} = 2.5\%$ (a) completely matched case (b) partially matched case (c) unmatched case (d) an enlarged section of (c).

case whereas in the unmatched case, the BD has both a magnitude error and artificial faint sources. Figure 4.4 (d) is an enlarged section of Figure 4.4 (c) that illustrates the artificial faint sources.

The percentage errors of the synthesized BDs for the partially matched and unmatched cases are depicted in Figures 4.5 (a) and 4.5 (b), respectively. For both cases, a significantly increase in the percentage error can be observed near the passband edge of the AAFs. This is due to the larger deviations of the amplitude and phase responses of the AAFs, due to the perturbations in the L and C elements, near the passband edge as shown in Figure 4.3. The maximum percentage errors are about 3.5% and 6% for the partially matched and unmatched cases, respectively.

4.4.2 BD Errors Caused by Random Variations of Gains of LNAs

In this subsection, errors introduced to the synthesized BD of the point source by the random variations of the gains of the LNAs are calculated for the partially matched and unmatched cases. Here, we consider only the spatial variation of the gains of

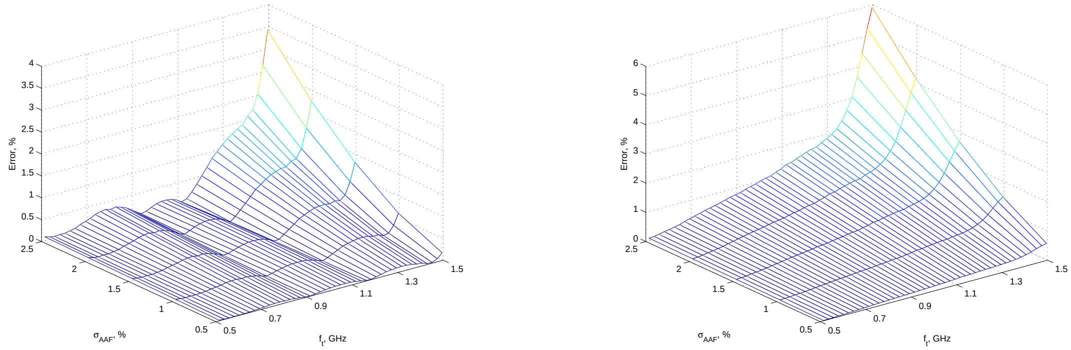

(a) (b)

Figure 4.5: Percentage error introduced to the synthesized BD of the point source by the tolerances of the L and C elements of the AAFs (a) partially matched case (b) unmatched case.

the LNAs, i.e., from LNA to LNA, and the gain of each LNA is considered to be constant over the desired temporal-frequency range. The matched (or unperturbed) gain of the LNAs is chosen as 20 dB, and the additive perturbations are drawn from Gaussian distributions having zero mean and standard deviation σ_{LNA}. Furthermore, for both cases, all the AAFs are considered to be matched.

The percentage errors of the synthesized BDs for the partially matched and unmatched cases are illustrated in Figures 4.6 (a) and 4.6 (b), respectively. In this case, the variation of the percentage error is random and entirely depends on the additive perturbations. For this particular example, the maximum percentage error is about 4% at around 830 MHz for the partially matched case whereas, for the unmatched case, the maximum percentage error is about 2% at around 1.5 GHz.

4.5 Summary

In this chapter, we analyze the BD errors caused by perturbations in the transfer functions of receivers employed in synthetic aperture systems. First, the BD errors caused by perturbations in the transfer functions of the LNAs and AAFs are considered. A detailed theoretical analysis of characteristics of the additive BD error and its effects on the synthesized BD of a point source located at the phase center is presented under three cases: completely matched, partially matched and unmatched transfer functions of the LNAs and AAFs. The synthesized BD of the point source is equivalent to the 1D point spread function of the radio telescope. In the *completely*

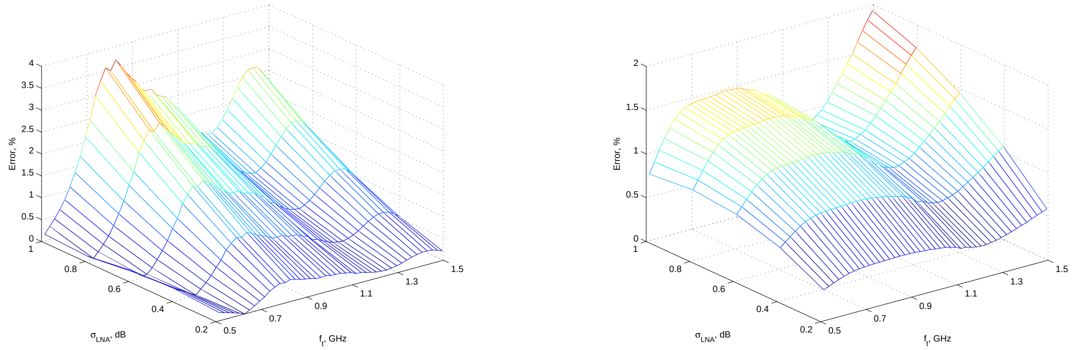

(a) (b)

Figure 4.6: Percentage error introduced to the synthesized BD of the point source by the random variations of the gains of the LNAs (a) partially matched case (b) unmatched case.

matched case, as expected, the BD error is zero. In the *partially matched case*, the BD error is real and even. Furthermore, it is nonzero only at the center. Consequently, the synthesized BD has only a magnitude error. In the more realistic *unmatched case*, the BD error is nonzero for all the points in the synthesized BD. This not only causes a magnitude error but may also lead to artificial faint sources.

Second, we investigate the conditions that should be satisfied by the transfer functions of 2D beamformers to eliminate errors caused by their phase responses. The sufficient condition to vanish the errors on the synthesized BD is that the transfer functions of the 2D beamformers are matched. Interestingly, the phase responses of the beamformers are not required to be linear. Consequently, typical IIR beamformers having nonlinear-phase responses can be employed instead of FIR counterparts because the former ones are arithmetically- and hardware-wise less complex than the latter ones for a similar performance.

Finally, the BD errors caused by the typical tolerances of passive L and C elements used to implement LC AAFs and the random variations of gain from LNA to LNA are numerically studied using an illustrative example. The deviation of the amplitude and phase responses of AAFs is substantial near the passband edge and in the transition band. The percentage error of the synthesized BDs for the partially matched and unmatched cases is substantial at frequencies near the passband edge of the AAFs. The variation of the percentage error due to the random variations of the gains of the LNAs is random and entirely depends on the additive perturbations for both partially matched and unmatched cases. Furthermore, the maximum percentage error due to the typical tolerances of passive L and C elements of AAFs is greater than that due to the random variations of the gains of the LNAs.

Chapter 5

Conclusions and Future Work

5.1 Conclusions

In this thesis, two computationally efficient 3D ST FIR cone filter bank structures: DFT and modified DFT, are proposed following [3][53] to improve the computational efficiency of the 3D ST FIR cone filter bank structure proposed in [38](ch. 5.5)[39]. Furthermore, a strategy is proposed to design 3D DFT and modified DFT frustum filter banks, having double-frustum-shaped passbands oriented along the temporal axis, from respective cone filter banks without compromising the computational efficiency. In the frustum filter banks, the double-frustum-shaped passbands are approximated by employing appropriate subsets of bands out of the total bands in the respective cone filter banks. Both DFT and modified DFT cone and frustum filter banks are almost alias free and provide near-perfect reconstruction. Furthermore, both temporal and spatial filtering operations can be carried out at a significantly lower rate in the DFT and modified DFT cone and frustum filter banks compared to the undecimated cone and frustum filter banks implying lower power consumption in the DFT and modified DFT cone and frustum filter banks.

Design examples of the DFT and modified DFT frustum filter banks indicate that they can be designed to have a small passband ripple and a good stopband attenuation. Furthermore the distortion due to aliasing is almost negligible. Furthermore, it is numerically confirmed that the DFT and modified DFT frustum filter banks provide a significant reduction of the computational complexity relative to the undecimated frustum filter banks without deteriorating the improvement in SINR in the presence of strong BB terrestrial RFI signals. Also, the computational complexity of a modified DFT frustum filter bank is approximately half of that of a DFT frustum filter bank having the same order. However, the implementation of the former requires twice the hardware required by the implementation of the latter.

A theoretical analysis of BD errors caused by parameter perturbations and mismatches among the ideally-matched transfer functions of receivers employed in synthetic aperture systems is presented. For simplicity, we consider 1D aperture synthesis with a synthetic aperture system consisting of 1D DLAs, which mimic the 1D version of more general 2D DAAs. However, the extension of the analysis from 1D to 2D aperture synthesis is straightforward. The analysis is mainly divided into two parts. First, the BD errors caused by perturbations in the transfer functions of the LNAs and AAFs are considered. The characteristics of the *additive BD error* and its effects on the synthesized BD of a point source located at the phase center are thoroughly analyzed under three cases: completely matched, partially matched and unmatched transfer functions of the LNAs and AAFs. The synthesized BD of the point source located at the phase center can be considered as the *1D point spread function* of the radio telescope. In the *completely matched case*, as expected, the BD error is zero. In the *partially matched case*, the BD error is real and even. Furthermore, it is nonzero only for the point at the center. Consequently, the synthesized BD has only a magnitude error. In the more realistic *unmatched case*, the BD error is nonzero for all the points in the synthesized BD. This not only causes a magnitude error but may lead to erroneous detection of faint sources.

Second, the conditions that should be satisfied by the transfer functions of 2D beamformers to eliminate the BD errors caused by their phase responses are examined. The sufficient condition to eliminate the BD errors is that the transfer functions of the 2D beamformers are matched, and the phase responses of the 2D beamformers are not necessary to be linear. This suggests an interesting potential application for IIR beamformers because they are arithmetically- and hardware-wise less complex than FIR beamformers.

Numerical simulations are carried out to quantify the errors introduced to the synthesized BD of a point source located at the phase center by the typical tolerances of the passive L and C elements used to implement the AAFs and the random variations of gain from LNA to LNA. The deviations of the amplitude and phase responses of AAFs are substantial near the passband edge and in the transition band. With perturbed AAFs, the percentage errors of the synthesized BDs for both partially matched and unmatched cases are substantial at frequencies near the passband edge.

The variations of the percentage errors due to the random variations of the gains of the LNAs are random and depend on additive perturbations for both partially matched and unmatched cases. Furthermore, the maximum percentage error due to the typical tolerances of the passive L and C elements of the AAFs is greater than that due to the random variations of the gains of the LNAs.

5.2 Future Work

The computational complexity of the 3D ST cone and frustum filters proposed in Chapter 3 can be further reduced by employing 2D IIR filters as the 2D spatial filters and 1D DFT and modified DFT filter banks having IIR filters. Furthermore, the 2D spatial filters can be designed by cascading 1D lowpass filters having appropriate cutoff frequencies. In this case, the ROS of the passband is more close to a square rather than a circle. Consequently, the approximation of a double-cone-shaped or a double-frustum-shaped passband is not accurate compared to the case where 2D circularly-symmetric filters are employed and may lead to a degradation of SINR. However, if 2D spatial filters are realized as cascades of 1D lowpass filters, the computational complexity of the corresponding cone or frustum filter is $\mathcal{O}(N)$ rather than $\mathcal{O}(N^2)$.

One drawback of the proposed cone and frustum filter bank structures is that the axis of the double-cone-shaped or double-frustum-shaped passband can not be oriented in directions other than the direction of the temporal axis. Consequently, the usage of beamforming applications of SOIs received by DAAs, where axis of the double-cone-shaped or double-frustum-shaped passband need to be oriented in directions other than the direction of the temporal axis, is limited. Although delays can be employed to make the DOA of an SOI as broadside, they should be either analog or digital fractional delays which increase the complexity of the implementation. Instead of the above strategy, we can investigate efficient strategies to rotate the ROS of an SOI coming from a non-broadside direction to coincide with the passband of a cone or a frustum filter having a narrow double-cone-shaped or double-frustum-shaped passband oriented along the temporal axis.

In the numerical simulations related to perturbed LNAs in Chapter 4, we perturbed only the gains. It is worthwhile to examine the BD errors caused by LNAs with both perturbed gains and phases. Furthermore, it is important to examine and evaluate the errors caused by other subsystems of synthetic aperture systems and disturbances such as those caused by the atmosphere. Furthermore, these investigations may be used to develop efficient calibration algorithms or to improve the efficiency of current calibration algorithms.

Bibliography

[1] D. E. Dudgeon and R. M. Mersereau, *Multidimensional Digital Signal Processing.* Englewood Cliffs, New Jersey: Prentice-Hall, 1984.

[2] J. W. Woods, *Multidimensional Signal, Image, and Video Processing and Coding.* Academic Press, 2006.

[3] B. Kuenzle and L. T. Bruton, "3-D IIR filtering using decimated DFT-polyphase filter bank structures," *IEEE Transactions on Circuits and Systems I: Regular Papers*, vol. 53, pp. 394–408, Feb. 2006.

[4] L. T. Bruton, "Three-dimensional cone filter banks," *IEEE Transactions on Circuits and Systems I: Fundamental Theory and Applications*, vol. 50, pp. 208–216, Feb. 2003.

[5] L. T. Bruton and N. R. Bartley, "The design of highly selective adaptive three-dimensional recursive cone filters," *IEEE Transactions on Circuits and Systems*, vol. CAS-34, pp. 775–781, July 1987.

[6] P. E. Dewdney, P. J. Hall, R. T. Schilizzi, and T. J. L. W. Lazio, "The Square Kilometre Array," *Proceedings of the IEEE*, vol. 97, pp. 1482–1496, Aug. 2009.

[7] R. T. Schilizzi, P. E. F. Dewdney, and T. J. W. Lazio, "The Square Kilometre Array," in *Proceedings of SPIE*, vol. 7012, pp. 70121l–1–70121l–13, July 2008.

[8] P. J. Hall, R. T. Schilizzi, P. E. F. Dewdney, and T. J. W. Lazio, "The Square Kilometre Array (SKA) radio telescope: Progress and technical directions," *Radio Science Bulletin*, pp. 4–19, Sep. 2008.

[9] P. J. Hall, "The Square Kilometre Array: An international engineering perspective," in *The Square Kilometre Array: An Engineering Perspective* (P. J. Hall, ed.), pp. 5–16, Springer, 2005.

[10] C. L. Carilli and S. Rawlings (eds.), "Science with the Square Kilometre Array," *New Astronomy Reviews*, vol. 48, pp. 979–1606, Dec. 2004.

[11] R. T. Schilizzi, P. Alexander, J. M. Cordes, P. E. Dewdney, R. D. Ekers, A. J. Faulkner, B. M. Gaensler, P. J. Hall, J. L. Jonas, and K. I. Kellermann, "Preliminary specifications for the Square Kilometre Array," SKA Memo 100, [Online], `http://www.skatelescope.org/uploaded/5110_100_Memo_Schilizzi.pdf`, Dec. 2003.

[12] P. J. Gibson, "The Vivaldi aerial," in *Proceedings of 9th European Microwave Conference.*, pp. 101–105, Sep. 1979.

[13] A. B. Smolders and G. W. Kant, "THousand Element Array (THEA)," in *IEEE Antennas and Propagation Society International Symposium*, vol. 1, pp. 162–165, July 2000.

[14] J. G. Bij de Vaate, S. J. Wijnholds, and J. D. Bregman, "Two dimensional 256 element phased array system for radio astronomy," in *IEEE International Symposium on Phased Array Systems and Technology*, pp. 359–364, Oct. 2003.

[15] A. van Ardenne, P. N. Wilkinson, P. D. Patel, and J. G. Bij de Vaate, "Electronic multi-beam radio astronomy concept: EMBRACE a demonstrator for the European SKA program," in *The Square Kilometre Array: An Engineering Perspective* (P. J. Hall, ed.), pp. 65–77, Springer, 2005.

[16] G. W. Kant, P. D. Patel, S. J. Wijnholds, M. Ruiter, and E. van der Wal, "EMBRACE: A multi-beam 20,000-element radio astronomical phased array antenna demonstrator," *IEEE Transactions on Antennas and Propagation*, vol. 59, pp. 1990–2003, June 2011.

[17] B. Veidt and P. Dewdney, "A phased-array feed demonstrator for radio telescopes," in *Proceedings of XXVIIIth URSI General Assembly*, Oct. 2005.

[18] B. Veidt, T. Burgess, R. Messing, G. Hovey, and R. Smegal, "The DRAO phased array feed demonstrator: Recent results," in *13th International Symposium on Antenna Technology and Applied Electromagnetics and the Canadian Radio Science Meeting*, pp. 1–4, Feb. 2009.

[19] B. Veidt, G. J. Hovey, T. Burgess, R. J. Smegal, R. Messing, A. G. Willis, A. D. Gray, and P. E. Dewdney, "Demonstration of a dual-polarized phased-array feed," *IEEE Transactions on Antennas and Propagation*, vol. 59, pp. 2047–2057, June 2011.

[20] B. Veidt, T. Burgess, R. Messing, G. J. Hovey, and R. J. Smegal, "Development of a low-noise wide-band phased-array feed," in *Proceedings of XXXth URSI General Assembly and Scientific Symposium*, pp. 1–4, Aug. 2011.

[21] A. van Ardenne, J. D. Bregman, W. A. van Cappellen, G. W. Kant, and J. G. B. de Vaate, "Extending the field of view with phased array techniques: Results of European SKA research," *Proceedings of the IEEE*, vol. 97, pp. 1531–1542, Aug. 2009.

[22] W. A. van Cappellen and L. Bakker, "APERTIF: Phased array feeds for the Westerbork Synthesis Radio Telescope," in *IEEE International Symposium on Phased Array Systems and Technology*, pp. 640–647, Oct. 2010.

[23] S. G. Hay, J. D. O'Sullivan, J. S. Kot, C. Granet, A. Grancea, A. R. Forsyth, and D. H. Hayman, "Focal plane array development for ASKAP (Australian SKA pathfinder)," in *The Second European Conference on Antennas and Propagation*, pp. 1–5, Nov. 2007.

[24] A. Chippendale and A. Schinckel, "ASKAP: Progress towards 36 parabolic reflectors with phased array feeds," in *Proceedings of XXXth URSI General Assembly and Scientific Symposium*, pp. 1–4, Aug. 2011.

[25] W. A. van Cappellen, L. Bakker, and T. A. Oosterloo, "Experimental results of the APERTIF phased array feed," in *Proceedings of XXXth URSI General Assembly and Scientific Symposium*, pp. 1–4, Aug. 2011.

[26] C. S. Ruf, "Error analysis of image reconstruction by a synthetic aperture interferometric radiometer," *Radio Science*, vol. 26, pp. 1419–1434, Nov.–Dec. 1991.

[27] F. Torres, A. Camps, J. Bará, and I. Corbella, "Impact of receiver errors on the radiometric resolution of large two-dimensional aperture synthesis radiometers," *Radio Science*, vol. 32, pp. 629–641, Mar.–Apr. 1997.

[28] A. Camps, J. Bará, F. Torres, I. Corbella, and J. Romeu, “Impact of antenna errors on the radiometric accuracy of large aperture synthesis radiometers,” *Radio Science*, vol. 32, pp. 657–668, Mar.–Apr. 1997.

[29] A. Camps, F. Torres, I. Corbella, J. Bará, and P. de Paco, “Mutual coupling effects on antenna radiation pattern: An experimental study applied to interferometric radiometers,” *Radio Science*, vol. 33, pp. 1543–1552, Nov.–Dec. 1998.

[30] J. Bará, A. Camps, I. Corbella, and F. Torres, “Specification of channel filters for an interferometric radiometer,” *Radio Science*, vol. 36, pp. 97–106, Jan.–Feb. 2001.

[31] A. Camps, I. Corbella, F. Torres, N. Duffo, M. Vall-llosera, and M. Martin-Neira, “The impact of antenna pattern frequency dependence in aperture synthesis microwave radiometers,” *IEEE Transactions on Geoscience and Remote Sensing*, vol. 43, pp. 2218–2224, Oct. 2005.

[32] C. S. Ruf, C. T. Swift, A. B. Tanner, and D. M. Le Vine, “Interferometric synthetic aperture microwave radiometry for the remote sensing of the Earth,” *IEEE Transactions on Geoscience and Remote Sensing*, vol. 26, pp. 597–611, Sep. 1988.

[33] A. R. Thompson and L. R. D’Addario, “Frequency response of a synthesis array: Performance limitations and design tolerances,” *Radio Science*, vol. 17, pp. 357–369, Mar.–Apr. 1982.

[34] A. R. Thompson, B. G. Clark, C. M. Wade, and P. J. Napier, “The Very Large Array,” *The Astrophysical Journal Supplement Series*, vol. 44, pp. 151–167, Oct. 1980.

[35] A. R. Thompson, J. M. Moran, and G. W. Swenson, Jr., *Interferometry and Synthesis in Radio Astronomy.* Wiley-VCH, 2nd ed., 2001.

[36] T. L. Wilson, K. Rohlfs, and S. Hüttemeister, *Tools of Radio Astronomy.* Berlin: Springer, 5th ed., 2009.

[37] D. Jones, “Characterization of a phased array feed model,” Master’s thesis, Department of Electrical and Computer Engineering, Brigham Young University, Provo, UT, USA, 2008.

[38] N. Liyanage, “3D space-time digital filtering for radio astronomy,” Master’s thesis, Department of Electrical and Computer Engineering, University of Victoria, Victoria, BC, Canada, 2009.

[39] N. Liyanage, L. Bruton, and P. Agathoklis, “On the attenuation of interference and mutual coupling in antenna arrays using 3D space-time filters,” in *Proceedings of IEEE Pacific Rim Conference on Communications, Computers and Signal Processing*, pp. 146–151, Aug. 2009.

[40] T. K. Gunaratne and L. T. Bruton, “Broadband beamforming of dense aperture array (DAA) and focal plane array (FPA) signals using 3D spatio-temporal filters for applications in aperture synthesis radio astronomy,” *Multidimensional Systems and Signal Processing*, vol. 22, pp. 213–236, Mar. 2011.

[41] N. Liyanage, L. Bruton, P. Agathoklis, and C. Edussooriya, “Space-time digital filtering of radio astronomical signals using 3-D cone filters,” in *Proceedings of RFI Mitigation Workshop*, pp. 1–7, Mar. 2010.

[42] C. Edussooriya, L. Bruton, and P. Agathoklis, “Under-decimated 3D FIR space-time cone filters using DFT polyphase filter banks for attenuation of radio frequency interference,” in *Proceedings of IEEE 54th International Midwest Symposium on Circuits and Systems*, pp. 1–4, Aug. 2011.

[43] T. K. Gunaratne, L. Bruton, and P. Agathoklis, “Broadband beamforming of focal plane array (FPA) signals using real-time spatio-temporal 3D FIR frustum digital filters,” *IEEE Transactions on Antennas and Propagation*, vol. 59, pp. 2029–2040, June 2011.

[44] T. K. Gunaratne, *Beamforming of Broadband Bandpass Signals using Multidimensional FIR Filters.* PhD thesis, Department of Electrical and Computer Engineering, University of Calgary, Calgary, AB, Canada, 2011.

[45] A. Leshem, A.-J. van der Veen, and A.-J. Boonstra, “Multichannel interference mitigation techniques in radio astronomy,” *The Astrophysical Journal Supplement Series*, vol. 131, pp. 355–373, Nov. 2000.

[46] F. H. Briggs, J. F. Bell, and M. J. Kesteven, “Removing radio interference from contaminated astronomical spectra using an independent reference signal

and closure relations," *The Astronomical Journal*, vol. 120, pp. 3351–3361, Dec. 2000.

[47] S. W. Ellingson, J. D. Bunton, and J. F. Bell, "Removal of the GLONASS C/A signal from OH spectral line observations using a parametric modeling technique," *The Astrophysical Journal Supplement Series*, vol. 135, pp. 87–93, July 2001.

[48] J. Raza, A.-J. Boonstra, and A.-J. van der Veen, "Spatial filtering of RF interference in radio astronomy," *IEEE Signal Processing Letters*, vol. 9, pp. 64–67, Feb. 2002.

[49] J. Minkoff, "A new very high resolution interference rejection method with potential for radio astronomy applications," *Radio Science*, vol. 38, pp. 8–1–8–14, May 2003.

[50] S. W. Ellingson and G. A. Hampson, "Mitigation of radar interference in L-band radio astronomy," *The Astrophysical Journal Supplement Series*, vol. 147, pp. 167–176, July 2003.

[51] B. D. Jeffs, L. Li, and K. F. Warnick, "Auxiliary antenna-assisted interference mitigation for radio astronomy arrays," *IEEE Transactions on Signal Processing*, vol. 53, pp. 439–451, Feb. 2005.

[52] C. K. Hansen, K. F. Warnick, B. D. Jeffs, J. R. Fisher, and R. Bradley, "Interference mitigation using a focal plane array," *Radio Science*, vol. 40, pp. 1–13, June 2005.

[53] L. T. Bruton, "A 3D polyphase-DFT cone filter bank for broad band plane wave filtering," in *Proceedings of International Symposium on Circuits and Systems*, vol. 3, pp. III–181–III–184, May 2004.

[54] S. R. Nassif, "Modeling and forecasting of manufacturing variations," in *Proceedings of 5th International Workshop on Statistical Metrology*, pp. 2–10, June 2000.

[55] S. R. Nassif, "Modeling and analysis of manufacturing variations," in *Proceedings of IEEE Conference on Custom Integrated Circuits*, pp. 223–228, May 2001.

[56] L. T. Bruton, *RC-Active Circuits: Theory and Design.* Englewood Cliffs, New Jersey: Prentice-Hall, 1980.

[57] S. Haykin, "Introduction," in *Array Signal Processing* (S. Haykin, ed.), pp. 1–5, Englewood Cliffs, New Jersey: Prentice-Hall, 1985.

[58] J. L. Yen, "Image reconstruction in synthesis radio telescope arrays," in *Array Signal Processing* (S. Haykin, ed.), pp. 293–350, Englewood Cliffs, New Jersey: Prentice-Hall, 1985.

[59] L. T. Bruton, "Multidimensional signal processing course notes." [Online], `http://www-mddsp.enel.ucalgary.ca/People/bruton/Enel699Main.html`, 2003.

[60] L. T. Bruton and N. R. Bartley, "Three-dimensional image processing using the concept of network resonance," *IEEE Transactions on Circuits and Systems*, vol. CAS-32, pp. 664–672, July 1985.

[61] J. W. M. Baars, *The Paraboloidal Reflector Antenna in Radio Astronomy and Communication: Theory and Practice.* New York: Springer, 2007.

[62] C. R. Scott, *Modern Methods of Reflector Antenna Analysis and Design.* Norwood, Massachusetts: Artech House, 1990.

[63] C. A. Balanis, *Antenna Theory: Analysis and Design.* Hoboken, New Jersey: Wiley-Interscience, 3rd ed., 2005.

[64] D. B. Hayman, T. S. Bird, K. P. Esselle, and P. Hall, "Encircled power study of focal plane field for estimating focal plane array size," in *IEEE Antennas and Propagation Society International Symposium*, vol. 3A, pp. 371–374, July 2005.

[65] K. F. Warnick, B. D. Jeffs, J. Landon, J. Waldron, D. Jones, J. R. Fisher, and R. Norrod, "BYU/NRAO 19-element phased array feed modeling and experimental results," in *Proceedings of XXIXth URSI General Assembly*, Aug. 2008.

[66] T. K. Gunaratne, "Beamforming of temporally broadband bandpass plane waves using 2D FIR trapezoidal filters," Master's thesis, Department of Electrical and Computer Engineering, University of Calgary, Calgary, AB, Canada, 2006.

[67] A. Antoniou, *Digital Signal Processing: Signals, Systems and Filters*. New York: McGraw-Hill, 2006.

[68] J. D. Bunton, "SKA PAF beamformer," SKA Memo 136, [Online], `http://www.skatelescope.org/uploaded/44534_136_Memo_Bunton.pdf`, Aug. 2011.

[69] H. Pekau, A. Yousif, and J. W. Haslett, "A CMOS integrated linear voltage-to-pulse-delay-time converter for time based analog-to-digital converters," in *Proceedings of International Symposium on Circuits and Systems*, pp. 2373–2376, May 2006.

[70] A. R. Macpherson, K. A. Townsend, and J. W. Haslett, "A 5GS/s voltage-to-time converter in 90nm CMOS," in *Proceedings of European Microwave Integrated Circuits Conference*, pp. 254–257, Sep. 2009.

[71] K. A. Townsend, A. R. Macpherson, and J. W. Haslett, "A fine-resolution time-to-digital converter for a 5GS/s ADC," in *Proceedings of International Symposium on Circuits and Systems*, pp. 3024–3027, May 2010.

[72] A. R. Macpherson, K. A. Townsend, and J. W. Haslett, "A 2.5GS/s 3-bit time-based ADC in 90nm CMOS," in *Proceedings of International Symposium on Circuits and Systems*, pp. 9–12, May 2011.

[73] L. T. Bruton, "Selective filtering of spatio-temporal plane waves using 3D cone filter banks," in *Proceedings of IEEE Pacific Rim Conference on Communications, Computers and Signal Processing*, vol. 1, pp. 67–70, Aug. 2001.

[74] G. Runze and P. Steffen, "A contribution to the design of digital three-dimensional FIR and IIR cone filters," in *Proceedings of 3D Image Analysis and Synthesis '96*, pp. 179–182, Nov. 1996.

[75] A. C. Tan and H. Sun, "Structural passive synthesis of three-dimensional recursive cone filters," in *Proceedings of 32nd Midwest Symposium on Circuits and Systems*, pp. 1119–1122, Aug. 1989.

[76] J. K. Pitas and A. N. Venetsanopoulos, "The use of symmetrics in the design of multidimensional digital filters," *IEEE Transactions on Circuits and Systems*, vol. 33, pp. 863–873, Sep. 1986.

[77] V. Rajaravivarma, P. K. Rajan, and H. C. Reddy, "Application of symmetry results in 3-D digital filter design," in *Proceedings of Twenty-First Southeastern Symposium on System Theory*, pp. 277–281, Mar. 1989.

[78] V. Rajaravivarma, P. K. Rajan, and H. C. Reddy, "Planar symmetries in 3-D filter responses and their application in 3-D filter design," *IEEE Transactions on Circuits and Systems II: Analog and Digital Signal Processing*, vol. 39, pp. 356–368, June 1992.

[79] M. V. Zervakis and A. N. Venetsanopoulos, "Design of 3-D IIR filters via transformations of 2-D circularly symmetric rotated filters," in *Proceedings of IEEE International Conference on Acoustics, Speech, and Signal Processing*, vol. 11, pp. 545–548, Apr. 1986.

[80] M. V. Zervakis and A. N. Venetsanopoulos, "Design of three-dimensional digital filters using two-dimensional rotated filters," *IEEE Transactions on Circuits and Systems*, vol. 34, pp. 1452–1469, Dec. 1987.

[81] M. Bolle, "A closed form design method for recursive 3-D cone filters," in *Proceedings of IEEE International Conference on Acoustics, Speech, and Signal Processing*, vol. VI, pp. VI–141–VI–144, Apr. 1994.

[82] L. T. Bruton and S. Singh, "Plane wave filtering using a novel 3D cone-stop filter bank," in *Proceedings of 45th Midwest Symposium on Circuits and Systems*, vol. 3, pp. 676–679, Aug. 2002.

[83] G. Runze, "Efficient design of digital 3-D cone-shaped FIR fan filters using transformations," in *Proceedings of 10th IEEE Workshop on Image and Multidimensional Signal Processing*, pp. 263–266, July 1998.

[84] G. Mollova and W. F. G. Mecklenbräuker, "A design method for 3-D FIR cone-shaped filters based on the McClellan transformation," *IEEE Transactions on Signal Processing*, vol. 57, pp. 551–564, Feb. 2009.

[85] J.-J. Shyu, S.-C. Pei, and Y.-D. Huang, "3-D FIR cone-shaped filter design by a nest of McClellan transformations and its variable design," *IEEE Transactions on Circuits and Systems I: Regular Papers*, vol. 57, pp. 1697–1707, July 2010.

[86] T. S. Huang, "Two-dimensional windows," *IEEE Transactions on Audio and Electroacoustics*, vol. 20, pp. 88–89, Mar. 1972.

[87] T. Karp and N. J. Fliege, "Modified DFT filter banks with perfect reconstruction," *IEEE Transactions on Circuits and Systems II: Analog and Digital Signal Processing*, vol. 46, pp. 1404–1414, Nov. 1999.

[88] N. J. Fliege, "Closed form design of prototype filters for linear phase DFT polyphase filter banks," in *Proceedings of International Symposium on Circuits and Systems*, vol. 1, pp. 651–654, May 1993.

[89] A. Antoniou and W.-S. Lu, *Practical Optimization: Algorithms and Engineering Applications*. New York: Springer, 2007.

[90] Y.-P. Lin and P. P. Vaidyanathan, "Application of DFT filter banks and cosine modulated filter banks in filtering," in *Proceedings of IEEE Asia-Pacific Conference on Circuits and Systems*, pp. 254–259, Dec. 1994.

[91] P. P. Vaidyanathan, *Multirate Systems and Filter Banks*. Upper Saddle River, New Jersey: Prentice-Hall, 1993.

[92] M. G. Bellanger and J. L. Daguet, "TDM-FDM transmultiplexer: Digital polyphase and FFT," *IEEE Transactions on Communications*, vol. COM-22, pp. 1199–1204, Sep. 1974.

[93] R. E. Crochiere and L. R. Rabiner, *Multirate Digital Signal Processing*. Englewood Cliffs, New Jersey: Prentice-Hall, 1983.

[94] T. Saramaki and R. Bregovic, "Multirate systems and filter banks," in *Multirate Systems: Design and Applications* (G. Jovanovic-Dolecek, ed.), pp. 27–85, Hershey, Pennsylvania: Idea Group Publishing, 2002.

[95] N. J. Fliege, "Computational efficiency of modified DFT polyphase filter banks," in *Proceedings of Twenty-Seventh Asilomar Conference on Signals, Systems and Computers*, vol. 2, pp. 1296–1300, Nov. 1993.

[96] P. N. Heller, T. Karp, and T. Q. Nguyen, "A general formulation of modulated filter banks," *IEEE Transactions on Signal Processing*, vol. 47, pp. 986–1002, Apr. 1999.

[97] T. Karp and N. J. Fliege, "MDFT filter banks with perfect reconstruction," in *Proceedings of International Symposium on Circuits and Systems*, vol. 1, pp. 744–747, May 1995.

[98] R. D. Koilpillai and P. P. Vaidyanathan, “Cosine-modulated FIR filter banks satisfying perfect reconstruction,” *IEEE Transactions on Signal Processing*, vol. 40, pp. 770–783, Apr. 1992.

[99] Y.-P. Lin and P. P. Vaidyanathan, “Linear phase cosine modulated maximally decimated filter banks with perfect reconstruction,” *IEEE Transactions on Signal Processing*, vol. 43, pp. 2525–2539, Nov. 1995.

[100] T. Q. Nguyen and R. D. Koilpillai, “The theory and design of arbitrary length cosine-modulated filter banks and wavelets, satisfying perfect reconstruction,” *IEEE Transactions on Signal Processing*, vol. 44, pp. 473–483, Mar. 1996.

[101] T. Q. Nguyen, “A quadratic-constrained least-squares approach to the design of digital filter banks,” in *Proceedings of International Symposium on Circuits and Systems*, vol. 3, pp. 1344–1347, May 1992.

[102] T. Q. Nguyen, “Digital filter bank design quadratic-constrained formulation,” *IEEE Transactions on Signal Processing*, vol. 43, pp. 2103–2108, Sep. 1995.

[103] H. S. Malvar, “Extended lapped transforms: properties, applications, and fast algorithms,” *IEEE Transactions on Signal Processing*, vol. 40, pp. 2703–2714, Nov. 1992.

[104] H. V. Sorensen, D. L. Jones, M. T. Heideman, and C. S. Burrus, “Real-valued fast fourier transform algorithms,” *IEEE Transactions on Acoustics, Speech and Signal Processing*, vol. ASSP-35, pp. 849–863, June 1987.

[105] P. Duhamel and H. Hollmann, “‘split radix’ FFT algorithm,” *Electronics Letters*, vol. 20, pp. 14–16, Jan. 1984.

[106] J. G. Proakis and D. G. Manolakis, *Digital Signal Processing: Principles, Algorithms and Applications (Eastern Economy Edition)*. New Delhi, India: Prentice-Hall, 3rd ed., 1996.

[107] A. T. Moffet, “Minimum-redundancy linear arrays,” *IEEE Transactions on Antennas and Propagation*, vol. 16, pp. 172–175, Mar. 1968.

[108] H. T. Kung, “Why systolic architectures?,” *Computer*, vol. 15, pp. 37–46, Jan. 1982.

[109] S. Y. Kung, "VLSI array processors," *IEEE ASSP Magazine*, vol. 2, pp. 4–22, July 1985.

[110] S. Y. Kung, "VLSI array processors: Designs and applications," in *Proceedings of International Symposium on Circuits and Systems*, vol. 1, pp. 313–320, June 1988.

[111] T. K. Gunaratne and L. T. Bruton, "Beamforming of broad-band bandpass plane waves using polyphase 2-D FIR trapezoidal filters," *IEEE Transactions on Circuits and Systems I: Regular Papers*, vol. 55, pp. 838–850, Apr. 2008.

[112] L. Khademi and L. T. Bruton, "Reducing the computational complexity of narrowband 2D fan filters using shaped 2D window functions," in *Proceedings of International Symposium on Circuits and Systems*, vol. 3, pp. III–702–III–705, May 2003.

[113] A. I. Zverev, *Handbook of Filter Synthesis.* John Wiley & Sons, 1967.

[114] R. E. Blahut, *Fast Algorithms for Signal Processing.* New York: Cambridge University Press, 2010.

Appendix A

Computational Complexities of DFT, Modified DFT and Undecimated Cone and Frustum Filter Banks

Here, the computational complexities of the DFT, modified DFT and the undecimated cone and frustum filter banks are derived for both real-valued and complex-valued input signals. As in [3], by computational complexity, we mean the number of arithmetic operations required by a cone or a frustum filter bank to process a sample of a real-valued or a complex-valued input signal. The realizations of the undecimated, DFT and the modified DFT cone filter banks, for which computational complexities are derived, are shown in Figures 3.1 (a), 3.5 and 3.9, respectively. The order of the temporal bandpass filters of the undecimated cone (or frustum) filter bank and that of the temporal prototype filter of the DFT or modified DFT cone (or frustum) filter bank are denoted by N_T and N_P, respectively. Furthermore, the order of the 2D spatial filters of all three cone (or frustum) filter banks is denoted by $N_{Sx} \times N_{Sy}$. In addition, all the temporal bandpass, temporal polyphase and the 2D spatial filters are assumed to be implemented using the *direct-form* structure [67](ch. 8.2)[106](ch. 7.2).

The number of nonzero coefficients in the transfer functions of the analysis and synthesis polyphase filters of a DFT or a modified DFT cone (or frustum) filter bank depends on the length (or the order) of the prototype filter. Consequently, if we express the length (N_P+1) of the prototype filter as $(N_P+1) = aM+b$, where M is the number of bands, $a \in \mathbb{N}$ and $b \in \{\mathbb{Z} \cup [0, M)\}$, the number of nonzero coefficients in the transfer function of the kth *analysis polyphase filter* (type-1 polyphase decomposition, given in Equation (3.30a)), $N_{ana,k}$, can be obtained as

Case 1: $b = 0$

$$N_{ana,k} = a, \qquad k = 0, 1, \ldots, M-1, \tag{A.1}$$

Case 2: $1 \leq b < M$

$$N_{ana,k} = \begin{cases} a+1, & k = 0, 1, \ldots, b-1 \\ a, & k = b, b+1, \ldots, M-1. \end{cases} \tag{A.2}$$

Note that, all the coefficients of the transfer function of the prototype filter are assumed to be nonzero. Similarly, the number of nonzero coefficients in the transfer function of the kth *synthesis polyphase filter* (type-3 polyphase decomposition, given in Equation (3.30b)), $N_{syn,k}$, is obtained as

Case 1: $b = 0$

$$N_{syn,k} = a, \qquad k = 0, 1, \ldots, M-1, \tag{A.3}$$

Case 2: $b = 1$

$$N_{syn,k} = \begin{cases} a+1, & k = 0 \\ a, & k = 1, 2, \ldots, M-1, \end{cases} \tag{A.4}$$

Case 3: $2 \leq b < M$

$$N_{syn,k} = \begin{cases} a+1, & k = 0 \text{ or } k = M-b+1, M-b+2, \ldots, M-1 \\ a, & k = 1, 2, \ldots, M-b. \end{cases} \tag{A.5}$$

It is clear that, in both analysis and synthesis side, the transfer functions of b polyphase filters have $a+1$ nonzero coefficients while the transfer functions of the remaining $M-b$ polyphase filters have a nonzero coefficients.

In the following derivations, the 3D input signal is assumed to have $(2N_x+1) \times (2N_y+1) \times N_{ct}$ samples. Moreover, N_{ct} is assumed to be an integer multiple of M to simply the derivations. Under this condition, the number of samples to be processed by each subband of the DFT or modified DFT cone (or frustum) filter bank is $(2N_x+1)\times(2N_y+1)\times(2N_{ct}/M)$ whereas $(2N_x+1)\times(2N_y+1)\times N_{ct}$ samples are processed in each subband of the undecimated cone (or frustum) filter bank.

In the following estimations of real multiplications and additions, the *trivial* ones, i.e., the multiplications with ± 1 and $\pm j$ and the addition with 0, are excluded. Note that, the constant $W_M^{\frac{kN_T}{2}}|_{k=M/2} = \pm 1$ or $\pm j$. Also, we assume that a complex multiplication is carried out with 3 real multiplications and 3 real additions. Moreover, in the IDFT blocks, the multiplication by M is considered to be carried out before performing the IDFT.

A.1 Computational Complexities for a 3D Real-Valued Input Signal

Although the input signal is real-valued, the subband signals (excluding those for $k = 0, M/2$), between the IDFT and DFT blocks in the DFT and modified DFT cone (or frustum) filter bank realizations (shown in Figures 3.5 and 3.9, respectively), are complex-valued. Therefore, the input signals for the spatial filters, corresponding to those $M-2$ subbands, of a DFT cone (or frustum) filter bank are complex-valued. However, in the case of a modified DFT cone (or frustum) filter bank, the input signals for all the spatial filters are either real or purely imaginary. Since the input signals for the IDFT blocks are real-valued, an FFT algorithm optimized for real-valued signals [104] can be used to implement the IDFT blocks whereas the implementation of the DFT blocks can be done by means of a general FFT algorithm designed for complex-valued signals [114](chs. 3 and 12).

The *nontrivial* real multiplications and additions required to process a real-valued sample by the different blocks of a DFT, modified DFT and an undecimated cone or frustum filter banks are given in Tables A.1 and A.2, respectively. The terms M_F and $M_{F,C}$ denote the number of bands, out of M, and the number of bands, out of $\{1, 2, \ldots, M/2-1\} \cup \{M/2+1, M/2+2, \ldots, M-1\}$, employed in a DFT or a modified DFT frustum filter bank, respectively. Also, the value of $M_{F,R}$ is defined as

$$M_{F,R} = \begin{cases} 0, & \text{if both 0th and } \frac{M}{2}\text{th bands are not employed} \\ 1, & \text{if either 0th or } \frac{M}{2}\text{th bands is employed} \\ 2, & \text{if both 0th and } \frac{M}{2}\text{th bands are employed.} \end{cases} \tag{A.6}$$

In the case of a DFT or a modified DFT cone filter bank, M_F, $M_{F,C}$ and $M_{F,R}$ takes the values of M, $M-2$ and 2, respectively. Furthermore, $M_{\mathrm{FFT},R}$, $A_{\mathrm{FFT},R}$, $M_{\mathrm{FFT},C}$ and $A_{\mathrm{FFT},C}$, respectively, denote the number of *nontrivial* real multiplications and additions required by the employed real-valued and complex-valued FFT algorithms to perform an M-point DFT (or IDFT). Moreover, L_F denotes the number of real bands employed in a undecimated frustum filter bank.

A.2 Computational Complexities for a 3D Complex-Valued Input Signal

In the case of a complex-valued input signal, the subband signals of a DFT or a modified DFT cone (or frustum) filter bank at the inputs and outputs of the 1D and 2D subband filters are complex-valued except for the 2D spatial filters of a modified DFT cone (or frustum) filter bank where, the input and output signals are either real or purely imaginary. To process a complex-valued signal, a filter of which the transfer function coefficients are real-valued requires twice the number of arithmetic operations required to process a real-valued signal because the real and imaginary parts of the complex-valued signal have to be processed separately. In fact, this is analogous to the filtering of two real-valued signals one after the other or simultaneously by the same or two identical filters, respectively. In contrast to the case of a real-valued input signal, in this case, a complex-valued FFT algorithm [114](chs. 3 and 12) should be employed to implement both DFT and IDFT blocks.

The *nontrivial* real multiplications and additions required to process a complex-valued sample by the different blocks of a DFT, modified DFT and an undecimated cone or frustum filter banks are given in Tables A.3 and A.4, respectively. As in the case of a real-valued input signal, the terms M_F and $M_{F,C}$ denote the number of bands, out of M, and the number of bands, out of $\{1, 2, \ldots, M/2-1\} \cup \{M/2+1, M/2+2, \ldots, M-1\}$, employed in a DFT or a modified DFT frustum filter bank, respectively, and in the case of a DFT or a modified DFT cone filter bank, M_F and $M_{F,C}$ are equal to M, $M-2$, respectively. Furthermore, $M_{\mathrm{FFT},C}$ and $A_{\mathrm{FFT},C}$, respectively, denote the number of *nontrivial* real multiplications and additions required by the employed complex-valued FFT algorithm to perform an M-point DFT (or IDFT), and L_F denotes the number of real bands employed in a undecimated frustum filter bank.

Block	DFT cone/frustum filter bank	Modified DFT cone/ frustum filter bank	Undecimated cone/ frustum filter bank
Temporal polyphase filters/ bandpass filters	$\frac{4}{M}[(a+1)b+a(M-b)]$	$\frac{4}{M}[(a+1)b+a(M-b)]$	$L_F(N_T+1)$
IDFT and multiplication by M	$\frac{2}{M}M_{\text{FFT},R}+2$	$\frac{2}{M}M_{\text{FFT},R}+2$	–
Spatial Filters	$\frac{2}{M}(M_{F,R}+2M_{F,C})$ $\times(N_{Sx}+1)(N_{Sy}+1)$	$\frac{2M_F}{M}(N_{Sx}+1)(N_{Sy}+1)$	$L_F(N_{Sx}+1)(N_{Sy}+1)$
DFT	$\frac{2}{M}M_{\text{FFT},C}$	$\frac{2}{M}M_{\text{FFT},C}$	–
$W_M^{\frac{kN_T}{2}}$ terms	$\frac{12M_{F,C}}{M}$	$\frac{10M_{F,C}}{M}$	–

Table A.1: Nontrivial real multiplications required to process a real-valued sample by the different blocks of a DFT, modified DFT and an undecimated cone or frustum filter banks.

Block	DFT cone/frustum filter bank	Modified DFT cone/ frustum filter bank	Undecimated cone/ frustum filter bank
Temporal polyphase filters/ bandpass filters	$\frac{4}{M}[ab+(a-1)(M-b)]$	$\frac{4}{M}[ab+(a-1)(M-b)]$	$L_F N_T$
IDFT and multiplication by M	$\frac{2}{M}A_{\mathrm{FFT},R}$	$\frac{2}{M}A_{\mathrm{FFT},R}$	–
Spatial Filters	$\frac{2}{M}(M_{F,R} + 2M_{F,C})$ $\times[(N_{Sx}+1)(N_{Sy}+1)-1]$	$\frac{2M_F}{M}[(N_{Sx}+1)(N_{Sy}+1)-1]$	$L_F[(N_{Sx}+1)(N_{Sy}+1)-1]$
DFT	$\frac{2}{M}A_{\mathrm{FFT},C}$	$\frac{2}{M}A_{\mathrm{FFT},C}$	–
$W_M^{\frac{kN_T}{2}}$ terms	$\frac{12M_{F,C}}{M}$	$\frac{6M_{F,C}}{M}$	–
Addition after upsampling	1	1	$L_F - 1$

Table A.2: Nontrivial real additions required to process a real-valued sample by the different blocks of a DFT, modified DFT and an undecimated cone or frustum filter banks.

Block	DFT cone/frustum filter bank	Modified DFT cone/ frustum filter bank	Undecimated cone/ frustum filter bank
Temporal polyphase filters/ bandpass filters	$\frac{8}{M}[(a+1)b+a(M-b)]$	$\frac{8}{M}[(a+1)b+a(M-b)]$	$2L_F(N_T+1)$
IDFT and multiplication by M	$\frac{4}{M}M_{\text{FFT},C}+4$	$\frac{4}{M}M_{\text{FFT},C}+4$	–
Spatial Filters	$\frac{4M_F}{M}(N_{Sx}+1)(N_{Sy}+1)$	$\frac{2M_F}{M}(N_{Sx}+1)(N_{Sy}+1)$	$2L_F(N_{Sx}+1)(N_{Sy}+1)$
DFT	$\frac{4}{M}M_{\text{FFT},C}$	$\frac{4}{M}M_{\text{FFT},C}$	–
$W_M^{\frac{kN_T}{2}}$ terms	$\frac{12M_{F,C}}{M}$	$\frac{10M_{F,C}}{M}$	–

Table A.3: Nontrivial real multiplications required to process a complex-valued sample by the different blocks of a DFT, modified DFT and an undecimated cone or frustum filter banks.

Block	DFT cone/frustum filter bank	Modified DFT cone/ frustum filter bank	Undecimated cone/ frustum filter bank
Temporal polyphase filters/ bandpass filters	$\frac{8}{M}[ab+(a-1)(M-b)]$	$\frac{8}{M}[ab+(a-1)(M-b)]$	$2L_F N_T$
IDFT and multiplication by M	$\frac{4}{M}A_{\mathrm{FFT},C}$	$\frac{4}{M}A_{\mathrm{FFT},C}$	–
Spatial Filters	$\frac{4M_F}{M}[(N_{Sx}+1)(N_{Sy}+1)-1]$	$\frac{2M_F}{M}[(N_{Sx}+1)(N_{Sy}+1)-1]$	$2L_F[(N_{Sx}+1)(N_{Sy}+1)-1]$
DFT	$\frac{4}{M}A_{\mathrm{FFT},C}$	$\frac{4}{M}A_{\mathrm{FFT},C}$	–
$W_M^{\frac{kN_T}{2}}$ terms	$\frac{12M_{F,C}}{M}$	$\frac{6M_{F,C}}{M}$	–
Addition after upsampling	2	2	$2(L_F-1)$

Table A.4: Nontrivial real additions required to process a complex-valued sample by the different blocks of a DFT, modified DFT and an undecimated cone or frustum filter banks.